Università degli Studi di Cagliari

DOTTORATO DI RICERCA

INGEGNERIA STRUTTURALE

Ciclo XXV

TITOLO TESI:

FLEXURAL MODELS OF REINFORCED

CONCRETE BEAMS UNDER BLAST LOAD

Settore/i scientifico disciplinari di afferenza

ICAR 09

Presentata da: Flavio Stochino

Coordinatore Dottorato: Prof. Ing. Francesco Ragnedda

Tutor/Relatore: Prof. Ing. Sergio Tattoni

Esame finale anno accademico 2011 – 2012

RINGRAZIAMENTI

Alla mia splendida moglie

A conclusione di questo percorso desidero ringraziare tutte le persone che mi hanno aiutato a crescere scientificamente e umanamente durante questi indimenticabili tre anni.

In particolare ringrazio il Prof. Ing. Sergio Tattoni per avermi fatto da guida e da mentore con un'eleganza e una pazienza non comuni, il Dott. Ing. Giorgio Carta per il fondamentale aiuto nella stesura della prima parte della tesi, ma soprattutto per il proficuo e continuo scambio di idee e di opinioni.

Sono grato al Prof. Ing. Antonio Cazzani per essere sempre stato pronto a chiarire ogni dubbio quando ne ho avuto bisogno, al Dott. Ing. Michele Brun per l'entusiasmo, l'incoraggiamento e l'esempio avuto giorno per giorno, ai Proff. Ingg. Ruge e Biondini per le accurate revisioni della tesi.

Un ringraziamento particolare va alla Prof.ssa Ing. Barbara De Nicolo per aver magistralmente coordinato il corso di Dottorato che mi ha dato la possibilità di capire qual è il mio scopo nella vita e cosa mi piace realmente fare.

Ringrazio la Fondazione Banco di Sardegna per il supporto finanziario ricevuto.

Grazie soprattutto alla mia famiglia che mi sostiene e mi sopporta da sempre, ma anche alla famiglia di mia moglie che mi ha accolto e fatto sentire a casa.

Cagliari 28 febbraio 2013   Flavio Stochino

PUBLICATIONS

Some ideas and figures have been previously discussed in the following publications:

[1] Carta G, Stochino F, "Theoretical models to predict the flexural failure of reinforced concrete beams under blast loads", Engineering Structures, Volume 49, April 2013, Pages 306–315 (2013), dx.doi.org/10.1016/j.engstruct.2012.11.008.

[2] Acito M, Stochino F, Tattoni S, "Structural response and reliability analysis of rc beam subjected to explosive loading". International Conference: PROTECT 2011 "Protection & Strengthening of Structures under Extreme Loading" – Lugano 08/30 –09/01 2011 - Applied Mechanics and Materials Vol. 82 (2011) pp 434-439 doi:10.4028/www.scientific.net/AMM.82.434.

[3] Tattoni S, Stochino F.(2012), "Azioni esplosive sulle strutture in c.a." 19° Congresso CTE, Bologna 11/8-10 2012- Pag. 407-417, ISBN: 978-88-903647-9-2.

[4] Acito M. Stochino F. Tattoni S., "Analisi della sicurezza di travi in c.a. soggette ad azioni da esplosione". Giornate AICAP 2011 – Le prospettive di sviluppo delle opere in calcestruzzo strutturale nel terzo millennio, Padova 05/19-21 2011 – Pag. 3-11.

[5] Stochino F. Tattoni S., "Incremento prestazionale per edifici in c.a. resistenti ad esplosione e relativa valutazione economica". Giornate AICAP 2011 – Le prospettive di sviluppo delle opere in calcestruzzo strutturale nel terzo millennio, Padova 05/19-21 2011 – Pag. 375-380.

INDEX

LIST OF FIGURES

LIST OF TABLES

INTRODUCTION

Nowadays, the issue of structural safety under blast loading has become a dramatic problem. The tragic news of the terrorist attacks of recent years (9/11/2001, New York; 7/7/2005, London; 7/23/2005, Sharm El Sheik; 1/24/2011, Moscow; etc), raise important, urgent questions regarding the real safety and reliability of our buildings. Extreme loads such as impacts, explosions, etc., can occur in everyday life with unexpectedly high frequency. Actually, the problem of terrorist attacks, so important for strategic and military building design, has been linked to residential and industrial building explosion accidents.

It is intuitively true that the effects of explosions on structures can be tremendously dangerous, since they can cause severe damage to buildings and, consequently, loss of lives. Since loads due to blast overpressure can be very extreme, structural elements should be endowed with enough strength and, above all, ductility to resist such loads. The evaluation of building response under blast load is a very complex subject due to the great non-linearity of the phenomena involved. Both load and structural models are affected by several uncertainties, which increase along with increasing complexity of analysis and the number of parameters considered. In introducing this issue, it is important to define ''explosion'', as stated by Mays and Smith [6]: "An explosion is a very fast chemical reaction producing the transient air pressure waves called blast waves." In order to better understand the complexity of this phenomenon, another definition by Genova-Silvestrini [7] may be useful: "The term explosion indicates a violent reaction, typical of explosives, characterized by great development of gas and heat and consequent increase in the volume of reaction products[1] ". It is thus understandable that facing this type of problem involves different fields of physical science, chemistry and, of course, engineering. In particular, evaluating and predicting the time-history of blast-load pressure is a vast and interesting topic, but is not the real objective of this work. On the contrary, the structural collapse caused by a blast load is the main subject of this thesis. Actually, in the case of explosion loads, the failure mechanism can be distinguished as a local or global one, as stated by De Matteis et alt. [8]:

- Local failure of structural elements directly due to the effect of the wave impact on structural elements.

---

[1] Original Italian from [7]: *"Con il termine esplosione si indica una violenta reazione, tipica degli esplosivi, caratterizzata da un forte sviluppo di gas e calore e conseguente aumento di volume dei prodotti di reazione".*

- Global collapse affecting the whole structure. It often occurs following localized collapse and is closely related to structural robustness.

Obviously, global collapse is more dangerous. One of the characteristics required by modern performance-based codes is the capability to redistribute loads as a result of the collapse of a localized structural element. In design procedures, both types of collapse should be taken into consideration. In this work, the author investigates the resistance of flexural elements under blast load, focusing only on local failure.

The explosion load model must take into account many variables which are difficult to determine a priori. A typical pressure time-history is shown in Fig. 1 (a) in case of detonation (wave velocity exceeds the speed of sound) and in Fig. 1 (b) in case of deflagration (wave velocity does not exceed the speed of sound). In the former case, the blockage ratio[2] is not relevant, and the magnitude of the charge and its distance from the target become predominant. On the contrary, referring to deflagration, the blockage ratio plays a fundamental role, as does charge magnitude.

positive phase duration
(a)

positive phase positive phase duration
(b)
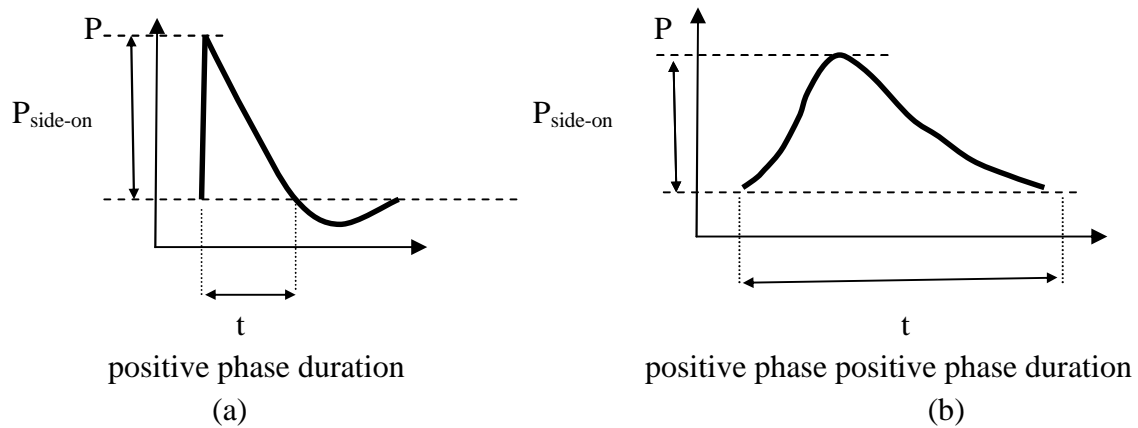
Fig. 1: Pressure time-histories for detonation (a) and deflagration (b).

In [9], the author proposes an overview of methods for assessing the effect of explosive action on buildings. He assumes to distinguish three categories:

- Empirical methods: essentially statistical correlations of experimental data.
- Semi-empirical methods: models based on simplified physical phenomenon.
- Numerical methods: numerical solutions of the fluid dynamics equations governing the phenomenon (Computational Fluid Dynamics (CFD)).

Choosing the best method depends on how much information is given for the load scenario. In fact, the more sophisticated the model, the more parameters must be known.
Empirical models are simpler and generally less accurate. There are several manuals ([10] for example) which present graphs and tables showing the results of various experimental analyses. These data can be very useful in initial assessment. They easily provide an order of magnitude of the variables involved and, within the limits of the experimental conditions in which they were obtained, are precise.

---

[2] The blockage ratio can be referred to both surface and volume. Actually, it represents the ratio between the sum of all obstacles volume/surface and the total studied volume/surface.

Semi-empirical models are developed by trying to interpret physical phenomenon assuming simplified hypothesis. There are several publications using this type of formulation (e.g.[11]. [12]). An interesting example is Hudson's method of evaluating the effect of compensation undergone by the pressure wave when it strikes a surface of finite width. In fact, the presence of edge effects produces a considerable pressure reduction on the target. Hudson in [13] proposes a series of assumptions (e.g. the pressure wave assumed to be plane) permitting a closed-form solution of the equations defining the problem. This method was recently rediscovered by Tyas et alt. [14], [15]. By means of experimental tests, the authors demonstrated that the real accuracy of this approach is greater than that obtained using the usual methods (e.g. ConWep software, etc.).

More complex models are developed by means of computational fluid-dynamic (CFD) solutions. Firstly, equations analytically representing the problem are assumed: the continuity equation, Navier Stokes' equation, the energy conservation equation. Actually, the main difficulty lies in the fact that these equations contain non-linear terms, and it is not always possible to find a solution in closed form. In most cases, it is necessary to resort to numerical discretization in space and time. The way in which the discretization (mesh) is done characterizes the calculation code and its numerical techniques. From the Lagrangian point of view, the evolutionary state of each particle is considered with a mesh which deforms and moves with the material. On the other hand, in the case of an Eulerian approach, the focus is on the state of the fluid at specific points in space at different instants in time. In this case, the mesh is fixed and is crossed by the moving material. Finally, there are codes using both systems according to varying situations (Arbitrary, Lagrangian, Eulerian, e.g.).

As regards the problem of external explosions caused by terrorist attacks, the uncertainties and difficulties can be described at different levels of detail. Firstly, it is necessary to define the quantification of the explosive threat in terms of kg of equivalent TNT[3]. The second level of uncertainty concerns the geometry scenario. It is usually defined by the distance between the position of the charge and the target structure and the relative position of the various objects on the scene (protective walls, street furniture, but also size and blockage ratio of the environment). The most common parameter generally used to describe this problem is stand-off distance d, the distance between the position of the charge and the target. In the current literature ([6], [7], [10]), these two variables (stand-off distance d and mass of TNT equivalent M) are expressed by means of a new quantity called scaled distance, as in Eq (1). The blast load time-history is often expressed as a function of time and stand-off distance.

$$z = \frac{d}{M^{1/3}}$$

(1)

The present thesis deals with the flexural failure of Reinforced Concrete beams under blast loads. The main aim is firstly to develop dynamic and energy models capable of evaluating the response of R.C. under explosive load. Then a sensitivity analysis is obtained by means of the above mentioned models in order to determine what are the key parameters in the beam response. In this way it is possible to attain simple predictive polynomial formulations and, finally, simple table for early structural assessment of beams under blast load during the design procedure.

---

[3] The equivalence factor is derived on the basis of energy considerations between TNT and other explosives.

The thesis is composed of three sections, each of which provides innovative methodologies and an introductory part presenting the literature state of the art.

Various dynamic models are developed in Section 1, taking into account the strain-rate sensitivity of both steel and concrete, as well as other nonlinearities in structural behaviour. Models with different levels of complexity are presented, from the simplest Single Degree Of Freedom (SDOF) system to Continuous Beam and Finite Element models. The characteristics, advantages and disadvantages of each approach are stated and discussed. The author considers as benchmark problem the works by Magnusson and Hallgren [16] - [20] and compares his models with the experimental results set out in [16] and [17]. The principal innovation that can be inferred from this section is the hypothesis of distributed plasticity along the beam (in the continuous model), represented by a non-linear smooth relationship between bending moment and curvature. This relationship, in addition to the Euler-Bernoulli beam equation, yields a non-linear Partial Differential Equation solved by means of the Finite Difference Method.

In Section 2, the same problem is solved in a different way: starting from the principle of energy conservation, the innovative procedure, developed by the author, can calculate the displacement field of a R.C. beam under blast load. This procedure, less accurate than the previous one, produces very good results regarding midspan displacement, especially as it requires less computation time.

In order to better understand the phenomenon, with the aim of identifying the key parameters in structural response, a sensitivity analysis is developed in Section 3. To this end, the author has performed a numerical investigation referring to the SDOF model presented in Section 1. Several numerical simulations are performed, with random variation of beam and load characteristics. Results are expressed in terms of maximum deflection and maximum velocity for each case. Then a least-squares interpolation has produced various polynomial curves and surfaces representing both a simplified tool to estimate structural response and a sensitivity analysis of the key parameters involved. One of the possible developments of this useful work is represented by simple tables (function of key parameters, see chapter 3.2.3) that provide the response of the beam under blast load for early assessment in design procedures.

SECTION 1:

DYNAMIC MODELS OF BEAMS UNDER BLAST LOAD

Chapter 1.0. Section Introduction

Determining the dynamic response of a reinforced concrete beam under blast loads is not an easy task, in part due to the complexity of modelling the structural element (considering that the behaviour of the beam under such loads is generally nonlinear and that properties of the materials are functions of the strain rate) and in part due to the difficulty of precisely defining the time variation and space distribution of the load. Actually, various simplified methods have been proposed to date. It is possible to identify three main theoretical approaches (see [21]) to the problem of a beam under blast load:

- Rigid-plastic models
- Elastic-plastic Single Degree of Freedom models
- Modal approximation and distributed models

1.0.1 Rigid-Plastic models

The first papers regarding the Rigid-Plastic model of beams under blast load date back to the fifties, but interest in the subject increased during the following years. Initially, there were solutions for specific cases without trying to develop an effective generalization (see [22]-[24]). Ten years later, Martin and Symonds [25] generalized the analysis of beams under impulsive load by means of a procedure for defining one equivalent Single Degree of Freedom Model (SDOF). This work represents an opportunity to present the "elementary rigid-plastic theory" on which it is based. Its basic assumptions are as follows:

- Ductile material has a rigid, perfectly plastic constitutive behaviour (excluding any elastic effects) under shock loading.
- Displacements must be geometrically small.
- Yield stress must be independent of strain-rate effect.

It is clear that the limits of the theory are defined on the one hand by the limitation of small

displacements, and on the other by the fact that the elastic energy that can be stored must be much less than the total energy incident in order to disregard the elastic effect. *"These two requirements are somewhat contradictory because the large disturbance needed to meet the energy requirement will tend to produce large deformations"* is stated in [25]. For this reason, any extension of the theory must be treated with great care. The importance of the theory is to provide a quick, simple estimate of the maximum deformation caused by impulsive-dynamic loads. One of the keys lies in the assumptions on the yield characteristics of the material: the yield function is determined using the plastic flow rule for a rigid, perfectly-plastic body (see Prager [26]).

If a solution is found that satisfies all the conditions (equilibrium, compatibility of deformation, in relation to yield stress/strain), the uniqueness of the solution ensures that it will also be the only valid one. The objective function is usually velocity as a function of position along the beam and time.

The response of one-dimensional rigid-plastic structures is divided into two phases: first to determine travelling plastic hinges and then to make deformations occur without changing the shape of the velocity field found.

In the paper by Martin and Symonds [25], several beams are analyzed in different boundary and loading conditions. To summarize, we may consider the example depicted in Fig. 2. This figure shows the time evolution of velocity profiles, indicating the different positions of the plastic hinges at different time steps following the hypothesized failure mechanism. The two central hinges tend to converge on the midspan, while lateral ones move to the fixed end of the beam.
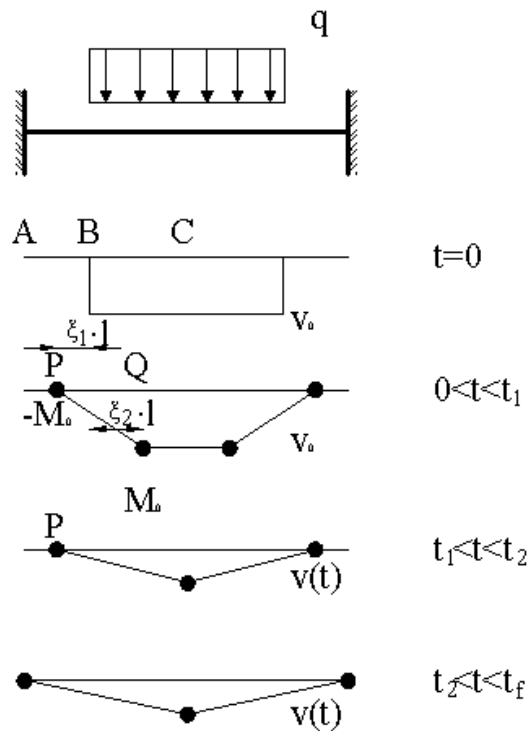
Fig. 2: Velocity profiles at different time steps for clamped beam.

Using the equations of momentum conservation and of the moment of momentum conservation, the analytical solution to the problem can be obtained. In [25], it is summarized as the position of the

plastic boundary ξ relative to point B (see Fig. 2) as a function of time:

$$\xi_1^2 = \xi_2^2 = \frac{12M_0 t}{ml^2 v_0} \tag{2}$$

In this Eq. (2) M_0 is the ultimate bending moment, m is the beam mass per unit length, t is the time, l is the span length and v_0 is the magnitude of the initial velocity.

SDOF model approximations are generally based on the assumption that the structure will assume a deformation pattern that can be described with only one parameter. In [25], approximation concerns the shape of the velocity field. The authors obtained displacements by means of velocity integration and set up a methodology for the SDOF model under impulsive load in elementary rigid-plastic theory.

The analysis by Martin and Symonds [25] was extended by Vashi [27], who took shear deformation into account as well. Several analyses were developed to also consider shear failure, not only plastic hinges due to bending. Symonds himself wrote several articles on this subject [28], [29].

In the '70s and '80s, theoretical solutions for monolithic rigid-plastic beams subjected to impulsive load had already been proposed (e.g. [30], [31]), and some experimental benchmark works began to spread, attempting to measure and verify these theoretical predictions. One of the most widely-cited in those years is Menkes and Opat's work [32]: they experimentally studied the response and failure of some fully-clamped aluminium beams subjected to velocity fields uniformly distributed along the span. It was observed that the beams respond in a ductile manner when they were subjected to speeds below a certain limit. When this value was reached, the beams entered a crisis state, and brittle failure (at constrained ends) was observed. Above this speed, travelling plastic hinges turned up closer to the end. In the case of a further increase in velocity, shear failure can occur. Norman Jones [33]-[36] developed, between the mid-seventies and mid-nineties, detailed research on rigid plastic beams under impulsive load. In these works, the rigid-plastic theory is a powerful tool to simply compute displacements and maximum speeds of beams subjected to impulsive loading. Above all, initial conditions are classified in terms of load, material, etc. to obtain a particular type of rupture. These theoretical methods are often compared with the experimental results by Menkes and Opat [32]. In particular, the influence of rotational inertia and transverse shear forces on the plastic response of rigid plastic beams was investigated in [37]-[40].

Rigid plastic models for beams have even been developed in recent works: for example, Lellep and Torn in [41] analyse the response of a rigid plastic beam under impulsive load. They refer to the square yield criterion which retains the transverse shear force as well as the bending moment. Qiu and Deshpande [41] also developed an analytical model for the response of clamped sandwich (and monolithic) beams subjected to impulsive loading over a central loading patch. Sandwich metallic structures under the same kind of loading are investigated in [42], also demonstrating, in 2009, how reliable, suitable and interesting rigid plastic models are.

1.0.2 Elastic-Plastic Single Degree of Freedom Models

The most elementary, common dynamic approach to model beams under blast load consists of schematizing the beam with a Single Degree of Freedom (SDOF) system. This approach simplifies both the theoretical formulation of the problem and calculations, but it usually requires the introduction of empirical formulas and, in addition, it does not provide full information on beam response. Actually, it only provides the fundamental response mode normally responsible for overall structural failure [21].

A pioneering work by Frankland [44] shows how World War II increased interest in the scientific world regarding impulsive loading on structures. The first models were very simple: purely undamped elastic SDOF.

Colin Morison [45] distinguishes two main SDOF approaches:

- ❖ Modal Method.
- ❖ Equivalent SDOF Method

The modal method was first presented in 1946 in the US Manual, ''Fundamentals of Protective Design (Non-Nuclear)'' EM 1110-345-405, re-issued in 1965 as TM5-855-1 [46]. This method assumes that the elastic forced response of the real element will be approximated by its first mode of free vibration. In case of elastic-pure plastic resistance function, the equation of motion can be solved in a close form, and referring to an idealised blast load, with triangular/rectangular time-history, maximum deflection can easily be calculated in order to develop a diagram like the one depicted in Fig. 3.
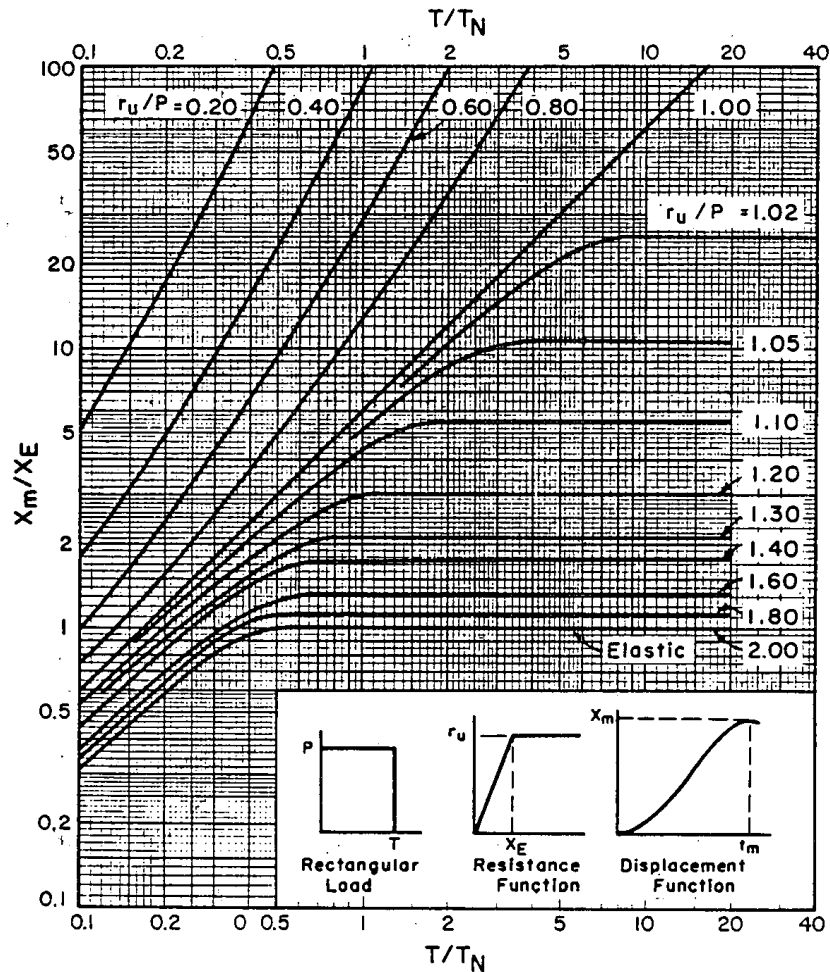
Fig. 3: Chart to calculate maximum deflection response X_m (from [10] fig. 3.56) attained at time t_m. The blast load is defined by its duration T and peak value P. The SDOF elastic deflection is X_E and r_u is its ultimate resistance, finally its natural period is T_N.

In the fifties, knowledge in this field increased, and the elastic-plastic model was considered. In an early work, Seiler et al. [47] modelled, by means of SDOF, a simply-supported beam under impulsive loading. They assumed that the initial velocity was a half sine wave. In this case, a simple mass-spring system can model the behaviour of elastic-plastic and rigid-plastic beams in order to develop a comparison between the two approaches. Then Brooks and Newmark, in [48], investigated numerous dynamic structural problems. In particular, Newmark [49]-[51] was an influential proponent of the modal method, having calculated several modal period formulas and corresponding stiffness and strength expressions.

According to Morison [45], this method presents two drawbacks:

1. A lack of versatility due to the fact that charts and diagrams based on it were developed only for some specific load time-histories.
2. Inadequate treatment of reaction forces. This method considers only forcing function distributed spatially with the same shape as the vibration shape, and this leads to underestimation of the reaction at member supports. In addition, this problem precludes suitable dynamic shear design for reinforced concrete members.

The equivalent SDOF method appeared in 1957 in the US Army Corps of Engineers manual "Design of structures to resist the effects of atomic weapons" [52], [53]. This method relies on calculation of SDOF parameters based on the equivalence of energy: the equivalent mass must have equal kinetic energy, the equivalent resistance must have equal internal strain energy and the equivalent loading must have equal external work to the real distributed element. These equivalent factors can be calculated for different structures with different boundary and loading conditions. In Fig. 4, some examples are shown of the value of the load factor K_L, mass factor K_M and other parameters of the equivalent SDOF for simply-supported beams.
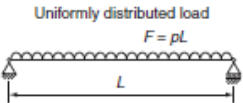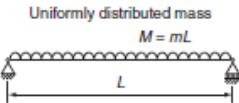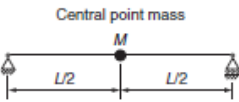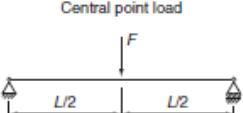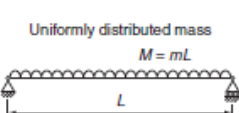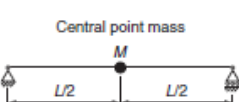
Loading diagram	Mass diagram	Strain range	Load factor, K_L	Mass factor, K_M	Load–mass factor, K_{LM}	Maximum resistance, R_m	Stiffness, k	Support shear, V_s	Ultimate shear stress, v	Dynamic reaction, V
Uniformly distributed load $F = pL$	Uniformly distributed mass $M = mL$	Elastic	0.64	0.50	0.78	$\frac{8M_p}{L}$	$\frac{384EI}{5L^3}$	$\frac{R_m}{2}$	$R_m\left(\frac{1}{2d_e} - \frac{1}{L}\right)$	$0.39R + 0.11F$
		Plastic	0.50	0.33	0.66	$\frac{8M_p}{L}$	0			$0.38R_m + 0.12F$
	Central point mass M	Elastic	0.64	1.0	1.56	$\frac{8M_p}{L}$	$\frac{384EI}{5L^3}$	$\frac{R_m}{2}$	$R_m\left(\frac{1}{2d_e} - \frac{1}{L}\right)$	$0.50R$
		Plastic	0.50	1.0	2.0	$\frac{8M_p}{L}$	0			$0.50R_m$
Central point load F	Uniformly distributed mass $M = mL$	Elastic	1.0	0.49	0.49	$\frac{4M_p}{L}$	$\frac{48EI}{L^3}$	$\frac{R_m}{2}$	$\frac{R_m}{2d_e}$	$0.78R - 0.28F$
		Plastic	1.0	0.33	0.33	$\frac{4M_p}{L}$	0			$0.75R_m - 0.25F$
	Central point mass M	Elastic	1.0	1.0	1.0	$\frac{4M_p}{L}$	$\frac{48EI}{L^3}$	$\frac{R_m}{2}$	$\frac{R_m}{2d_e}$	$0.50R$
		Plastic	1.0	1.0	1.0	$\frac{4M_p}{L}$	0			$0.50R_m$

Fig. 4: Equivalent SDOF factors for simply-supported beams (from [6] table A1).

In order to illustrate the procedure to obtain factors presented in Fig. 4, consider the case of elastic simple supported beam with uniformly distributed load p. First of all it is necessary to determine a deflected shape. A good approximation can be the beam static deflected shape corresponding to the particular load distribution (see Biggs [54], § 5.2). In this case it yields:

$$\phi(x) = \frac{16}{5L^2}\left(L^3 x - 2Lx^3 + x^4\right)$$

(3)

Where L is the span length and x represents the position along the beam. It can be proved by means of the equivalence of the kinetic energy of the equivalent SDOF and of the beam, or by some modal considerations (see Biggs [54], § 3.7) that the equivalent mass is:

$$M_e = \int_0^L \mu\phi^2(x)dx$$

(4)

Where μ represents the mass per unit length of the beam and ϕ is the shape function. Considering that the total mass of the beam is μL, the equivalent mass factor K_M is expressed by the following Eq. (5).

$$K_M = \frac{M_e}{\mu L}$$

(5)

Taking into account the shape function ϕ defined by Eq. (3) is easy to determine the numerical value of the mass factor K_M equal to 0.50.

Regarding the load factor K_L consider the equivalence of the work done by the external loads in case of SDOF and of real beam. This consideration leads to Eq. (6).

$$K_L = \frac{\int_0^L p(x)\phi(x)dx}{pL}$$

(6)

In this case the numerical value of the load factor K_L is 0.64.

Furthermore, the stiffness factor K_s is defined by means of strain energy equivalence. Actually, despite coming from different physical considerations, it has mostly the same value of load factor K_L. For this reason it is often convenient to define an unique load-mass factor K_{LM} :

$$K_{LM} = \frac{K_M}{K_L}$$

(7)

Referring to the assumed hypothesis in this case its numerical value is 0.78.

The accuracy of the equivalent SDOF method depends on the assumed deflected shape of the distributed element. In other words, due to the fact that energy equivalence is assessed referring to a particular deflection shape, the approximation inherent in this methodology is strictly linked to this shape. From a theoretical point of view, all deflected shapes consistent with support conditions may be assumed, but for practical reasons (computational effort and elastic-plastic behaviour), the static deflected shape is the most common approximation used, as highlighted by Morison [45]. In order to take even the plastic realm (and not only the elastic one) into account, different transformation factors are evaluated at different stages of the response. In this way, it is possible to consider the change in stiffness and strength due to the plasticization of some sections of the distributed element. In addition, the equivalent SDOF method involves dynamic equilibrium to calculate support reactions. In this way, it is possible to avoid problems inherent in the differences between lumped SDOF reactions and distributed element ones.

The equivalent SDOF method is a powerful tool to analyse distributed element response with some approximation, but it allows definition of: an idealised response chart for quickly determining

amplitude and time of peak response, dynamic load factor DLF in order to define the static load which gives the same elastic deflection as the dynamic one and the analytical and numerical solution of the equation of motion. A complete, effective presentation of this method is provided by Biggs [54].

In the last fifty years, several versions of this method were developed, and it is frequently used nowadays as well. In an interesting work [55], Fischer and Häring investigate minimization problems to determine parameters for the best practical SDOF model referring to dynamic deflection experimental data. Even strain rate effects (which will be discussed in §1.1.2) are taken into account by the SDOF model: Nassr et al. [56] develop SDOF analysis of steel beams, while Yang and Lok [57] present a new method to calculate the dynamic strength of R.C. structures, referring to SDOF models and suitable approximate formulas to evaluate structural response under blast load. Magnusson (already citied in the Introduction) also presents, in his licentiate thesis [58], SDOF analysis of his experimental results of R.C. beams subjected to blast load.

1.0.2.1 Dynamic Solution of Elastic-Plastic SDOF Equations of Motion

The most general expression of the dynamic equation of motion for a SDOF is:

$$m \cdot \ddot{u} + c \cdot \dot{u} + k \cdot u = P(t) \tag{8}$$
.

Where:

- m is the SDOF mass,
- c is the SDOF damping coefficient,
- k is SDOF stiffness,
- *P(t)* is the time history of the load,
- $\ddot{u}, \dot{u}, u$ are respectively the acceleration, velocity and displacement of the SDOF.

Damping effects are rarely significant for structural response under blast load; they have a negligible effect on SDOF maximum displacement (Baker et al. [59]). In addition, the energy absorbed by elastic-plastic deformation is greater than that dissipated in viscous damping. For these reasons, it is widely accepted to simplify Eq. (8), deleting the damping coefficient:

$$m \cdot \ddot{u} + k \cdot u = P(t) \tag{9}$$
.

The general solution in case of free vibration is expressed below:

$$u(t) = A\cos(\omega t) + B\sin(\omega t) \tag{10}$$
,

where ω is the circular frequency and is equal to *2π/T. T* is the period of the SDOF. *A* and *B* are coefficients depending on the initial conditions. After the derivations of Eq. (10), it is possible to obtain the expression of velocity and acceleration of the SDOF response:

$$\dot{u}(t) = -A\omega\sin(\omega t) + B\omega\cos(\omega t) \tag{11}$$

$$\ddot{u}(t) = -A\omega^2 \cos(\omega t) - B\omega^2 \sin(\omega t)$$.

(12)

After some rearrangements of Eqs. (11) and (12), it is possible to obtain:

$$\omega = \sqrt{\frac{k}{m}},$$

(13)

Due to Eq. (13), the SDOF period T can be expressed as:

$$T = 2\pi\sqrt{\frac{k}{m}},$$

(14)
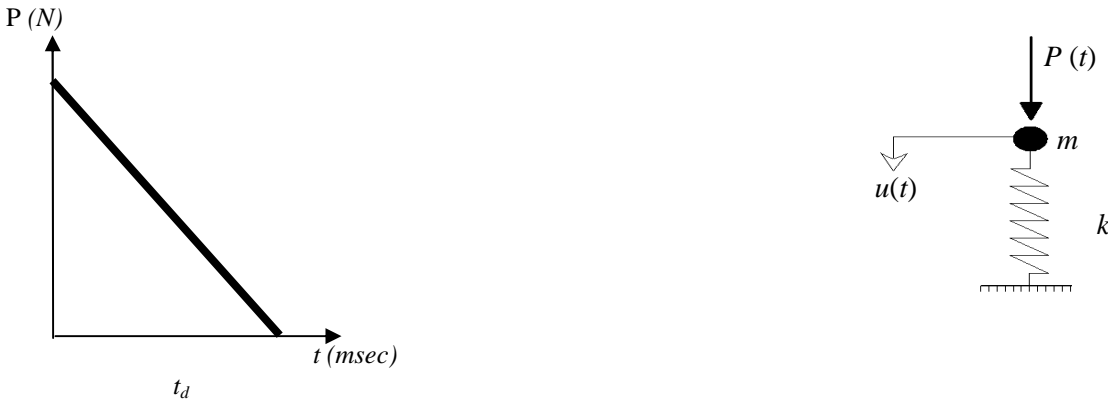
Fig. 5: Idealised blast load and Single Degree Of Freedom System.

Referring to the idealised triangular blast load time history, it is possible to distinguish three loading regimes depending on the ratio between the positive phase duration t_d (see Fig. 5) and the SDOF period T [6]:

 ➤ $\dfrac{t_d}{T} < 0.1$ impulsive

 ➤ $0.1 < \dfrac{t_d}{T} < 10$ dynamic

 ➤ $10 < \dfrac{t_d}{T}$ *quasi – static* .

For the sake of clarity in the following analysis, the SDOF resistance law will be an elastic-plastic one, as depicted in Fig. 6. In this figure, it is possible to identify an elastic field characterized by an elastic stiffness k_y and a plastic field characterized by another stiffness k_u.
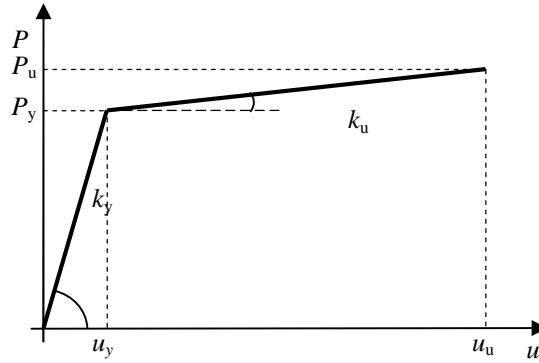
Fig. 6: Bilinear load-displacement diagram of the SDOF model.

In case of an impulsive load regime, Eq. (9) can be reformulated with its initial conditions by means of Eq. (15) concerning the elastic realm and Eq. (16) for the plastic realm.

$$\begin{cases} m \cdot \ddot{u} + k_y \cdot u = 0 & if \ u < u_y \\ u(0) = 0 \\ \dot{u}(0) = I/m \end{cases} \tag{15}$$

$$\begin{cases} m \cdot \ddot{u} + k_u \cdot u + (k_y - k_u)u_y = 0 & if \ u > u_y \\ u(t_y) = u_0 \\ \dot{u}(t_y) = \dot{u}_o \end{cases} \tag{16}$$

Where $\dot{u}_o$ and u_o respectively represent the velocity and the displacement corresponding to the transition from elastic to plastic realm, I represents the impulse of the blast load that can be defined with Eq. (17).

$$I = \int_0^{t_d} P(t)dt. \tag{17}$$

The elastic solution of Eq. (15) is expressed below:

$$u(t) = \frac{I}{m \cdot \omega_1} \sin(\omega_1 \cdot t) \quad where \quad \omega_1 = \sqrt{\frac{k_y}{m}}. \tag{18}$$

If the maximum displacement u_{MAX} is lower than the elastic limit u_y, Eq. (18) represents the solution to the dynamic problem. On the other hand, if u_{MAX} is higher than u_y, it is necessary to evaluate the initial conditions ($u(t_y)$ and $\dot{u}(t_y)$) of the plastic field and integrate Eq. (16).

In the case of a quasi-static regime, the forcing function is approximated as a constant force $P(t)=P$. The problem can be expressed by the following Eqs. (19) and (20), regarding respectively the elastic and plastic realm.

$$\begin{cases} m \cdot \ddot{u} + k_y \cdot u = P & if \ u < u_y \\ u(0) = 0 \\ \dot{u}(0) = 0 \end{cases} \tag{19}$$

$$\begin{cases} m \cdot \ddot{u} + k_u \cdot u + (k_y - k_u) u_y = P & if \ u > u_y \\ u(t_y) = u_0 \\ \dot{u}(t_y) = \dot{u}_o \end{cases} \tag{20}$$

The elastic solution of Eq. (19) is simply:

$$u(t) = \frac{P}{k_y} \big(1 - \cos(\omega_1 \cdot t)\big) \quad where \quad \omega_1 = \sqrt{\frac{k_y}{m}} \,. \tag{21}$$

Considerations similar to the previous case can be made as concerns the elastic-plastic transition. After having determined the initial plastic condition ($u(t_y)$ and $\dot{u}(t_y)$), the solution of Eq. (20) is easily obtainable.

The situation of the dynamic regime is more complicated. From a mathematical point of view, it is necessary to solve a set of differential equations representing the various dynamic problems. First of all, it is important to define two different possible situations:

- Condition I- maximum displacement is reached during free vibration, after the end of the blast load.

- Condition II- maximum displacement is reached during the blast load.

In order to define these two different conditions, it is possible to refer to the ratio between T (the period of the SDOF) and t_d (the positive phase duration of the load). In §1.0.2.6 it is shown how to define the discriminating factor: if $T / 2.69534 > t_d$ (Condition I), three different cases can be developed, as shown in Fig. 7.
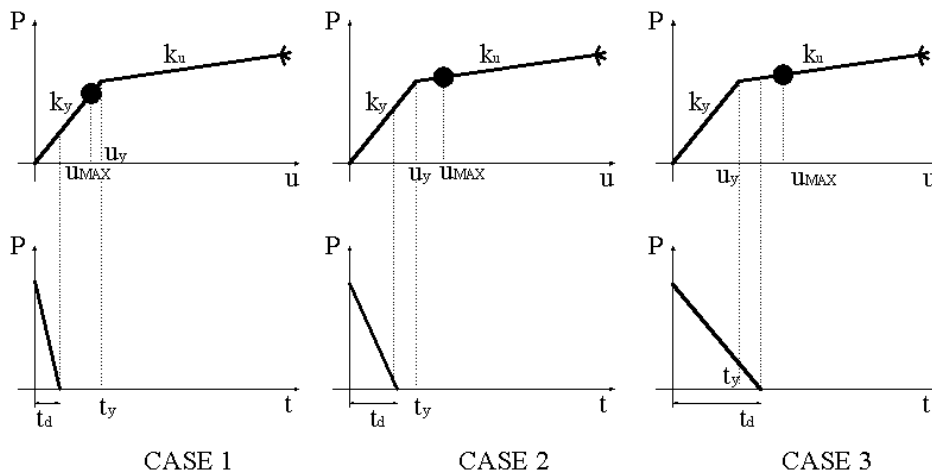
Fig. 7: Bilinear constitutive law of the SDOF and time history of the load for each of three cases.

<ins>1.0.2.2 Case 1: u$_{MAX}$<u$_y$:</ins>

In this case, the maximum displacement u_{MAX} is smaller than the elastic limit u_y and has to be defined the non-homogeneous problem (under the load) and the homogeneous one when the SDOF oscillates at natural frequencies. The equation of motion and its initial condition is expressed by Eq. (22).

$$\begin{cases} M_E \ddot{u} + k_y u = P\left(1 - \dfrac{t}{t_d}\right) \\ u(0) = 0 \\ \dot{u}(0) = 0 \end{cases} \qquad (22)$$

Given $\omega_1 = \sqrt{k_y/m}$, the solution of Eq. (22) is expressed in Eq. (23).

$$\begin{cases} u(t) = \dfrac{P}{k_y}\left(1 - \cos(\omega_1 t)\right) + \dfrac{P}{k_y \cdot t_d}\left(\dfrac{\sin(\omega_1 t)}{\omega_1} - t\right) \\ \dot{u}(t) = \dfrac{P\omega_1}{k_y}\left(\sin(\omega_1 t)\right) + \dfrac{P}{k_y \cdot t_d}\left(\cos(\omega_1 t) - 1\right) \end{cases} \qquad (23)$$

The displacement and velocity at the end of the blast load are calculated by Eq. (24) and become the initial conditions of the homogeneous problem (Eq.(25)). Its solution is also expressed in   Eq (26).

$$\begin{cases} u(t_d) = u_0 \\ \dot{u}(t_d) = \dot{u}_0 \end{cases} \qquad (24)$$

$$\begin{cases} M_E \ddot{u} + k_y u = 0 \\ u(0) = u_0 \\ \dot{u}(0) = \dot{u}_0 \end{cases} \qquad (25)$$

$$\begin{cases} u(t) = u_0 \cdot \cos(\omega_1 t) + \dfrac{\dot{u}_0}{\omega_1} \cdot \sin(\omega_1 t) \\ \dot{u}(t) = \dot{u}_0 \cdot \cos(\omega_1 t) - \omega_1 u_0 \cdot \sin(\omega_1 t) \end{cases} \qquad (26)$$

Now the maximum displacement is obtained by the optimization of Eq. (26), and the maximum velocity must be sought in both Eq. (23) and Eq. (26).

<ins>1.0.2.3 Case 2: u$_{MAX}$>u$_y$ and t$_d$<t$_y$:</ins>

In this case, the SDOF develops maximum displacement in the plastic field, but the blast load ends before the elastic-plastic transition occurs. The equations of motion and their initial conditions are

expressed in Eqs. (22) and (25). The solution of the last one (Eq. (26)) allows determination of the yielding instant t_y by means of Eq. (27).

$$u_y = u_0 \cdot \cos(\omega_1 t) + \frac{\dot{u}_0}{\omega_1} \cdot \sin(\omega_1 t) \Rightarrow t_y \quad \text{.} \tag{27}$$

Now this result is exploited in order to determine the initial condition of the free vibration problem in the plastic field (Eq. (28)), its equation of motion (Eq. (29)) and its solution Eq. (30). Note how Eq. (29) is not really homogeneous because, in the plastic field, the restoring force of the SDOF has a constant term equal to $(k_y - k_u)u_y$ as a consequence of the constitutive law in Fig. 7.

$$\begin{cases} u(t_y) = u_y = u_0 \\ \dot{u}(t_y) = \dot{u}_0 \end{cases} \tag{28}$$

$$\begin{cases} M_E \ddot{u} + k_u u + (k_y - k_u)u_y = 0 \\ u(0) = u_0 \\ \dot{u}(0) = \dot{u}_0 \end{cases} \tag{29}$$

Given $\omega_2 = \sqrt{k_u / m}$.

$$\begin{cases} u(t) = \left(u_0 + \frac{k_y - k_u}{k_u} u_y \right) \cdot \cos(\omega_2 t) + \frac{\dot{u}_0}{\omega_2} \cdot \sin(\omega_2 t) - \frac{k_y - k_u}{k_u} u_y \\ \dot{u}(t) = -\left(u_0 + \frac{k_y - k_u}{k_u} u_y \right) \cdot \omega_2 \cdot \sin(\omega_2 t) + \dot{u}_0 \cdot \cos(\omega_2 t) \end{cases} \tag{30}$$

Maximum displacement is obtained by the optimization of Eq. (30), and maximum velocity must be sought in Eq. (23), Eq. (26) and Eq. (30).

1.0.2.4 Case 3: $u_{MAX} > u_y$ and $t_d > t_y$:

Even in this case, the SDOF develops maximum displacement in the plastic field, but the blast load ends after the elastic-plastic transition occurs. The equations of motion and their initial conditions are expressed in Eq. (22). The solution of the last one (Eq.(23)) allows determination of the yielding instant t_y by means of Eq. (31).

$$u_y = \frac{P}{k_y}(1 - \cos(\omega_1 t)) + \frac{P}{k_y \cdot t_d}\left(\frac{\sin(\omega_1 t)}{\omega_1} - t \right) \Rightarrow t_y \tag{31}$$

The initial conditions of the plastic field equation of motion (Eq. (32)) are still expressed by Eq.(28), taking into account that now t_y is obtained from Eq. (31).

$$\begin{cases} M_E \ddot{u} + k_u u + \left(k_y - k_u\right) u_y = P\left(1 - \dfrac{t_y}{t_d}\right)\left(1 - \dfrac{t}{t_d - t_y}\right) \\ u(0) = u_0 = u_y \\ \dot{u}(0) = \dot{u}_0 \end{cases} \qquad (32)$$

Given $\alpha = \left(1 - t_y / t_d\right)$, $\beta = \left(k_y - k_u\right) u_y$, $\gamma = \alpha - \beta / k_u$, $\delta = \alpha / k_u \left(t_d - t_y\right)$, the solution of Eq. (32) represented in Eq. (33) is necessary to determine the initial condition (Eq. (34)) for the free vibration after the blast load.

$$\begin{cases} u(t) = \left(u_0 - \gamma\right)\cdot\cos\left(\omega_2 t\right) + \left(\dfrac{\delta}{\omega_2} + \dfrac{\dot{u}_0}{\omega_2}\right)\cdot\sin\left(\omega_2 t\right) - \delta t + \gamma \\ \dot{u}(t) = -\omega_2\left(u_0 - \gamma\right)\cdot\sin\left(\omega_2 t\right) + \left(\delta + \dot{u}_0\right)\cdot\cos\left(\omega_2 t\right) - \delta \end{cases} \qquad (33)$$

$$\begin{cases} u\left(t_d - t_y\right) = u_0 \\ \dot{u}\left(t_d - t_y\right) = \dot{u}_0 \end{cases} \qquad (34)$$

Then the problem has been taken back to Eq. (29) (obviously with different initial conditions from Case 2) and to its solution (Eq. (30)). The maximum displacement is obtained by the optimization of Eq. (30), and the maximum velocity must be sought in Eq. (23), Eq. (33) and Eq. (30).

1.0.2.5 Remaining cases

Condition II (characterised by $T / 2.69534 < t_d$) remains to be considered. In this case, the first displacement peak is reached before the end of the blast load. Two possibilities exist:

A. Maximum displacement is smaller than the yielding limit.
B. Maximum displacement is greater than the yielding limit, and the SDOF enters the plastic field.

Case A can be solved like Case 1, considering that maximum displacement and velocity are reached under the blast load (Eq. (23)) and not during free vibration.

Case B is similar to Case 3, but maximum displacement can be obtained from the optimization of Eqs. (30) and (33). Otherwise maximum velocity must be sought in Eq.(23), Eq. (33) and Eq. (30).

1.0.2.6 Discriminating factor $T/t_d = 2.69534$

In order to define the difference between conditions I and II, consider that if maximum displacement is reached under the blast load, the solution of equation (22) has a maximum between 0 and t_d. This means that the derivate of displacement (velocity) must be equal to 0 in these time ranges (see Eq. (35)).

$$\dot{u}(t) = \frac{P\omega_1}{k_y}\left(\sin(\omega_1 t)\right) + \frac{P}{k_y \cdot t_d}\left(\cos(\omega_1 t) - 1\right) = 0 \qquad (35)$$

.

Note that equation (35) is totally independent of peak pressure P and elastic stiffness k_y. By simple steps it develops into equation (36). Therefore, the solution of equation (36) is expressed with equation (37).

$$\sqrt{\left(\frac{2\pi}{T}\right)^2 + \left(\frac{1}{t_d}\right)^2}\cos\left(\frac{2\pi}{T}t - \arccos\left(\frac{\frac{1}{t_d}}{\sqrt{\left(\frac{2\pi}{T}\right)^2 + \left(\frac{1}{t_d}\right)^2}}\right)\right) = \frac{1}{t_d} \qquad (36)$$

$$t^* = \frac{T}{2\pi}\left(2\cdot\arccos\left(\frac{\frac{1}{t_d}}{\sqrt{\left(\frac{2\pi}{T}\right)^2 + \left(\frac{1}{t_d}\right)^2}}\right)\right) \qquad (37)$$

Now it must be ensured that the instant t^* is between 0 and the positive phase duration t_d (inequality (38)).

$$0 < \frac{T}{2\pi}\left(2\cdot\arccos\left(\frac{\frac{1}{t_d}}{\sqrt{\left(\frac{2\pi}{T}\right)^2 + \left(\frac{1}{t_d}\right)^2}}\right)\right) < t_d \qquad (38)$$

The inequality (38) is satisfied[4] for $0 < T/t_d < 2.69534$. This result was obtained numerically. Thus if the ratio between the period and positive phase duration is large enough ($T/t_d > 2.69534$), maximum displacement is reached after the end of the blast load (Condition I). If not, it is important to take into account that maximum displacement can be reached during the blast load (Condition II).

---

[4] This result is also confirmed by Clough and Penzien [60].

1.0.3 Modal Approximation models

As rightly stated by Zhu and Lu [21], *"modal solutions are of fundamental importance for explaining and estimating the deformation of structures that develop in response to impact or blasting loading."* The deformation caused by a blast load can be divided into an initial transient phase, where the pattern is continually changing, and a modal phase, where the pattern is constant. Velocity distribution evolves from the one imposed by the impact load to a mode configuration. Stronge and Yu [61] demonstrate that most of the impact energy is dissipated in a mode configuration during the modal phase of deformation.

An effective presentation of these models can be found in the work by Goldsmith [62]. This book, the first organized collection of analyses in the general impact field, had a significant influence upon publication, and attracted many researchers to that scientific problem. It is still one of the most important works available on impact phenomena.

An important contribution to the modal approach was made by Symonds [63], [64]. He referred to mild steel beams under pulse load and developed approximate theoretical solutions confining elastic effects to the initial stage with no plastic deformation and to residual vibration after lumped plastic deformation.

Some researchers like Yankelevsky [65] tried to model impulsively-loaded structures by considering rigid segments interconnected by plastic hinges; others (Hsu and Scheleyer [66]) referred to the equilibrium equation and its numerical solution.

There is as well an approach for distributed structural elements under blast load that also takes into account membrane action. The pioneering work by Symonds and Jones [67] was followed by several other papers: for example, Yeh [68] and, quite recently, Boutros [69].

After the development of computer science in the '80s, there were the development of advanced methods based on the multi-degree of freedom (MDOF) discretization, whereby the beam is divided into finite elements along its length. Nowadays, the finite element model is very common, and its solutions are often considered a benchmark in many studies. In the most sophisticated formulations, each finite element is also subdivided into fibres along its depth, in order to take into account the variation of the strain rate over the cross-section [70],[20].

1.0.3.1. Elastic Euler-Bernoulli Beam Theory

As stated in [71], *"the Euler-Bernoulli equation describes the relationship between the beam's deflection and the applied load"*:

$$\frac{d^2}{dx^2}\left(EJ \frac{d^2 u}{dx^2} \right) = q \tag{39}$$

Eq. (39) represents the static Euler-Bernoulli beam equation where:

- u is the deflection of the beam
- x is the longitudinal abscissa
- E is the elastic modulus
- J is the second moment of area

- q is the distributed load. Eq. (39) can be calculated assuming the following constitutive law for the beam material:

$$N = EA\varepsilon, \quad \gamma = 0, \quad M = EJ\chi.$$ (40)

Assuming the small displacement hypothesis, the kinematic conditions of congruence (and the definition of the strains in Eq. (40)) are the following:

$$\varepsilon = \frac{\partial s}{\partial x}, \quad \gamma = \frac{\partial u}{\partial x} + \varphi, \quad \theta = \frac{\partial \varphi}{\partial x}.$$ (41)

The displacements presented in Eq. (41) are defined in Fig. 8. The fundamental assumption of Euler-Bernoulli beam theory is that shear deformation can be neglected (as stated in Eq.(40)). For this reason, cross sections of the beams have planar rigid behaviour; in other words, they have to remain perpendicular to the longitudinal axis. Considering Eqs. (40) and (41) together:

$$0 = \frac{\partial u}{\partial x} + \varphi, \quad \varphi = -\frac{\partial u}{\partial x}$$ (42)

The displacement field (*u, s*) completely describes the kinematics of the Euler-Bernoulli beam. In other words, the deflected shape of the longitudinal axes contains all the information necessary to determine beam displacement.

Fig. 8: Displacement in the Euler-Bernoulli Beam Theory.

In order to express the dynamic Euler-Bernoulli beam equation, consider an infinitesimal section of the beam dx long without any axial force. The actions on this section are:

- Inertia forces dF_i
- Shear $T(x)$
- Bending Moment $M(x)$
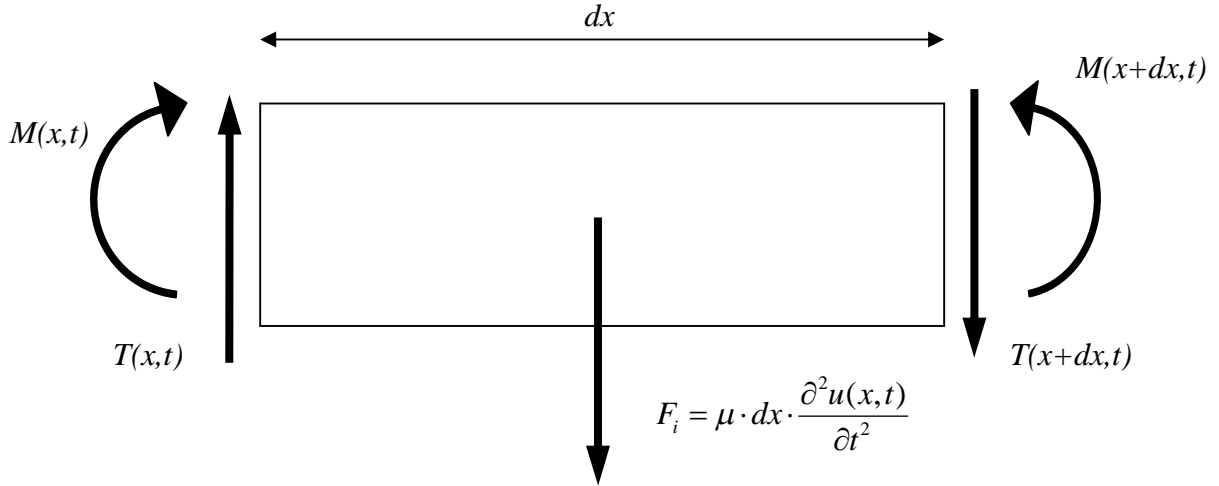
Fig. 9: Dynamic equilibrium of a section of the Euler-Bernoulli beam.

Fig. 9 represents the dynamic equilibrium of the forces and moment acting on an infinitesimal section of the Euler-Bernoulli beam. The rotational equilibrium yields:

$$\frac{\partial M(x,t)}{\partial x} = T(x,t) \quad .$$

(43)

Translational equilibrium is expressed by:

$$\frac{\partial T(x,t)}{\partial x} + \mu \frac{\partial^2 u(x,t)}{\partial t^2} = 0 \quad ,$$

(44)

and introducing Eq. (43) into Eq. (44):

$$EJ \frac{\partial^4 u(x,t)}{\partial x^4} + \mu \frac{\partial^2 u(x,t)}{\partial t^2} = 0 \quad .$$

(45)

Eq. (45) represents the homogenous dynamic equation of the Euler-Bernoulli beam, where *EJ* is the bending stiffness and μ is the specific mass. As stated by Frýba in [72], its solutions can be found assuming the following form:

$$u(x,t) = \sum_{j=1}^{\infty} u_j(x) \sin(\omega_i t) \quad .$$

(46)

In Eq. (46), u_j are the modes of natural vibration and ω_i are the natural circular frequencies of the beam. They are obviously equal to *2πf$_i$*. Inserting Eq. (46) into Eq. (45), it is possible to obtain Eq.(47).

$$EJ \sum_{j=1}^{\infty} \frac{d^4 u_j(x)}{dx^4} \sin(\omega_j t) - \mu \sum_{j=1}^{\infty} \omega_j^2 u_j(x) \sin(\omega_j t) = 0 \quad .$$

(47)

Eq.(47) is valid for each of the natural modes. It can be simplified into a set of independent,

ordinary differential equations. Referring to the j-th mode:

$$\frac{d^4 u_j(x)}{dx^4} - \frac{\mu \omega_j^2}{EJ} u_j(x) = 0 \quad j = 1, 2, 3... \quad . \tag{48}$$

Eq. (48) is often rewritten, introducing $\lambda = l^4 \dfrac{\mu \omega_j^2}{EJ}$:

$$\frac{d^4 u_j(x)}{dx^4} - \frac{\lambda_j^4}{l^4} u_j(x) = 0 \quad j = 1, 2, 3... \quad . \tag{49}$$

The general solution of Eq.(49) is:

$$u_j(x) = A_1 \sin\left(\frac{\lambda_j x}{l}\right) + A_2 \cos\left(\frac{\lambda_j x}{l}\right) + A_3 \sinh\left(\frac{\lambda_j x}{l}\right) + A_4 \cosh\left(\frac{\lambda_j x}{l}\right). \tag{50}$$

Where A_i, $_{i=1,2,3,4}$ are the integration constants that can be determined from the boundary conditions of the beam. For a simple supported beam of span l, these conditions are:

$$u_j(0) = 0, \quad u_j(l) = 0, \quad \frac{du_j^2(0,t)}{dx^2} = 0, \quad \frac{du_j^2(l,t)}{dx^2} = 0. \tag{51}$$

Inserting Eq. (50) into Eq. (51), a set of four independent equations is obtained:

$$\begin{cases} u_j(0) = A_2 + A_4 = 0 \\ u_j{}''(0) = \dfrac{\lambda_j^2}{l^2}\left(-A_2 + A_4\right) = 0 \\ u_j(l) = A_1 \sin \lambda_j + A_3 \sinh \lambda_j = 0 \\ u_j{}''(l) = \dfrac{\lambda_j^2}{l^2}\left(-A_1 \sin \lambda_j + A_3 \sinh \lambda_j\right) = 0 \end{cases} \tag{52}$$

Eq. (52) is satisfied when:

$$A_2 = A_3 = A_4 = 0 \quad and \quad \sin \lambda_j = 0, \tag{53}$$

Consequently, constant A_1 is arbitrary: natural vibration may occur at any amplitude. The right side of Eq. (53) is called *"frequency equation and is indicative for a simply-supported beams"* (see [72]):

$$\lambda_j = j\pi, \quad j = 1, 2, 3.... \tag{54}$$

$$\omega_j^2 = \frac{\lambda_j^4}{l^4} \frac{EJ}{\mu} \, , \tag{55}$$

$$f_j = \frac{\lambda_j^2}{2\pi l^2}\left(\frac{EJ}{\mu}\right)^{1/2} .$$

(56)

Natural circular frequencies and natural frequencies for a simply-supported beams are, respectively, expressed in Eq. (55) and Eq. (56). Therefore, as reported in [72], *according to* Eq. (46), *"a beam can vibrate in an infinite number of modes, but the simplest natural mode is the sine curve":*

$$u(x) = A_j \sin\left(\frac{j\pi x}{l}\right) .$$

(57)

In Table 1, following, the characteristics of natural vibrations of single-span beams of constant cross section with different support conditions are reported. The shapes of the natural modes with node positions are depicted in the subsequent Fig. 10 for some support conditions.

It is important to underline that the solution expressed in Eq. (57) is a singular solution. Vibrations without external forces do not have to simply be harmonic: they may be a combination of simple harmonic motions characterized by different frequencies and phases. Actually, natural vibrations are often distinguished from free vibrations. A complete solution of Eq. (45) is reported in [72] in the case of free vibrations for a simply-supported beam:

$$u(x,t) = \sum_{j=1}^{\infty} A_j \sin\left(\frac{j\pi x}{l}\right)\sin\left(\omega_j t + \varphi_j\right) ,$$

(58)

where φ_j is the phase of the j-th natural mode.

Beam Figure	Boundary conditions	No. of natural mode j	λ_j	Frequency equation	Natural vibration mode $u_j(x)$	A_j	Equation for A_j
Simple supported FIG…	$u_j(0)=0$ $u_j''(0)=0$ $u_j(l)=0$ $u_j''(l)=0$	1 2 3 4 5 >5	3.142 6.283 9.425 12.566 15.708 $j\pi$	$\sin\lambda_j = 0$	$\sin\dfrac{\lambda_j x}{l}$	- - - - - -	-
Both ends clamped FIG	$u_j(0)=0$ $u_j'(0)=0$ $u_j(l)=0$ $u_j'(l)=0$	1 2 3 4 5 >5	4.730 7.853 10.996 14.137 17.279 $(2j+1)\pi/2$	$\cos\lambda_j\cosh\lambda_j = 1$	$\cosh\dfrac{\lambda_j x}{l}+$ $-\cos\dfrac{\lambda_j x}{l}+$ $-A_j(\sinh\dfrac{\lambda_j x}{l}+$ $-\sin\dfrac{\lambda_j x}{l})$	0.983 1.001 1 1 1 1	$(\cosh\lambda_j + -\cos\lambda_j)/ (\sinh\lambda_j + -\sin\lambda_j)$
Boths ends free FIG	$u_j''(0)=0$ $u_j'''(0)=0$ $u_j''(l)=0$ $u_j'''(l)=0$	The same as for beam with both ends clamped			$\cosh\dfrac{\lambda_j x}{l}+$ $+\cos\dfrac{\lambda_j x}{l}+$ $-A_j(\sinh\dfrac{\lambda_j x}{l}+$ $+\sin\dfrac{\lambda_j x}{l})$	The same as for beam with both ends clamped	
Cantilever	$u_j(0)=0$ $u_j'(0)=0$ $u_j''(l)=0$ $u_j'''(l)=0$	1 2 3 4 5 >5	1.875 4.694 7.855 10.996 14.137 $(2j-1)\pi/2$	$\cos\lambda_j\cosh\lambda_j = -1$	$\cosh\dfrac{\lambda_j x}{l}+$ $-\cos\dfrac{\lambda_j x}{l}+$ $-A_j(\sinh\dfrac{\lambda_j x}{l}+$ $-\sin\dfrac{\lambda_j x}{l})$	0.734 1.018 0.999 1 1 1	$(\sinh\lambda_j + -\sin\lambda_j)/ (\cosh\lambda_j + +\cos\lambda_j)$
One end clamped, one end simply supported	$u_j(0)=0$ $u_j'(0)=0$ $u_j''(l)=0$ $u_j(l)=0$	1 2 3 4 5 >5	3.927 7.069 10.210 13.352 16.493 $(4j+1)\pi/2$	$\text{tg}\lambda_j=\text{tgh}\lambda_j$	$\cosh\dfrac{\lambda_j x}{l}+$ $-\cos\dfrac{\lambda_j x}{l}+$ $-A_j(\sinh\dfrac{\lambda_j x}{l}+$ $-\sin\dfrac{\lambda_j x}{l})$	1.001 1 1 1 1 1	$\cot g\lambda_j$

Table 1: Characteristics of natural vibrations of single-span beams of constant cross-section (extracted from [72] §Table 4.1).
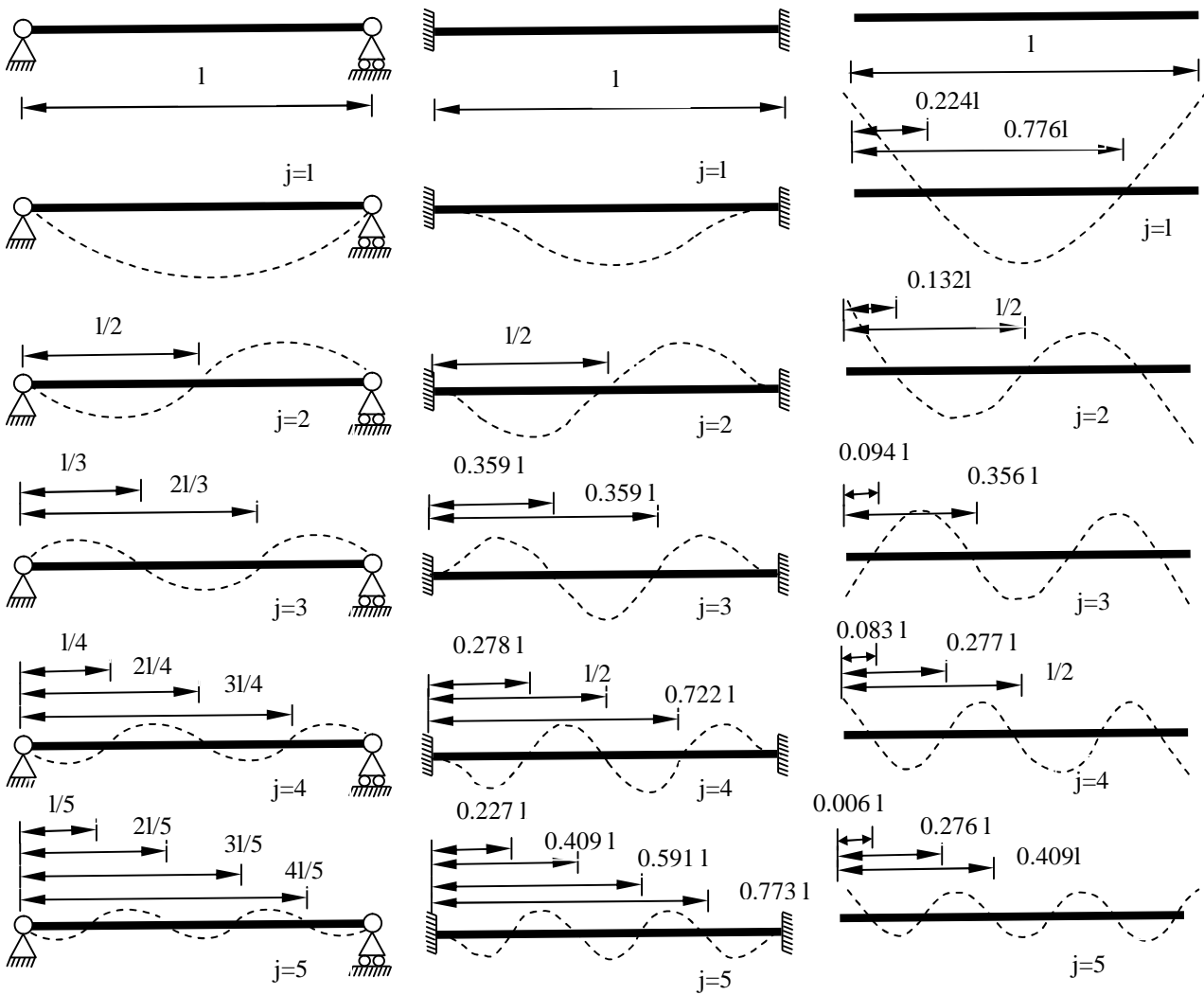
Fig. 10: Modes of natural vibration for beams with different support conditions (extracted from [72] §Fig.4.1-4.3).

In case of blast load, a suitable model for the pressure time history is the triangular pulse shown in Fig. 5. If the charge is at a sufficient distance, it is possible to consider the load uniformly distributed along the beam, and the equation of motion of the Euler-Bernoulli beam becomes:

$$EJ\frac{\partial^4 u(x,t)}{\partial x^4} + \mu\frac{\partial^2 u(x,t)}{\partial t^2} = \frac{q}{t_d}(t-t_d)\big(H(t)-H(t-t_d)\big) \quad . \qquad (59)$$

Where q is the peak of the uniformly-distributed blast load, t_d is the positive phase duration and H is the Heaviside step defined below:

$$H(t) = \begin{cases} 0, & t < 0 \\ 1, & t > 0 \end{cases} \qquad (60)$$

It is necessary to use the Heaviside step in order to have a unique load function without

- 42 -

distinguishing between load time and free vibration time. In addition, the definition of the Fourier Transform (Eq. (61)) and Laplace Carson Transform (Eq.(62)) are useful. Actually, there are techniques similar to those previously shown for free vibration, also for the solution of Eq. (59). Nevertheless, for the sake of brevity and in order to show other methodologies by means of the following steps, the solution of Eq. (59) will be found by referring to the previously-cited Transforms.

$$F(j) = \int_0^l f(x) \sin\left(\frac{j\pi x}{l}\right) dx \qquad (61)$$
,

$$\tilde{F}(p) = p \int_0^\infty f(t) e^{-tp} dt \qquad (62)$$
.

Taking into account Eqs. (54) and (55) and applying the Fourier Transform, Eq. (63) is obtained:

$$U(n,t)\cdot\omega_n^2 + \ddot{U}(n,t) = \frac{1-\cos(n\pi)}{n\pi\mu}\left[\frac{q}{t_d}(t-t_d)\big(H(t)-H(t-t_d)\big)\right] \qquad (63)$$

Where $U(n,t)$ is the Fourier Transform of the deflection $u(x,t)$. The application of the Laplace-Carson transform to Eq. (63) produces:

$$\tilde{U}(n,p)\cdot\omega_n^2 + p^2\tilde{U}(n,p) = \frac{1-\cos(n\pi)}{n\pi\mu}\frac{ql}{t_d}\left\{1-\frac{1}{p}+\left(\frac{1}{p}-t_d\right)e^{-pt_d}\right\} \qquad (64)$$

Where $\tilde{U}(n,p)$ is the Laplace-Carson Transform of the Fourier Transform of the deflection $u(x,t)$. Now it is quite easy to determine the solution in the Laplace-Carson realm by simply rearranging the terms in Eq. (71):

$$\tilde{U}(n,p) = \frac{1}{\omega_n^2 + p^2}\cdot\frac{1-\cos(n\pi)}{n\pi\mu}\cdot\frac{ql}{t_d}\left\{t_d-\frac{1}{p}+\left(\frac{1}{p}-t_d\right)e^{-pt_d}\right\} \qquad (65)$$

The inverse Laplace-Carson of the solution expressed in Eq. (65) can be obtained with the tables reported in Frýba [73] or with its analytical definition:

$$f(t) = \frac{1}{2\pi i}\int_{a-i\infty}^{a+i\infty}\frac{F(p)}{p}e^{tp}dp \qquad (66)$$
.

The inverse Laplace-Carson of the function defined in Eq. (65) is shown below:

$$U(n,t) = \frac{(1-\cos(n\pi)) \cdot ql}{n\pi\mu} \left\{ \begin{array}{l} \frac{1}{\omega_n^2}\left[1-\left(1-\cos(\omega_n t)\right)\right] - \frac{1}{t_d}\frac{1}{\omega_n^3}\left(\omega_n t - \sin(\omega_n t)\right) + \\ + \frac{H(t-t_d)}{t_d}\left[\frac{1}{\omega_n^3}\left(\begin{array}{l}\omega_n(t-t_d) - \sin(\omega_n(t-t_d)) + \\ -\frac{t_d}{\omega_n^2}\left(1-\cos(\omega_n(t-t_d))\right)\end{array}\right)\right] \end{array} \right\} \qquad (67)$$

$$f(x) = \frac{2}{l}\sum_{j=1}^{\infty} F(j)\sin\left(\frac{j\pi x}{l}\right). \qquad (68)$$

Introducing the inverse Fourier transform, (see Eq. (68)) it is possible to obtain the solution in the time realm:

$$u(x,t) = \frac{2}{l}\sum_{j=1}^{\infty}\frac{(1-\cos(n\pi)) \cdot ql}{n\pi\mu}\left\{\begin{array}{l}\frac{1}{\omega_n^2}\left[1-\left(1-\cos(\omega_n t)\right)\right] - \frac{1}{t_d}\frac{1}{\omega_n^3}\left(\omega_n t - \sin(\omega_n t)\right) + \\ + \frac{H(t-t_d)}{t_d}\left[\frac{1}{\omega_n^3}\left(\begin{array}{l}\omega_n(t-t_d) - \sin(\omega_n(t-t_d)) \\ + -\frac{t_d}{\omega_n^2}\left(1-\cos(\omega_n(t-t_d))\right)\end{array}\right)\right]\end{array}\right\}\sin\left(\frac{j\pi x}{l}\right) \quad (69)$$

.

Eq. (69) represents the solution of the dynamic equation of an elastic Euler-Bernoulli beam. The procedure obviously becomes more complicated when geometry and material nonlinearities are taken into account. For example, as done for the SDOF, it is possible to consider a non-linear relationship between moment and curvature, considering the plastic realm. In §1.3, a continuous beam model based on the Euler-Bernoulli equation is presented, and in that case material nonlinearities are taken into account, considering the strain-rate effect and elastic-plastic behaviour.

1.0.4 Experimental Results

Experimental results on structural elements subjected to blast loads are rarely found in the literature. This is due not only to national security reasons (the diffusion of knowledge on this topic is often limited by countries for defence purposes), but also to the fact that experiments of this kind are costly and difficult to carry out. Fortunately, there are some remarkable exceptions. For instance, Hudson and Darwin [74] damaged several reinforced concrete beams using explosives and, after strengthening some of them with carbon fibres-reinforced polymers, examined whether repaired beams exhibited enhanced flexural capacity with respect to unrepaired ones. Magnusson and Hallgren [16] - [20] subjected many reinforced concrete beams made of normal or high-strength concrete, with or without steel fibres, to air blast-loading; they discovered that beams with a high reinforcement ratio and without steel fibres failed in shear, while those with a low reinforcement ratio failed in flexure. It is also important to mention the experimental work by Remennikov and Kaewunruen [75], Fujikake et al. [70] and Tachibana et al. [76], in which reinforced concrete beams under impact loads were investigated, along with contributions by Alves and Jones [77], Lawver et al. [78] and Nassr et al. [56], who analyzed the behaviour of steel members under impact or blast loads; though quite interesting, the results of these studies are not considered in the

present thesis, since they are irrelevant to the scope of this work.

This introduction was necessary to describe in a synthetic way the state of the art of such a wide scientific field. In the following part of Section 1, the nonlinear dynamic models developed by the author will be explained and discussed.

Chapter 1.1 Material and Sectional Models

First of all, the constitutive properties of the materials from which the RC beam is made should be specified. They are extracted from fib Bulletin n. 55 [79]. In particular, the uniaxial stress-strain relation of concrete is given by ([79],§ 5.1.8.1).

$$\sigma_c = f_{cm} \frac{k \cdot \varepsilon_c / \varepsilon_{c1} - (\varepsilon_c / \varepsilon_{c1})^2}{1 + (k-2) \cdot \varepsilon_c / \varepsilon_{c1}} \quad \text{for } |\varepsilon_c| < |\varepsilon_{c,lim}| \tag{70}$$

where σ_c (<0) and ε_c (<0) are respectively concrete compressive stress and strain, while f_{cm}, ε_{c1}, $\varepsilon_{c,lim}$ and k are quantities depending on the concrete grade ([79],Table 5.1-8). The compressive stress-strain diagram of concrete for a generic concrete grade is shown in Fig. 11a. It should be pointed out that the tensile strength of concrete is disregarded.

The uniaxial behaviour of reinforcing steel (both in tension and in compression) is approximated by an elastic-perfect plastic diagram, as shown in Fig. 11b ([79]§ 5.2.9). In this figure, E_s denotes Young's steel modulus, f_{yk} indicates its yield strength and ε_{sy} stands for its yield strain.
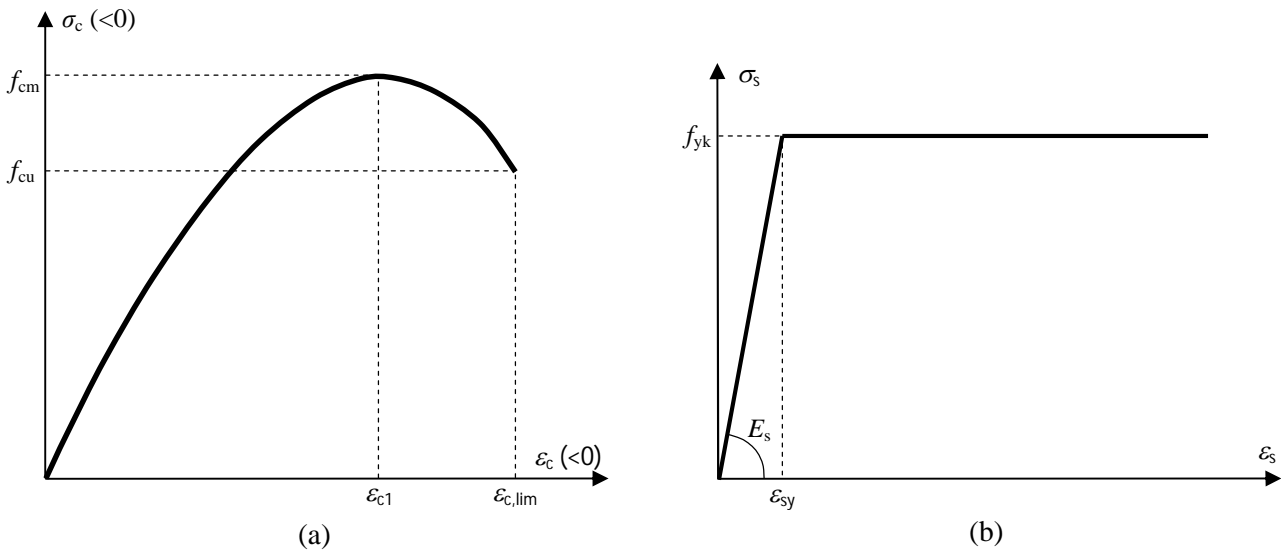
Fig. 11: Stress-strain diagrams for concrete (a) and reinforcing steel (b) adopted in this work.

It is assumed that the yield state of the beam is reached as soon as stress in the tensile reinforcement σ_s equals yield strength f_{yk}. The neutral axis depth at the yield state, denoted by x_y, can be obtained by imposing translational equilibrium. Referring to Fig. 12, where a doubly-reinforced concrete beam is considered, translational equilibrium requires that the following equation be fulfilled at each instant of time:

$$b\int_0^{x_y} \sigma_c \, dy + \sigma_{ss} A_{ss} = f_{yk} A_s \tag{71}$$

Here the subscripts "s" and "ss" are appended to quantities respectively corresponding to tensile and compressive reinforcements, while the subscript "c" refers to concrete. The meanings of all geometric quantities relative to the beam cross-section can be inferred from Fig. 3a. By inserting into Eq.(71) the expression of σ_c given by Eq.(70) and by using the linear strain diagram plotted in Fig. 12c, Eq. (71) becomes[5]:

$$b f_{cm} \int_0^{x_y} \left[\frac{k \frac{\varepsilon_{sy}}{\varepsilon_{c1}} \frac{x_y - y}{d - x_y} - \left(\frac{\varepsilon_{sy}}{\varepsilon_{c1}} \frac{x_y - y}{d - x_y} \right)^2}{1 + (k-2) \frac{\varepsilon_{sy}}{\varepsilon_{c1}} \frac{x_y - y}{d - x_y}} \right] dy + E_s \varepsilon_{sy} \frac{x_y - d'}{d - x_y} A_{ss} = f_{yk} A_s \tag{72}$$

from which neutral axis depth at the yield state (x_y) can be calculated. The resistant bending moment of the section at the yield state (M_y) may be determined from the equilibrium of rotation around the tensile reinforcement, leading to the following formula:

$$M_y = b \int_0^{x_y} \sigma_c (d - y) \, dy + \sigma_{ss} A_{ss} (d - d') =$$

$$= b f_{cm} \int_0^{x_y} \left[\frac{k \frac{\varepsilon_{sy}}{\varepsilon_{c1}} \frac{x_y - y}{d - x_y} - \left(\frac{\varepsilon_{sy}}{\varepsilon_{c1}} \frac{x_y - y}{d - x_y} \right)^2}{1 + (k-2) \frac{\varepsilon_{sy}}{\varepsilon_{c1}} \frac{x_y - y}{d - x_y}} \right] (d - y) \, dy + E_s \varepsilon_{sy} \frac{x_y - d'}{d - x_y} A_{ss} (d - d'). \tag{73}$$
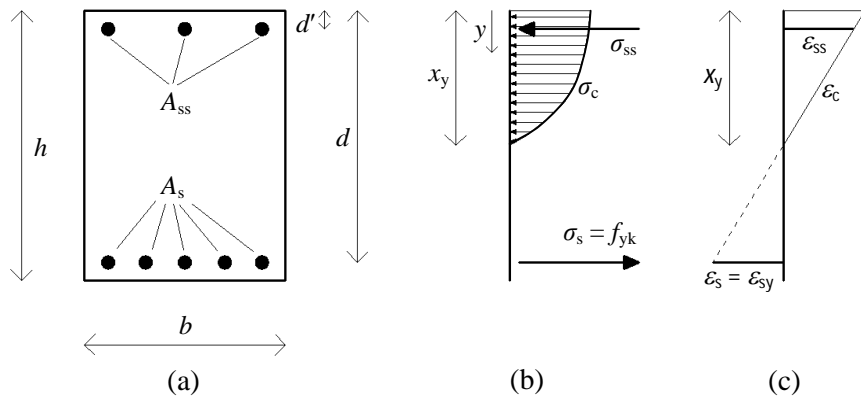
Fig. 12: (a) Sketch of the cross-section of a doubly-reinforced concrete beam; (b) stress diagram at the yield state; (c) strain diagram at the yield state.

---

[5] It is supposed that $\sigma_{ss} < f_{yk}$, as usually occurs; if not, σ_{ss} should be substituted by f_{yk}. The same consideration applies to Eq. (73).

The ultimate state is reached, however, when concrete attains its maximum strain $\varepsilon_{c,lim}$. In this case, the stress and strain diagrams over the cross-section are those respectively depicted in Fig. 13a and Fig. 13b. Neutral axis depth at the ultimate state (x_u) can be calculated again from the translational equilibrium condition, which, after using Eq. (70) and the linear strain diagram in Fig. 13b, is given by one of the following two equations:

$$b\,f_{cm}\int_0^{x_u}\left[\frac{k\dfrac{\varepsilon_{c,lim}}{\varepsilon_{c1}}\dfrac{x_u-y}{x_u}-\left(\dfrac{\varepsilon_{c,lim}}{\varepsilon_{c1}}\dfrac{x_u-y}{x_u}\right)^2}{1+(k-2)\dfrac{\varepsilon_{c,lim}}{\varepsilon_{c1}}\dfrac{x_u-y}{x_u}}\right]dy+E_s\,\varepsilon_{c,lim}\frac{x_u-d'}{x_u}A_{ss}=f_{yk}A_s \quad \text{if } \sigma_{ss}<f_{yk} \quad (a)$$

$$b\,f_{cm}\int_0^{x_u}\left[\frac{k\dfrac{\varepsilon_{c,lim}}{\varepsilon_{c1}}\dfrac{x_u-y}{x_u}-\left(\dfrac{\varepsilon_{c,lim}}{\varepsilon_{c1}}\dfrac{x_u-y}{x_u}\right)^2}{1+(k-2)\dfrac{\varepsilon_{c,lim}}{\varepsilon_{c1}}\dfrac{x_u-y}{x_u}}\right]dy+f_{yk}A_{ss}=f_{yk}A_s \quad \text{if } \sigma_{ss}\geq f_{yk} \quad (b)$$

(74)

Rotational equilibrium around the tensile reinforcement expresses the resistant bending moment at the ultimate state (M_u):

$$M_u=b\,f_{cm}\int_0^{x_u}\left[\frac{k\dfrac{\varepsilon_{c,lim}}{\varepsilon_{c1}}\dfrac{x_u-y}{x_u}-\left(\dfrac{\varepsilon_{c,lim}}{\varepsilon_{c1}}\dfrac{x_u-y}{x_u}\right)^2}{1+(k-2)\dfrac{\varepsilon_{c,lim}}{\varepsilon_{c1}}\dfrac{x_u-y}{x_u}}\right](d-y)\,dy+E_s\,\varepsilon_{c,lim}\frac{x_u-d'}{x_u}A_{ss}(d-d') \quad \text{if } \sigma_{ss}<f_{yk} \quad (a)$$

(75)

$$M_u=b\,f_{cm}\int_0^{x_u}\left[\frac{k\dfrac{\varepsilon_{c,lim}}{\varepsilon_{c1}}\dfrac{x_u-y}{x_u}-\left(\dfrac{\varepsilon_{c,lim}}{\varepsilon_{c1}}\dfrac{x_u-y}{x_u}\right)^2}{1+(k-2)\dfrac{\varepsilon_{c,lim}}{\varepsilon_{c1}}\dfrac{x_u-y}{x_u}}\right](d-y)\,dy+f_{yk}A_{ss}(d-d') \quad \text{if } \sigma_{ss}\geq f_{yk} \quad (b)$$

(a)   (b)
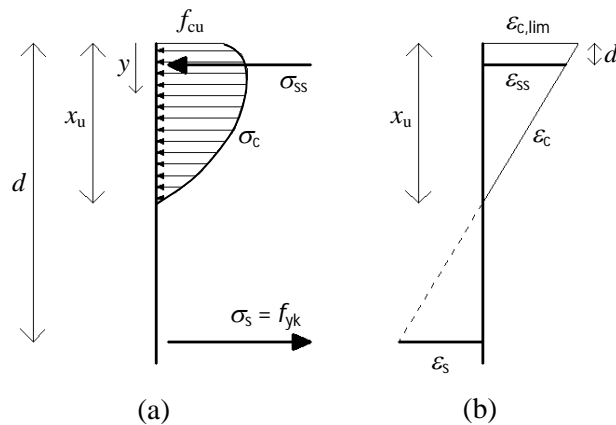
Fig. 13: (a) Stress distribution over the cross-section at the ultimate state; (b) strain diagram at the ultimate state.

Determination of x_y, M_y, x_u and M_u allows definition of the bilinear bending moment-curvature diagram of the RC beam, illustrated in Fig. 14a. In this figure, θ_y and θ_u denote curvatures at the yield and ultimate states, given by:

$$\theta_y = \frac{\varepsilon_{sy}}{d - x_y} \qquad (76)$$

and

$$\theta_u = \frac{\varepsilon_{c,lim}}{x_u} \qquad (77)$$

respectively.

The next step is to specify the nonlinear sectional behaviour of the RC beam. In practical applications, for an under-reinforced concrete beam, a bilinear relationship[6] between bending moment and curvature is commonly assumed. It is usually defined by the previously-established characteristic point (yielding, ultimate). Though quite convenient from a computational point of view, this relationship hardly mimics the real behaviour of the beam, which rarely exhibits a clear-cut transition between the elastic and plastic deformation regimes. Therefore, in this work, a smoother relationship between the bending moment M and curvature θ is introduced, which reads:

$$M = \bar{M} \tanh\left(\frac{\bar{K}}{\bar{M}} \theta\right) = -\bar{M} \tanh\left(\frac{\bar{K}}{\bar{M}} \frac{\partial^2 u}{\partial x^2}\right) \qquad (78)$$

The hyperbolic tangent function is used in Eq.(78) because it presents no slope discontinuity and it is capable of fitting a bilinear function well, with proper choice of its coefficients. The parameters $\bar{M}$ and $\bar{K}$ appearing in Eq.(78), respectively representing the equivalent ultimate bending moment and the initial flexural rigidity of the beam, depend on the sectional and constitutive properties of the beam (as will be illustrated below). The minus sign in front of the right-hand term takes into account that a positive bending moment (which, conventionally, causes compression in top fibers and tension in bottom ones) produces negative curvature in the reference system usually chosen (see Fig. 18). It should be observed that the right-hand term of Eq.(78) is obtained by assuming small deformation and rotation in the beam.

The parameters $\bar{M}$ and $\bar{K}$, appearing in Eq.(78), can be determined from values of the neutral axis depth and bending moment at the yield and ultimate states. More specifically $\bar{K}$, which represents the slope of the diagram plotted in Fig. 14b at $\theta = 0$, can be calculated by this ratio:

---

[6] A more sophisticated approach would be to adopt a trilinear relationship between bending moment and curvature, which would also take into account the initial state before concrete cracking occurs. Here this initial state is not considered, since the tensile strength of concrete is disregarded, as previously stated.

$$\bar{K} = \frac{M_y}{\theta_y} \tag{79}$$

Parameter $\bar{M}$, representing the equivalent ultimate bending moment, can be obtained by equating areas A_1 and A_2 under the curves shown respectively in Fig. 14a and Fig. 14b. The equivalence of A_1 and A_2 leads to the following equation:

$$\frac{\bar{M}^2}{\bar{K}} \ln\left[\cosh\left(\frac{\bar{K}}{\bar{M}} \theta_u \right) \right] = \frac{M_u \left(\theta_u - \theta_y \right) + M_y \theta_u}{2} \tag{80}$$

where the left-hand term was obtained by integrating Eq.(78). In this way, the bilinear bending moment-curvature relationship can be substituted by a smoother diagram, better approximating the real behaviour of the beam. In fact, the bending moment–curvature diagram of a real RC beam presents a gradual change in slope when yielding of the tensile reinforcement occurs, as in Fig. 14b, and hence there are no tangent discontinuities, as in Fig. 14a. For this reason, the diagram in Fig. 14b is preferable to the one in Fig. 14a.
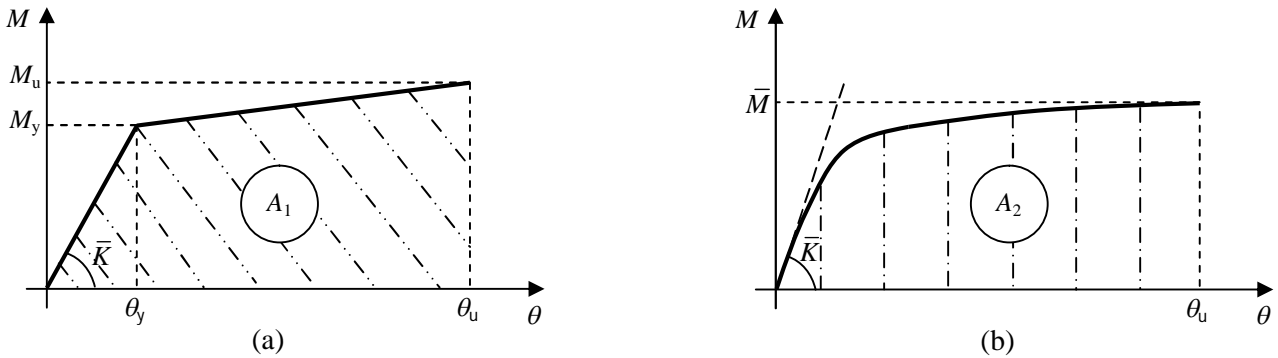
Fig. 14: (a) Bilinear bending moment-curvature relation; (b) smoother bending moment-curvature diagram adopted in this work

1.1.2 Strain-rate effects

The constitutive quantities introduced in the previous section are valid only in a static regime. Since dynamic loads are considered in this work and since concrete and steel are strain-rate sensitive materials, static constitutive quantities are updated by using the relationships provided by the *CEB Information Bulletin n.187* [82](also refer to the recent paper by Asprone et al.[83]).

First, the strain rates of concrete and steel reinforcements are easily determined by knowing the curvature rate and the value of the neutral axis depth. Next, the dynamic properties of concrete and steel reinforcements are evaluated.

As regards concrete ([82],§ 3.3.1), its dynamic strength is given by:

$$f_{cm,dyn} = f_{cm} \cdot \left(\frac{\dot{\varepsilon}_c}{30 \cdot 10^{-6}} \right)^{1.026 \cdot \alpha} \quad \text{if } \dot{\varepsilon}_c \leq 30 \, \text{s}^{-1} \quad \text{a);}$$

$$f_{cm,dyn} = f_{cm} \cdot \gamma \cdot (\dot{\varepsilon}_c)^{1/3} \quad \text{if } \dot{\varepsilon}_c > 30 \, \text{s}^{-1} \qquad \text{b)}.$$

(81)

In the formulas above, $\dot{\varepsilon}_c$ is the strain rate of concrete, while $\alpha = 1/(5+3 \cdot f_{cm}/4)$ and $\gamma = 10\text{\textasciicircum}(6.156 \cdot \alpha - 0.492)$. Concrete strains ε_{c1} and $\varepsilon_{c,lim}$ are augmented by the following expressions (see also [83]):

$$\varepsilon_{c1,dyn} = \varepsilon_{c1} \cdot \left(\frac{\dot{\varepsilon}_c}{30 \cdot 10^{-6}} \right)^{0.02} ;$$

(82)

$$\varepsilon_{c,lim,dyn} = \varepsilon_{c,lim} \cdot \left(\frac{\dot{\varepsilon}_c}{30 \cdot 10^{-6}} \right)^{0.02} .$$

(83)

As concerns steel ([82],§ 3.4.2), its dynamic strength is calculated as:

$$f_{yk,dyn} = f_{yk} \cdot \left[1 + \frac{6}{f_{yk}} \ln \left(\frac{\dot{\varepsilon}^s}{5 \cdot 10^{-5}} \right) \right] \quad \text{if } \dot{\varepsilon}^s \leq 10 \, \text{s}^{-1} ,$$

(84)

where $\dot{\varepsilon}^s$ is the strain rate of either tensile or compressive reinforcement. If $\dot{\varepsilon}^s > 10 \, \text{s}^{-1}$, the limit value $10 \, \text{s}^{-1}$ is assigned to $\dot{\varepsilon}^s$ in Eq. (87). On the contrary, the module of elasticity E_s is considered constant ([82],§3.4.3; [83],§2).

Chapter 1.2 SDOF Model

This chapter discusses how to assess the dynamic response of the beam by means of a single degree of freedom (SDOF) model. In Fig. 15a, a real beam is depicted (which, as an example, is supposed to be simply supported and subjected to a uniformly-distributed load), while its equivalent SDOF system is sketched in Fig. 15b. It should be noted that damping is disregarded, since successive loading cycles are not considered; in fact, the first peak displacement is the most severe condition, as it is unlikely the structure will collapse after unloading [80].
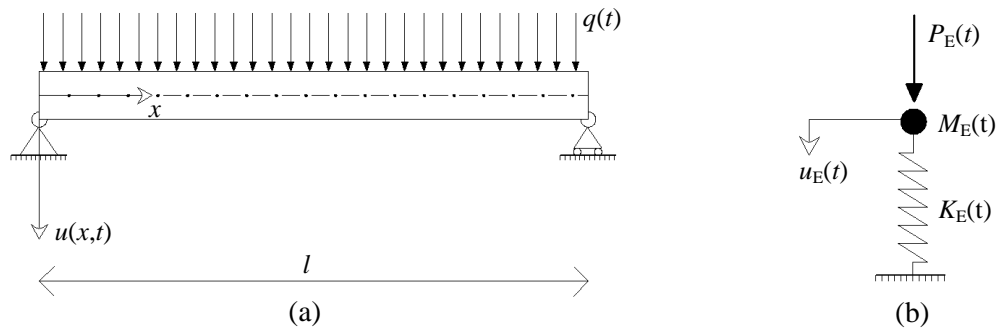
Fig. 15: (a) Real beam; (b) equivalent SDOF model of the real beam.

1.2.1 Load-displacement diagram of the SDOF system

The elastic-plastic behaviour of the SDOF system can be represented by a bilinear load-displacement diagram, as shown in Fig. 16b. The latter can be derived from the bending moment-curvature diagram of the beam (plotted first in Fig. 14a and re-drawn in Fig. 16a), as described in the following:
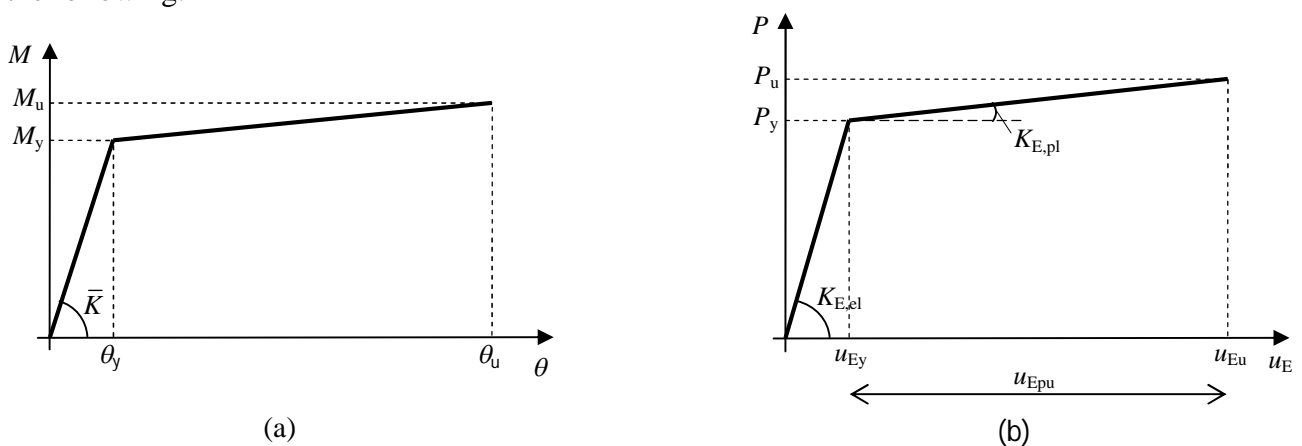
Fig. 16: (a) Bilinear bending moment-curvature diagram of the beam; (b) corresponding bilinear load-displacement diagram of the equivalent SDOF model.

Yield load P_y is easily determined from the yield bending moment M_y by means of equilibrium considerations:

$$M_y = \frac{q_y \cdot l^2}{8} \quad \Rightarrow \quad P_y = q_y \cdot l = \frac{8 \cdot M_y}{l} \tag{85}$$

where q_y is the uniformly-distributed load acting on the beam in the yield state. Yield displacement v_{Ey} can be calculated using the well-known formula provided by the linear elastic theory of beams:

$$u_{Ey} = \frac{5 \cdot q_y \cdot l^4}{384 \cdot \overline{K}} = \frac{5 \cdot P_y \cdot l^3}{384 \cdot \overline{K}} \tag{86}$$

where $\overline{K} = M_y / \theta_y$ is the elastic bending rigidity of the beam (see Fig. 16a). Hence, the elastic stiffness of the SDOF system is given by:

$$K_{E,el} = \frac{P_y}{v_{Ey}} = \frac{384 \cdot \overline{K}}{5 \cdot l^3} \tag{87}$$

The ultimate load P_u can again be obtained from equilibrium conditions:

$$M_u = \frac{q_u \cdot l^2}{8} \quad \Rightarrow \quad P_u = q_u \cdot l = \frac{8 \cdot M_u}{l} \tag{88}$$

where q_u is the uniformly-distributed load on the beam at the ultimate state. Ultimate displacement u_{Eu} is evaluated by assuming that a concentrated plastic hinge is formed at the mid-span section of the beam, as shown in Fig. 17a. Here, φ_p indicates the plastic rotation at any time after generation of the plastic hinge, while u_{Ep} represents the corresponding plastic displacement at the mid-span section. At the ultimate state $\varphi_p = \varphi_{pu}$, hence total plastic displacement, $u_{Ep} = u_{Epu}$ can be calculated as:

$$u_{Epu} = \frac{\varphi_{pu}}{2} \cdot \frac{l}{2} . \tag{89}$$

By introducing plastic hinge length l_p (see Fig. 17b) and by denoting total plastic curvature by θ_p ($\theta_p = \theta_u - \theta_y$), assumed to be constant over l_p, the ultimate displacement u_{Eu} can finally be derived:

$$u_{Eu} = u_{Ey} + u_{Epu} = u_{Ey} + \frac{\varphi_{pu}}{2} \frac{l}{2} = u_{Ey} + \frac{\theta_p \cdot l_p}{2} \frac{l}{2} = u_{Ey} + \frac{1}{4} \cdot \left(\theta_u - \theta_y \right) \cdot l_p \cdot l . \tag{90}$$

Finally, plastic stiffness of the SDOF system is given by:

$$K_{E,pl} = \frac{P_u - P_y}{u_{Eu} - u_{Ey}}.$$

(91)
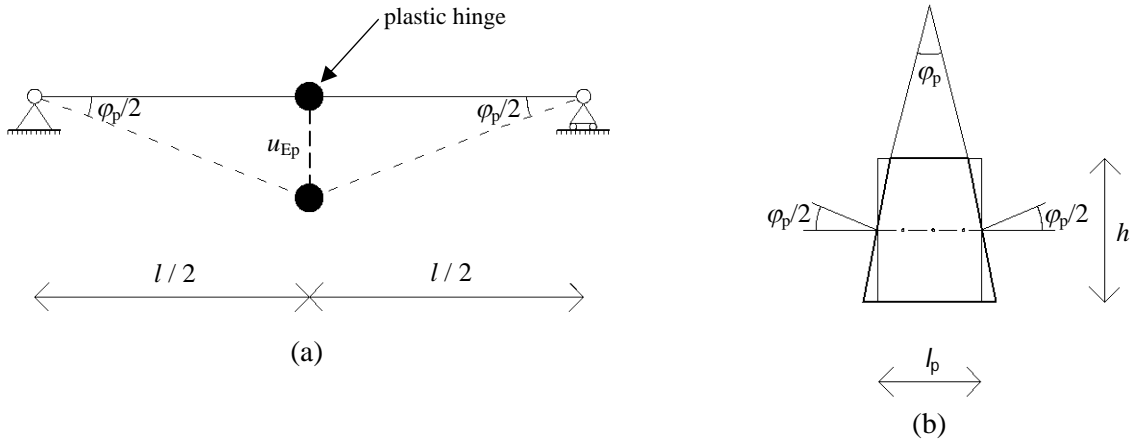
Fig. 17: (a) Plastic deflections of the beam with a concentrated plastic hinge at the mid-span section; (b) schematic representation of the plastic hinge.

The main drawback of this approach is that plastic hinge length l_p cannot be determined *a priori*. Many approximate expressions for l_p are available in the literature. Here, the simple formula provided by Mattock (see [81], [70]) is adopted:

$$l_p = d + 0.05 \cdot l.$$

(92)

For the sake of clarity it is important to point out that the effective height d is defined in the previous Fig. 12 and Fig. 13.

1.2.2 Motion equations of the SDOF system

Motion in the SDOF system under an external dynamic force P_E is described by the following set of ordinary differential equations (refer to Fig. 15b and Fig. 16b):

$$M_{E,el} \frac{d^2 u_E(t)}{dt^2} + K_{E,el}(t) u_E(t) = P_E(t) \quad \text{for } 0 \le u_E \le u_{Ey} \qquad a);$$

(93)

$$M_{E,pl} \frac{d^2 u_E(t)}{dt^2} + K_{E,pl}(t) u_E(t) + \left(K_{E,el}(t) - K_{E,pl}(t)\right) u_{Ey} = P_E(t) \quad \text{for } u_{Ey} < u_E \le u_{Eu} \quad b).$$

It is important to observe that elastic and plastic stiffness ($K_{E,el}$ and $K_{E,pl}$) depends on time t, since it is updated at each step of the calculation due to strain rate effects, as explained in section 3.3.

The equivalent load P_E is simply given by $P_E = q \cdot l$. The elastic and plastic equivalent masses ($M_{E,el}$

and $M_{E,pl}$) are obtained by multiplying the total mass of the beam (M_b) by a "load-mass factor", depending both on the type of regime (either elastic or plastic) and on the beam supports and loads; in particular, for a simply-supported beam with a uniformly distributed load, $M_{E,el} = 0.78 \cdot M_b$ and $M_{E,pl} = 0.66 \cdot M_b$ (see § 1.0.2 and Fig. 4 but also [54],Table 5.1).

1.2.3 Strain-rate effects for the SDOF system

The effects of strain rate are also taken into account for the equivalent SDOF model. Since the dynamic properties of the materials are given in terms of their strain rates (see Eqs. (81)-(84)), it is necessary to relate the SDOF system to the associated (real) beam, from which the strain rates of concrete and steel can be assessed.

Once the equivalent displacement u_E and equivalent velocity $\dot{u}_E = du_E / dt$ are calculated at each time step by solving either Eq. (93) or Eq. (93), the curvature θ_E and the curvature rate $\dot{\theta}_E = d\theta_E / dt$ at the mid-span section of the associated beam can be evaluated. In the elastic regime, θ_E and $\dot{\theta}_E$ are obtained from linear elastic theory; in particular, for a simply-supported beam with a uniformly distributed load, they are given by:

$$\theta_E = \frac{48 \cdot u_E}{5 \cdot l^2} \quad \text{for } 0 \leq u_E \leq u_{Ey} \quad a);$$

$$\dot{\theta}_E = \frac{48 \cdot \dot{u}_E}{5 \cdot l^2} \quad \text{for } 0 \leq u_E \leq u_{Ey} \quad b).$$

(94)

In the plastic regime, on the other hand, it is supposed that a concentrated plastic hinge is generated at the mid-span section of the associated beam, as shown in Fig. 17a. Accordingly, in this case θ_E and $\dot{\theta}_E$ can be evaluated by means of the following expressions:

$$\theta_E = \theta_y + \frac{\varphi_p}{l_p} = \theta_y + 2 \cdot \frac{u_{Ep}}{l/2} \cdot \frac{1}{l_p} = \theta_y + 2 \cdot \frac{u_E - u_{Ey}}{l/2} \cdot \frac{1}{l_p} \quad \text{for } u_{Ey} \leq u_E \leq u_{Eu} \quad a);$$

$$\dot{\theta}_E = 2 \cdot \frac{\dot{u}_E}{l/2} \cdot \frac{1}{l_p} \quad \text{for } u_{Ey} \leq u_E \leq u_{Eu} \quad b).$$

(95)

At each step of the calculation, the value of θ_E (given by either Eq. (94) or Eq. (95)) allows to determine the value of the bending moment M from the bending moment-curvature diagram in Fig. 16a. Then, by imposing rotational equilibrium regarding tensile reinforcement, the neutral axis depth (here denoted as $\bar{x}$) can easily be evaluated. Finally, the strain rates of concrete and of tensile and compressive steel reinforcements are calculated using the following formulas[7]:

$$\dot{\varepsilon}_c = \dot{\theta}_E \cdot \bar{x} \qquad a);$$

$$\dot{\varepsilon}_s = \dot{\theta}_E \cdot (d - \bar{x}) \qquad b);$$

(96)

---

[7] The quantity d and d' have been defined in Fig. 12 and Fig. 13.

$$\dot{\varepsilon}_{ss} = \dot{\theta}_E \cdot (\overline{x} - d') \qquad c) \, .$$

The absolute values of the strain rates given by Eqs. (96) are introduced into Eqs. (81)-(84) to update the properties of the materials.

It is apparent that the procedure described above contains some approximations. This is one of the reasons why the continuous beam model discussed in chapter 1.3 is preferable to the simpler SDOF model presented here.

$$\dot{\varepsilon}_{ss} = \dot{\theta}_E \cdot (\overline{x} - d') \qquad c) \, .$$

Chapter 1.3 Continuous Beam Model

1.3.1 Equation of beam motion under distributed loads

In order to model a reinforced concrete (RC) beam before collapse, Euler-Bernoulli's theory is adopted; it assumes that plane sections remain plane and perpendicular to the beam axis after deformation. An infinitesimal segment of the beam in its deformed configuration is represented in Fig. 18, where u denotes transverse displacements, M is the bending moment, V is the shear force and q is the transverse distributed load. All these quantities are generally functions of both the undeformed axis coordinate x and time t.
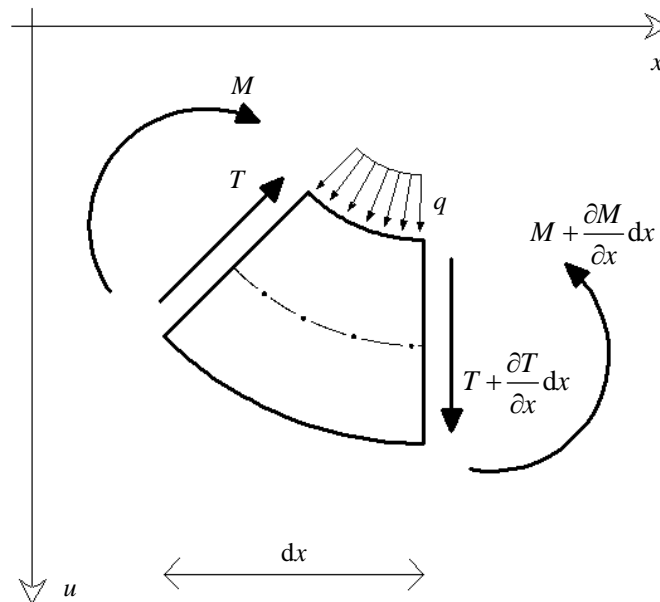
Fig. 18: Internal and external forces acting on an infinitesimal element of the beam.

Equilibrium conditions require that ([84] in § 3.1.1 and §1.0.3.1 of this thesis):

$$\frac{\partial^2 M}{\partial x^2} + q = \mu \frac{\partial^2 u}{\partial t^2} ,$$

(97)

where μ stands for the mass-per-unit length of the beam. Eq. (97) should be satisfied for any constitutive properties of the beam.

The introduction of the sectional model presented in § 1.1 yields an unique relationship between

bending moment and curvature (see Eq. (78)). Furthermore, it allows the use of a single motion equation, without having to split Eq. (97) into one equation for the elastic range and another for the elastic-plastic range, as it is required if a bilinear relationship is considered. Moreover, unloading can be ignored in dynamic problems concerning explosions, since the maximum response of the beam to blast loads is usually found before unloading occurs [80].[8] By substituting Eq. (78) into Eq. (97), the following differential equation of motion in the only unknown u is derived:

$$\bar{K}(t)\operatorname{sech}^2\left(\frac{\bar{K}(t)}{\bar{M}(t)}\frac{\partial^2 u(x,t)}{\partial x^2}\right)\left[-2\frac{\bar{K}(t)}{\bar{M}(t)}\tanh\left(\frac{\bar{K}(t)}{\bar{M}(t)}\frac{\partial^2 u(x,t)}{\partial x^2}\right)\left(\frac{\partial^3 u(x,t)}{\partial x^3}\right)^2+\frac{\partial^4 u(x,t)}{\partial x^4}\right]+\mu\frac{\partial^2 u(x,t)}{\partial t^2}=q(x,t) \quad (98)$$

The solution of Eq. (98) has been obtained by means of a numerical discretization. The finite difference expression of Eq. (98) is presented in the following Eq. (99). All derivatives (both in space (index i) and time (index j)) are computed with a 2nd order approximation. For the sake of clarity k represents the time increment and h the space increment.

$$
\begin{aligned}
&K_{(j)}\operatorname{sech}^2\left(\frac{\bar{K}_{(j)}}{\bar{M}_{(j)}}\frac{u_{(i-1,j)}-2u_{(i,j)}+u_{(i+1,j)}}{h^2}\right)\times\left[\begin{array}{l}-2\frac{\bar{K}_{(j)}}{\bar{M}_{(j)}}\tanh\left(\frac{\bar{K}_{(j)}}{\bar{M}_{(j)}}\frac{u_{(i-1,j)}-2u_{(i,j)}+u_{(i+1,j)}}{h^2}\right)\times\\ \times\left(\frac{-u_{(i-2,j)}+2u_{(i-1,j)}-2u_{(i+1,j)}+u_{(i+2,j)}}{h^3}\right)^2+\\ +\frac{u_{(i-2,j)}-4u_{(i-1,j)}+6u_{(i,j)}-4u_{(i+1,j)}+u_{(i+2,j)}}{h^4}\end{array}\right]+\\[4mm]
&+\mu\frac{u_{(i,j-1)}-2u_{(i,j)}+u_{(i,j+1)}}{k^2}=q(i,j)
\end{aligned}
\qquad (99)
$$

1.3.2 Strain-rate effects for the continuous beam model

It is important to underline that both $\bar{M}$ and $\bar{K}$ are updated at each time step of the calculation, as explained in the next subsection.

1.3.3 Iterative procedure for the integration of the equation of motion

First, the static mechanical characteristics (i.e. the neutral axis depth and the bending moment at yield and ultimate states), determined from Eqs. (72)-(75), are used to calculate the parameters $\bar{K}$ and $\bar{M}$ using Eqs. (79) and (80). Then the initial conditions are imposed and the space and time steps specified.

Next, an iterative procedure is performed, consisting of evaluating the following quantities at each

---

[8] This is why damping has not been included in the formulation.

time step:

1) vertical displacement u, obtained by solving Eq. (98) (for instance, by employing either an explicit or implicit version of the Finite Difference Method, after setting the proper initial and boundary conditions), where $\overline{K}$ and $\overline{M}$ vary at each time step due to strain-rate effects;

2) curvature $\theta = -\partial^2 u/\partial x^2$ and the curvature rate $\dot{\theta} = \partial\theta/\partial t$;

3) bending moment M corresponding to curvature θ from Eq. (78);

4) neutral axis depth from rotational equilibrium around the tensile reinforcement under the applied bending moment M;

5) strains of concrete and steel reinforcements using the linear deformation diagram and curvature value;

6) strain rates of concrete and steel reinforcements;

7) updated dynamic properties of materials by means of Eqs. (81)-(84);

8) updated values of the mechanical characteristics (x_y, M_y, x_u, M_u), by which the values of $\overline{K}$ and $\overline{M}$ are modified.

The loop is closed when the collapse criterion, which has been defined as the attainment of maximum concrete strain (ultimate state), is satisfied.

Chapter 1.4 FE Model

A Finite Element model has been developed by means of commercial software *Midas Gen 2012 (v2.1)*. In particular, the fibre model of this software is used, consisting of dividing the cross-section of the beam into concrete fibres and steel rebars.
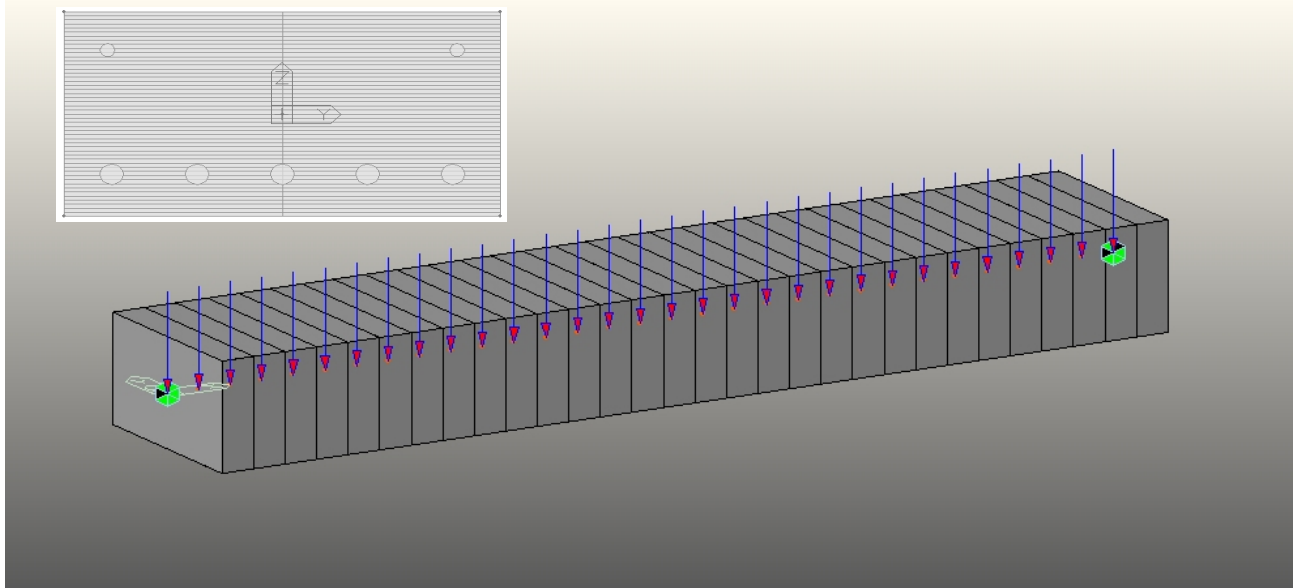
Fig. 19: Picture of the FE model of the beam with loads, boundary conditions and cross section.

The fibre model is developed through the flexibility method: assuming the equilibrium condition, the forces trend in the cross section are expressed in relation to nodal forces by means of specific interpolation functions. The section constitutive law represents the link between strains and stress and a simple application of the principle of virtual forces leads to the matrix of flexibility.

The flexibility method has several advantages in case of nonlinear analysis: the force interpolation matrix is exact with any material constitutive behaviour and so it is not an approximation also in the plastic realm. Furthermore equilibrium considerations can easily produce additional force interpolation functions. In comparison with the well known stiffness method the flexibility method is capable of accurate results even with a single beam element characterised by a sufficient number of integration sections. However the main drawback is that the structural code must impose kinematic and not static boundary condition.

As concerns material models, a trilinear relationship between stress and strain is used for concrete (see Fig. 20a), approximating with great precision the compressive stress-strain diagram shown in Fig. 11a (the tensile strength of concrete is however disregarded, in according to the assumptions of this work); for steel rebars, an elastic–perfectly plastic stress-strain diagram is adopted and showed in Fig. 20b. Variation in compressive zone depth over time is computed by Finite Element software, which thus automatically deals with the transition from compression to tension across the cross-section. In order to take into consideration the effects of strain rate, not accounted for by *Midas Gen 2012 (v2.1)*, the dynamic properties of the material provided by the continuous beam model in the

last step of the calculation (corresponding to the ultimate strain rates reached in the analysis of that model) are introduced into the FE model as constants. If static properties of materials had been used instead, the FE software would have provided an even lower ultimate deflection. The meshes in space and time used in the FE software are identical to those adopted for the continuous beam model and expressed in the next Chapter. Lastly, it should be underlined that, since the software does not include a failure criterion for concrete crushing, the time-history provided by the FE solution is interrupted at the instant in time in which maximum concrete strain obtained from the continuous beam model is reached.
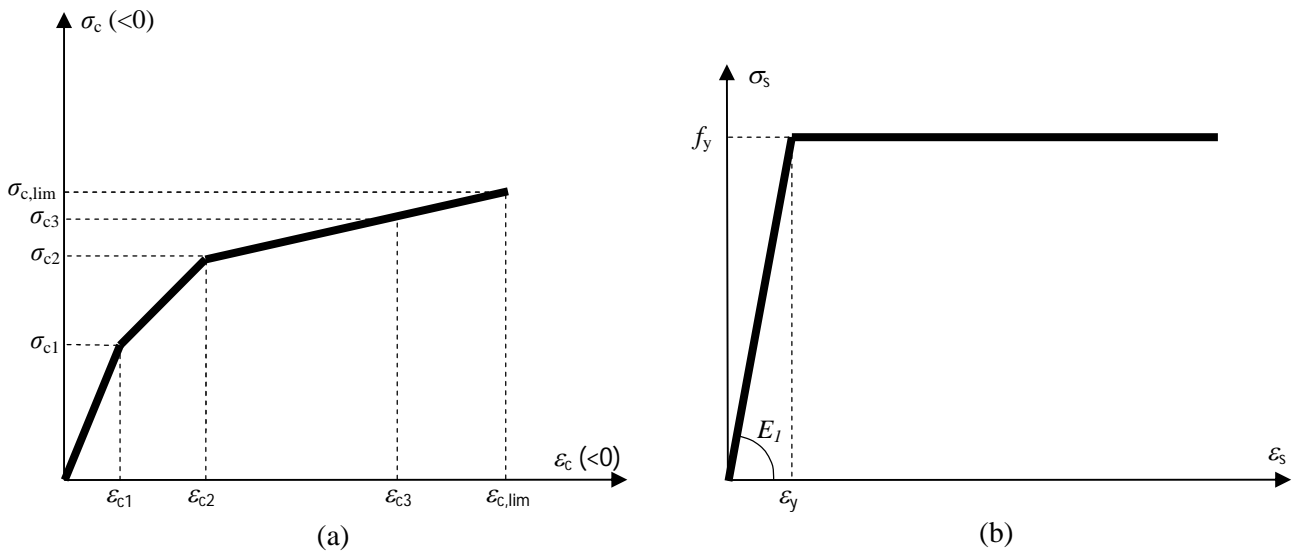
Fig. 20: Fibre model materials constitutive law for concrete (a) and steel (b).

Chapter 1.5 Experimental Procedure

This chapter contains detailed information on the material properties and loads relative to the two beams (tested by Magnusson and Hallgren) analyzed in this thesis, which are labelled B40-D5 and B200/40-D3 in [16].

A sketch of the experimental apparatus set up by Magnusson and Hallgren is shown in Fig. 21. All beams were simply-supported, had a span of 1.5 m and a rectangular cross-section, and were reinforced with both tensile and compressive bars and with stirrups. Other geometric and mechanical characteristics of the beams are summarized in Table 2.
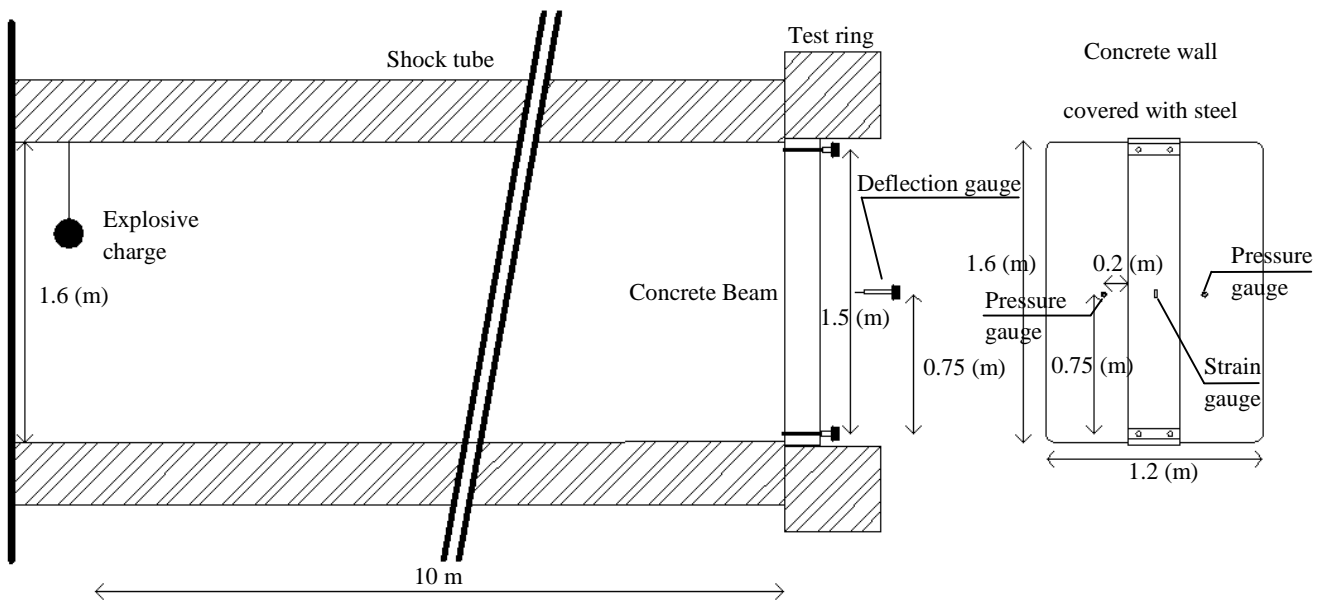
Fig. 21: Experimental apparatus used by Magnusson and Hallgren [16].

The two beams were subjected to the pressures shown in Fig. 22 and Fig. 23. Each figure presents two diagrams, since two pressure gauges were used by Magnusson and Hallgren to register the pressure generated by the explosive charge on each beam. The results in Section 4 were obtained by applying, to each beam, the average pressure between the two curves. The diagrams of Fig. 22 and Fig. 23 have been interrupted at $t = 6$ ms, since for both beams the maximum deflection on failure occurs at a time $t < 6$ ms (see Chapter 1.6). It is important to note that after concrete crushing, both beams continued to move due to an inertia effect, dissipating the amount of energy acquired from the blast load. Experimental gauges recorded these further displacements, but for our structural analysis they are meaningless, as concrete is already crushed at this stage.

Going more in detail, Fig. 22 and Fig. 23 clearly show that there is a strong interaction between fluid (shock-wave) and structure. The properties of the structure have an influence on the pressure and vice versa due to the strain rate effect. Different properties of the concrete beam will produce different pressures, but also different mechanical properties of the structural element will produce different pressure fields. This means that a true analysis should be a time consuming fluid-structure

interaction analysis. Although it is not the main aim of the thesis it is important to underline this concept.

Beam label	B40-D5	B200/40-D3
width of cross-section	0.300 m	0.293 m
depth of cross-section	0.160 m	0.160 m
cover	0.025 m	0.025 m
tensile reinforcement	5 ϕ16 mm	5 ϕ 16 mm
compressive reinforcement	2 ϕ 10 mm	2 ϕ 10 mm
concrete compressive strength [a]	43 MPa	173/54 MPa [b]
maximum concrete strain registered	3.69 ‰	5.03 ‰
steel yield strength	604 MPa	555 MPa
steel elastic modulus	210 GPa	204 GPa
mass per unit length	--- [c]	130 kg/m

[a] Referring to the compressive strength of ϕ 150x300 mm concrete cylinders.

[b] The beam was made of two concrete layers: the first value refers to the concrete in the compressive zone, while the second is relative to the concrete in the tensile zone.

[c] This value has not been provided by the authors, so it has been assumed to be equal to 120 kg/m = 2500 kg/m^3 x 0.3 m x 0.16 m.

Table 2 : Properties of the beams studied in this work (extrapolated from [16]).
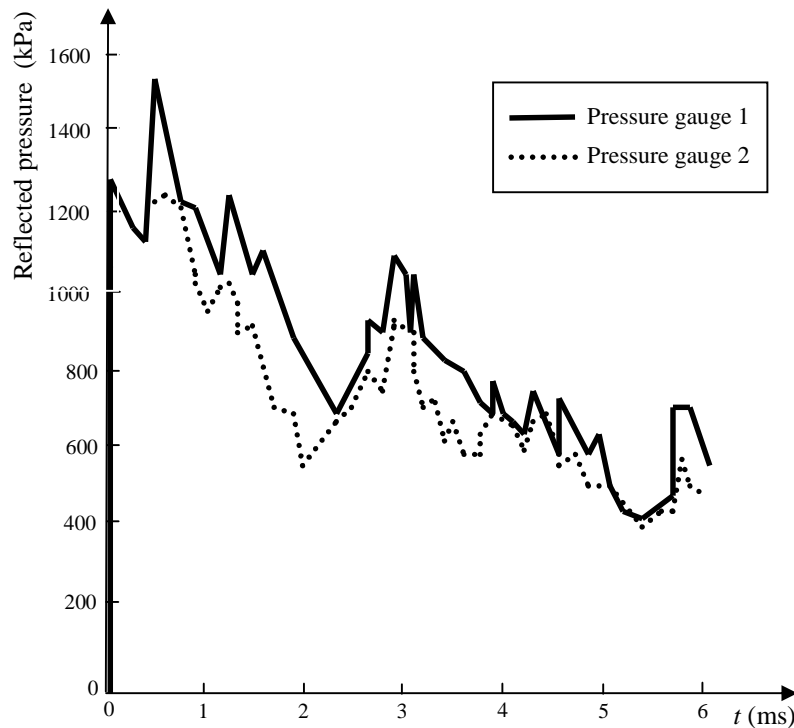
Fig. 22: Recorded pressure for beam B40-D5 (derived from ([16],Fig. A1.6)).
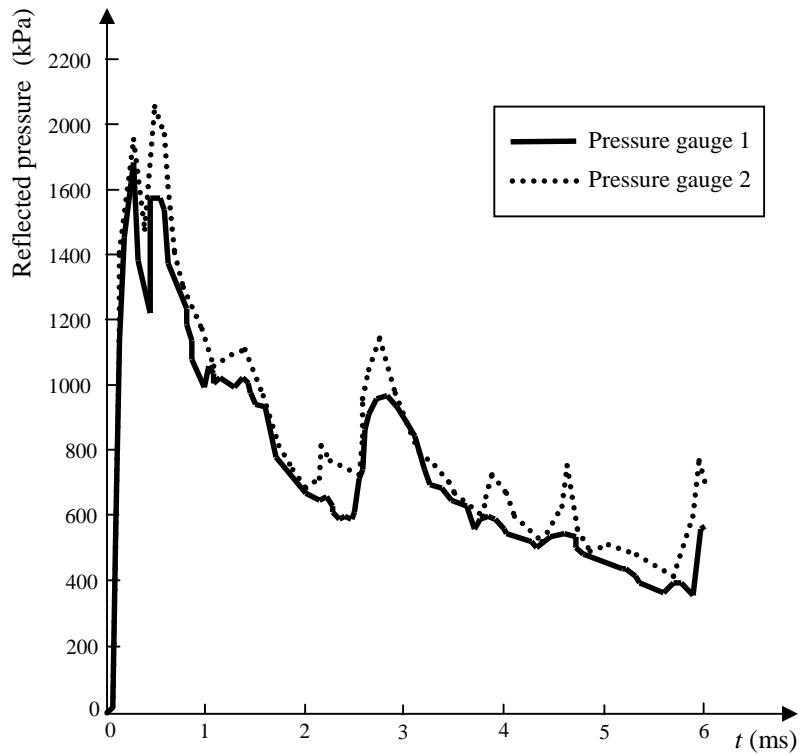
Fig. 23: Recorded pressure for beam B200/40-D3 (derived from ([16],Fig. A1.26)).

Chapter 1.6 Applications and Results

In this chapter, the theoretical models described in Chapters 1.2 – 1.3 – 1.4 are applied to the practical example described in Chapter 1.5. In particular, a simply-supported beam subjected to a uniformly-distributed load generated by an explosion is considered.

Theoretical results are compared with experimental findings obtained by Magnusson and Hallgren [16], who tested several simply-supported RC beams under shock waves produced by air blast. As the authors themselves point out in their paper, the explosive charge was located far enough from the beam to generate a plane wavefront, hence a uniformly-distributed load.

First, the beam labelled B40-D5 is examined. The parameter chosen to compare experimental data with theoretical results is deflection at the mid-span section of the beam, obviously representing maximum deflection, henceforth indicated by u_{max}. The experimental time-history of u_{max} relative to beam B40-D5 is plotted with a solid black line in Fig. 24. The latter has been interrupted when maximum experimental concrete strain is reached, in accordance with the assumption made in this paper that failure occurs when concrete attains maximum strain.

The broken black line in Fig. 24 represents instead the time-history of u_{max} obtained by integrating Eq. (3), derived from the continuous-beam model proposed in this work. This partial differential equation is solved by means of the Finite Difference Method. Since the beam is at rest before the shock wave impinges on it, zero initial conditions are imposed (meaning that displacement and velocities along the beam at the beginning of the calculation are taken as equal to zero), while boundary conditions state that vertical displacement and curvature must vanish at the ends of the beam. At each time step, displacements in the beam are calculated explicitly[9] by using values at previous time steps. Convergence of results is reached by taking a time step of 10^{-6} s and a space step of 0.05 m; in fact, the results produced by the Finite Difference Code after decreasing time and space steps do not show significant variation. Maximum strains in materials according to the continuous beam model are $\varepsilon_{c,lim,dyn} = 0.0044$, $\varepsilon_s = 0.0056$ and $\varepsilon_{ss} = 0.002$. Yielding is reached only in the tensile reinforcement.

The time-history of the maximum deflection predicted by the SDOF model is shown by the dotted black line in Fig. 24. This curve is determined from ordinary differential equations (26), which are integrated in time by again employing the explicit version of the Finite Difference Method and by imposing zero initial conditions (i.e. u_E (t=0) = du_E/dt (t=0) = 0). The chosen time step is identical to that adopted for the continuous-beam model.

Finally, the grey curve in Fig. 24 corresponds to the finite element (FE) solution.

---

[9] It should also be noted that an implicit version of the Finite Difference Method has been used, which requires greater computational effort though providing the same results.
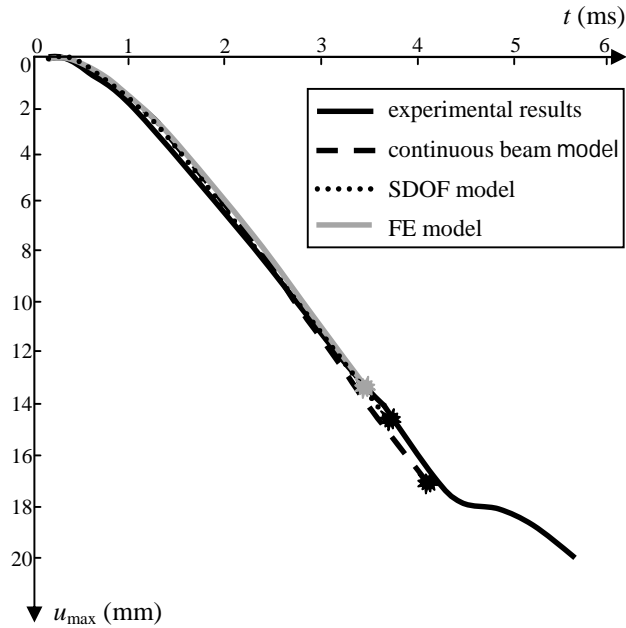
Fig. 24: Time-histories of the maximum deflection of beam B40-D5 (tested in [16]) calculated by means of different theoretical models, and comparison with experimental findings. The spots represent the collapse for each theoretical model.

The experimental time-history of the maximum deflection of another beam analyzed by Magnusson and Hallgren [16], labelled by B200/40-D3, is reported in Fig. 25, along with its theoretical predictions based on the continuous beam model, the SDOF model and the FE model. For this beam, the maximum concrete strain produced by the continuous beam model, used to truncate the deflection time-history derived from the FE model, is $\varepsilon_{c,lim,dyn} = 0.005$. However, the maximum steel strains calculated from the continuous beam model are $\varepsilon_s = 0.028$ and $\varepsilon_{ss} = 0.0026$; in this case as well, yielding is reached only in the tensile reinforcement.

The maximum experimental concrete strains of both beams are reported for comparison purposes in Table 2.
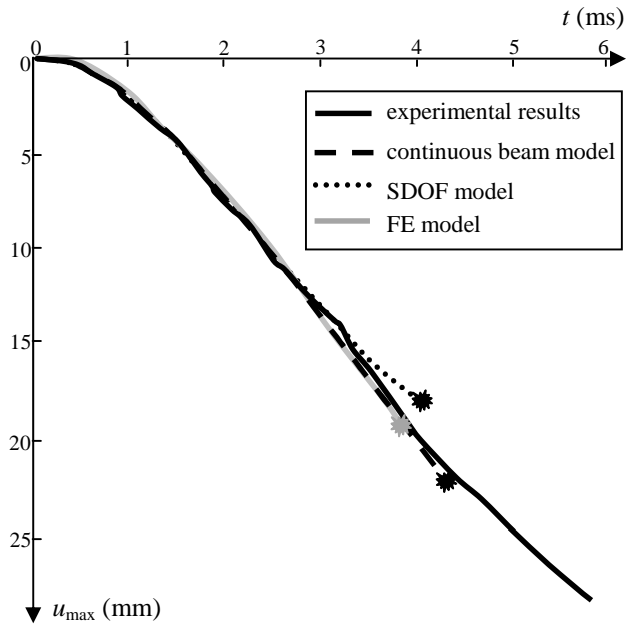
Fig. 25: Comparison between experimental outcomes (provided in [16]) and theoretical results provided by different approaches relative to beam B200/40-D3. The spots represent the collapse for each theoretical model.

Fig. 24 and Fig. 25 show that the continuous beam model presented in this work is the one that best fits with experimental data.[10] In particular, the continuous-beam model gives the most accurate assessment of the maximum deflection of the beam on failure. On the other hand, the FE solution always underestimates the maximum displacement of the beam on collapse, while the prediction of the SDOF model sometimes diverges from the experimental curve (see Fig. 25).

(a)

(b)
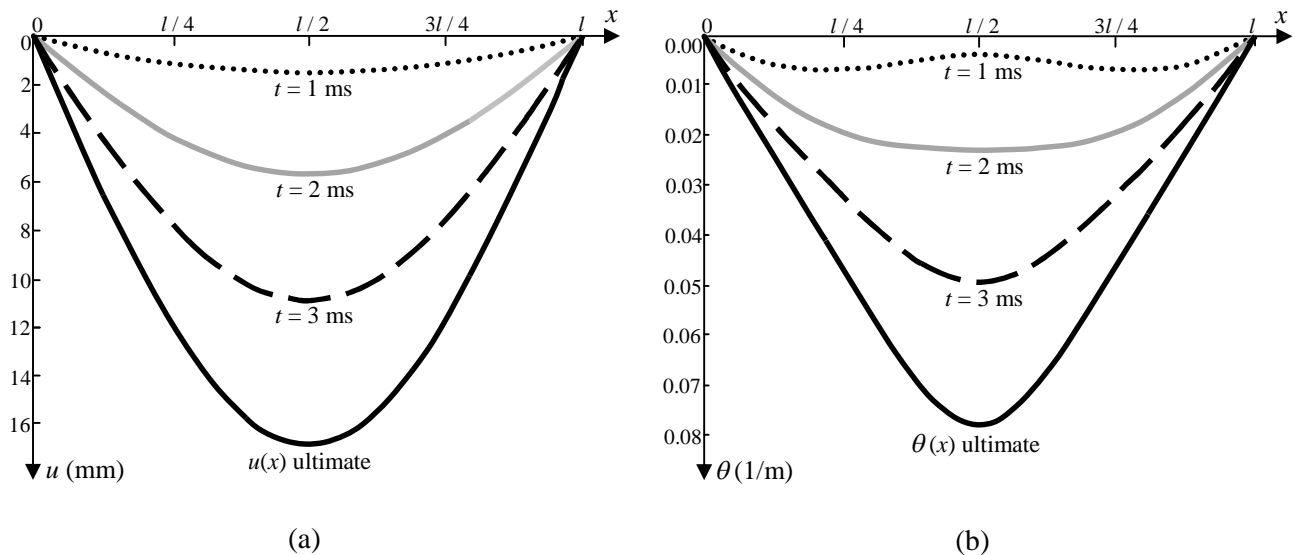
Fig. 26: Vertical displacements (a) and curvatures (b) of beam B40-D5 at different times, predicted by the continuous beam model.

---

[10] This statement is confirmed by the investigation of other beams tested in [16], the outcome of which is not reported here for the sake of brevity.

In addition to fitting well with the actual time-history of maximum beam deflection, the continuous beam model can also provide other useful information, such as displacement and curvature profiles along the beam axis at a particular instant in time, which on the other hand cannot be determined from the SDOF model. For instance, Fig. 26a and Fig. 26b respectively show diagrams of beam vertical displacements and curvatures at different instants in time relative to beam B40-D5. It can be observed from the figures that the vertical displacement and curvature profiles at the initial instants in time (e.g. at $t = 1$ ms) exhibit changes in concavity along the length of the beam, due to inertia effects. As time passes, the deflection and curvature profiles assume the typical shapes they show in the static case. This interesting consideration could not have been derived from the SDOF model, which can provide deflection and curvature values only for the mid-span section of the beam.

SECTION 2:

ENERGY MODELS

Chapter 2.0 Section Introduction

Energy approaches are often simple and require less computational effort. On the other hand, the main characteristic of these methods can also represent their main drawback: referring to a scalar parameter (energy absorbed by the beam or work done by external loads), complex 3-dimensional behaviour can be hazardous. Obviously, such approaches cannot produce all the results obtained by means of a rigorous dynamic approach; on the other hand, energy solutions present a number of significant advantages, as shown in this section.

The first energy solutions refers to Lee and Symonds [22], who used the travelling-static plastic-hinge concept. They calculated an approximation of the final permanent deformation that is the upper boundary for a close-form solution in a beam under transverse load. Approximately ten years later, Greenspon [85] - [89] pointed out that excellent solutions can be obtained without going into the details of propagating hinges. The key is that the residual strain energy stored in a plastically-deformed member could be calculated by assuming a final deformed shape. Greenspon's subsequent assumption was that this strain energy can be equated with the energy flux in an explosive blast wave. Since the seventies, many authors have disagreed with the latter hypothesis: Westine and Baker [90] stated that deformation is dependent on structural orientation relative to the enveloping blast wave, as many experiments have shown. However, Greenspon's energy estimation procedures were correct. Taking into account the case of load regime (impulsive, dynamic, quasi-static: see Section 1, §1.0.1.3), it is possible to determine the Pressure-Impulse Diagram for different structural models.

2.0.1 Pressure-impulse curves

This particular diagram represents the load-impulse combination that will cause a specified level of damage to the structure. Referring to the simple elastic SDOF model (characterized by stiffness equal to k and displacement represented by u) consider the external work done WE by the loads (force P in this case) as defined in the following equation:

$$WE = P \cdot u_{MAX}.$$

(100)

The strain energy acquired by the SDOF *SE* is obtained by Eq. (101).

$$SE = \frac{1}{2} k \cdot u_{MAX}^2 .$$

(101)

Equating *WE* and *SE* yields:

$$\frac{2P}{k \cdot u_{MAX}} = 1 .$$

(102)

Eq. (102) represents a quasi-static asymptote in a non-dimensionalized P-I diagram. If an impulse is applied to the model, the initial velocity can easily be calculated:

$$\dot{u}_0 = \frac{I}{M} ,$$

(103)

where *I* is the blast load pulse and *M* the equivalent SDOF mass. Then the kinetic energy absorbed can be expressed as:

$$KE = \frac{1}{2} \cdot M \cdot \dot{u}_0^2 = \frac{I^2}{2M} .$$

(104)

Equating *KE* and *SE*, after some rearrangement, the expression of the impulsive asymptote can be obtained:

$$1 = \frac{I}{u_{MAX} \sqrt{k \cdot M}} .$$

(105)
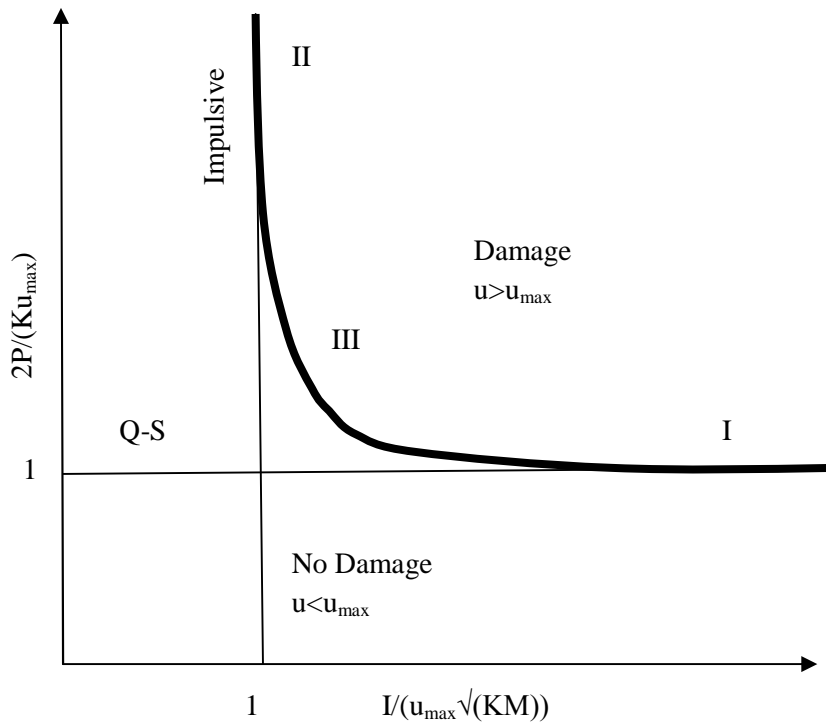
Fig. 27: Non-dimensionalized pressure-impulse diagram for SDOF elastic system (derived from

([6],Fig. 4.6)).

As stated by Mays and Smith [6], the P-I diagram (see, for example, Fig. 27) allows easy verification of the response to a specified load. Once a maximum displacement (corresponding to a damage level) is specified, this graph shows the combination of P and I that will cause failure. Points to the left or below the curves represent combinations of P and I that will not cause collapse. On the contrary, points to the right or above the curve indicate P and I values that will cause failure.

P-I curves can be derived from more-or-less accurate analytical considerations (as previously done) or from experimental evidence.

2.0.1 Rayleigh-Ritz Method
The Rayleigh-Ritz Method of analysis [60] has been used since the early seventies [90], [91], [92] to obtain energy solutions for uncoupled SDOF systems, referring to static deformed shape cases and not displacement time-histories. The description of this method, provided by Mays and Smith [6], appears below:

- First of all, it is necessary to select a mathematical representation of the deformed shape which satisfies all boundary conditions.
- Referring to the deformed shape, curvature and strain are defined.

In the case of impulsive loading, a calculation of the *KE* absorbed by structures is developed. Then strain energy *SE* is equated to the *KE* in order to assess structural response in terms of displacement, strain and stress.

On the other hand, if the load is quasi-static, the external work *WE* is estimated by means of integration of the elementary work over the whole loaded area. Even in this case, the equation between *SE* and *WE* yields the estimation of displacements, strain and stress.

For example, in [90], Westine et al. assumed the following polynomial expression as the deformed shape of a rigid-simple supported beam of span *L* under a uniform load:

$$u = u_0\left(1 - \frac{4x^2}{L^2}\right).$$

(106)

If *b* is the width of the loaded member, ρ the density of the material, *A* the cross-sectional area, *i* the specific impulse and M_y the plastic yield moment, maximum displacement u_0 at midspan in the impulsive realm is expressed by Eq. (107).

$$\frac{u_0}{L}16 = \frac{i^2 b^2 L}{\rho M_y A}.$$

(107)

Westine et al. [90] experimentally demonstrated the validity of their approach, comparing their results with the experimental findings by Florence and Firth [93] (the comparison is shown in Fig. 28). In [93], rectangular cross-section beams are used. The bending moment at yielding state is equal to: $M_y = \sigma_y bh^2/4$.
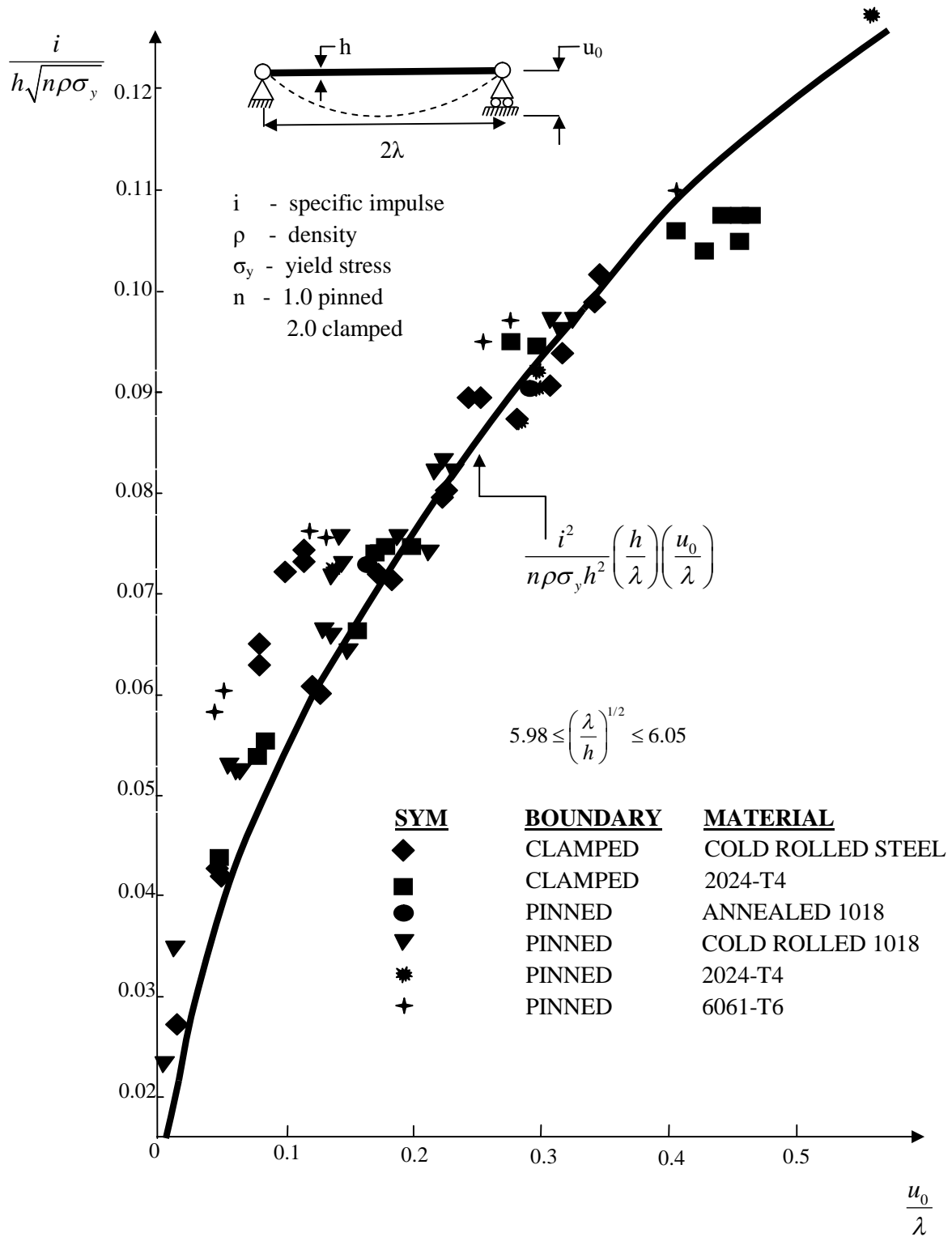
Fig. 28: Comparison between Westine et al. [90] model and Florence and Firth [93] (derived from ([90],Fig. 9)).

In this case, the quasi-static realm asymptote is expressed in Eq. (108), where p is the load pressure.

$$12 = \frac{pbL^2}{M_y}.$$

(108)

This methodology is developed in an original way in Chapter 2.2. The author has considered the Rayleigh Ritz Method as a step-by- step procedure to estimate the displacement of beams described in chapters 1.5-1.6. In addition, strain rate effects and non-linear constitutive relationships are taken into account.

2.0.2 Other approaches
Blast-load structures are stressed at very high frequencies. In this realm, the response of the structural element becomes sensitive to small details (construction technology, material properties, boundary conditions) that cannot be ascertained with sufficient accuracy.

As stated by Bouthier and Bernhard [94], for many diagnostic and design purposes, a simple approximation is often preferred. The first approximate method for built-up structures was Statistical Energy Analysis (SEA), introduced by Lyon [95], [96]. It is a lumped parameter approach (single parameter for each structural subsystem) in which the coupling power between two subsystems is assumed to be proportional to the difference in their modal energies. Furthermore, proportionality constants are related to coupling loss factors, as described by Ju-Bum Han [97]. The main drawback of this approach is that it is not possible to model local behaviour. For this reason, it is necessary to evaluate global characteristics for local phenomena. As a result, there have been several studies to develop methods to estimate the approximate response of structures using a continuous approach. Energy Flow Analysis (EFA), introduced by Belov et al. [98], is an efficient "wave" approach based on an energy equation similar to the heat conduction equation in a steady state. In 1989, Nefske and Sung solved the governing equation by means of FEM and estimated the vibrational response of the Euler-Bernoulli beam. Wohlever and Bernhard [99] improved the application of EFA, developing a rigorous method for approximate energy solutions. Bouthier refined this method and applied it to transversely vibrating plates [100] and membranes [101]. In a recent work [102], Ju-Bum Han et al. developed the energy-flow model for thin plates in contact with mean flow.

Other precise energy solutions have been obtained by Luzzato [103], Lase [104] and Le Bot [105]. In this case, Lagrangian energy and energy density are considered as coupled variables. This methodology can be used at any frequency without approximations, but requires great computational effort.

Chapter 2.1 Energy acquisition by elastic SDOF: a toy problem

In this chapter, in order to go more deeply into the energy approach, the aim is to determine how much energy from the shock wave is dispersed in structural deformation. For the sake of simplicity, this chapter will not consider energy dissipation due to viscosity and plastic deformation and will model a small building by means of a simplified SDOF model. Actually, the focus of this analysis is not the dynamic result, but energy transfers between the blast wave and structures. For this reason, the SDOF model will not consider the strain-rate effect and the plastic field. A simple elastic-linear analysis will be developed to determine how much elastic energy is absorbed by the structure from a qualitative point of view.

<u>2.1.1 Total energy of the shock:</u>
First of all, consider the case of external detonation caused by a 500-kg charge of TNT. In [7], it is assumed that the detonation enthalpy of TNT is $4,6 \cdot 10^6$ J/kg. For this reason, a 500-kg charge of TNT contains an amount of energy equal to $4,6 \cdot 10^6 \cdot 500 = 2300 \cdot 10^6$ J.

Actually, considering that a spherical wave emanates from the charge, not all the energy will hit target structures. When we have a superficial burst, the lower half of the wave will be dispersed in the soil, with some reflection. Therefore, only the upper half is to be considered: in addition, only a portion of this will be in contact with the target, depending on its surface. The other part of the wave does not interact with it (see Fig. 29).
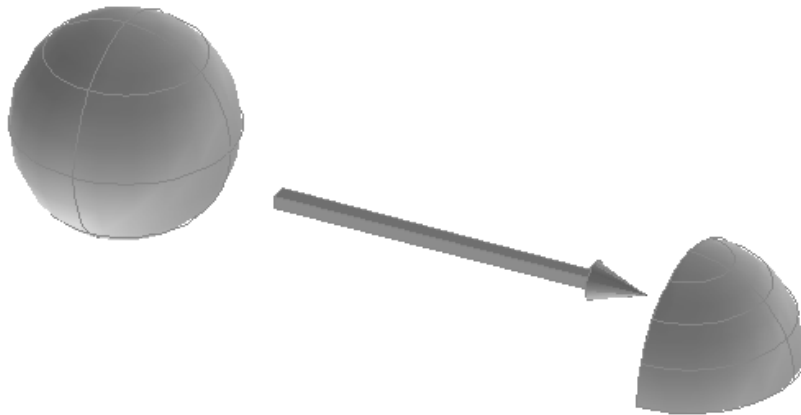
Fig. 29: Only a portion of spherical wave energy is considered.

<u>2.1.2 Energy absorbed by the structure</u>
The basic assumption of this analysis is that in most cases, an impulsive regime must be considered. Kinetic energy from the wave is transmitted to the structure by means of initial conditions, and it can be easily determined by means of Eq. (104).

The main objective of this analysis is to quantify the percentage of shock-wave energy absorbed by the building in the two modalities considered. If E_{RTOT} is the total amount of energy associated with

a certain mass of TNT impinging on the structure, the ratio E_{ASB}/E_{RTOT} is to be determined, where $E_{ASB}=KE$ is the energy absorbed by the building, represented as an equivalent SDOF.

2.1.3 First case: Building 1.

In this calculation, 500 kg of TNT are considered. The total amount of energy due to this charge is $2300 \cdot 10^6$J, but only part of this energy really impinges on the structure. For each case, it is necessary to calculate the ratio between the surface of the target and the total area of the sphere. This ratio is assumed to be equal to the ratio between the part of energy interacting with the building E_{RTOT} and real total energy E_{TOT}. Several scenarios are analyzed using different buildings:

The first one is the following one-storey frame system (Fig. 30). It is a R.C. structure: 6 columns with a cross-section 300x300 mm.
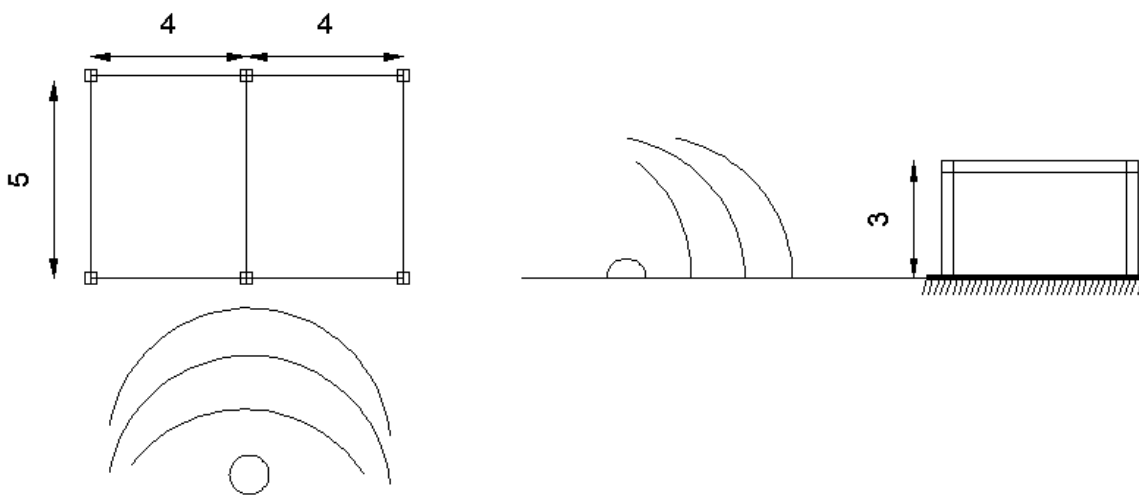
Fig. 30: Building 1: measurements are in m.

The characteristics of the equivalent SDOF reported in Table 3 were found by the calculation.

k	N/m [11]=	45.000.000,00
M	kg=	28.440,00
$\omega = \sqrt{\dfrac{k}{M}}$	1/sec=	39,78

Table 3 : Properties of the equivalent SDOF model for building 1.

Referring to [6],[7], [92] and considering various stand-off distances z (see Eq.(1)) , the following quantities can be determined:

---

[11] This stiffness is due to the fact that a column (with the base fixed in the ground and the head rigidly connected to the beam) in a shear-type frame has a characteristic stiffness of 12 EJ/h^3, but in this case there are 6 columns, so that value is multiplied by 6.

a) Stand-off distance= 5 m
   z=0,631 m/kg$^{1/3}$

E_{ASB}=	1.76· 10^{8}J
Pr =	2.48· 10^7 N/m^2
t_p =	0,000161 sec
I =	1.34· 10^4 Pa·sec
$\omega\ tp$ =	0,0064
M_{TNT} =	500,00 kg
A =	24,00 m^2

Table 4 : Characteristics of load scenario a).

Considering the characteristics of the load scenario expressed in Table 4 and Eq. (110), the ratio between the incident energy and energy acquired from the SDOF is $E_{ASB}/\ E_{RTOT}$ =1.04% .

$KE=E_{ASB}=(IA)^2/2M$	1.82· 10^6 J
E_{RTOT}=	1.76· 10^8 J
E_{ASB}/E_{RTOT}	1.04 %

Table 5 : Energy values for scenario a).

b) Stand-off distance= 10 m
   z=1,263 m/kg$^{1/3}$

Pr =	4.25· 10^6 N/m^2
t_p =	0,001675 sec
I =	5.17· 10^3 Pa·sec
$\omega\ tp$ =	0,0666
M_{TNT} =	500,00 kg
A =	24,00 m^2

Table 6 : Characteristics of load scenario b).

$KE=E_{ASB}=(IA)^2/2M$	0.27· 10^6 J
E_{RTOT}=	4.39· 10^7 J
E_{ASB}/E_{RTOT}	0.61 %

Table 7 : Energy values for scenario b).

c) Stand-off distance= 15 m
   z=1,894 m/kg$^{1/3}$

Pr =	1.25· 10^6 N/m^2
t_p =	0,005074 sec
I =	3.10· 10^3 Pa·sec
$\omega\ tp$ =	0,2018
$MTNT$ =	500,00 kg
A =	24,00 m^2

Table 8 : Characteristics of load scenario c).

$KE=E_{ASB}=(IA)^2/2M$	$9.7 \cdot 10^4$ J
$E_{RTOT}=$	$1.95 \cdot 10^7$ J
E_{ASB}/E_{RTOT}	0.50 %

Table 9 : Energy values for scenario c).

d) Stand-off distance= 20 m
z=2,525 m/kg$^{1/3}$

Pr =	$5.35 \cdot 10^5$ N/m^2
t_p =	0,006710 sec
I =	$2.19 \cdot 10^3$ Pa·sec
$\omega\, tp$ =	0,2669
$MTNT$ =	500,00 kg
A =	24,00 m^2

Table 10 : Characteristics of load scenario d).

$KE=E_{ASB}=(IA)^2/2M$	$4.8 \cdot 10^4$ J
$E_{RTOT}=$	$1.10 \cdot 10^7$ J
E_{ASB}/E_{RTOT}	0.44 %

Table 11 : Energy values for scenario d).

Thus, it is possible to graphically represent the percentage E_{ASB}/E_{RTOT} depending on the scaled distance z (see Fig. 31). Observe how this ratio is very low, even if we consider a very short stand-off distance:
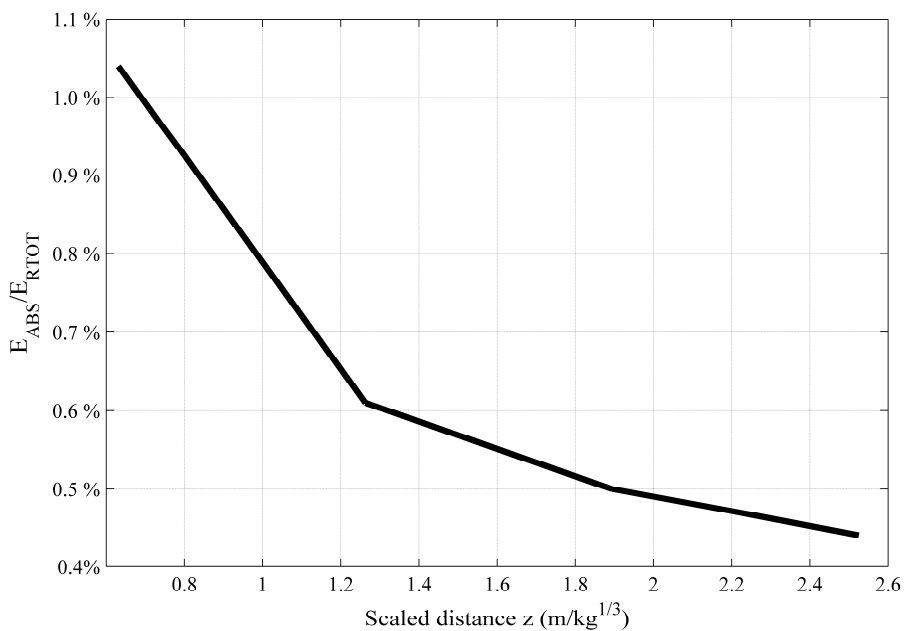
Fig. 31: Incidence E_{ABS}/E_{TOT} depending on z for 500 kg of TNT considering building 1.

2.1.3 Second case: Building 2.

Building n.2 is the two-storey frame system shown in Fig. 32. It is a R.C. structure with a column cross-section of 300x300 mm.
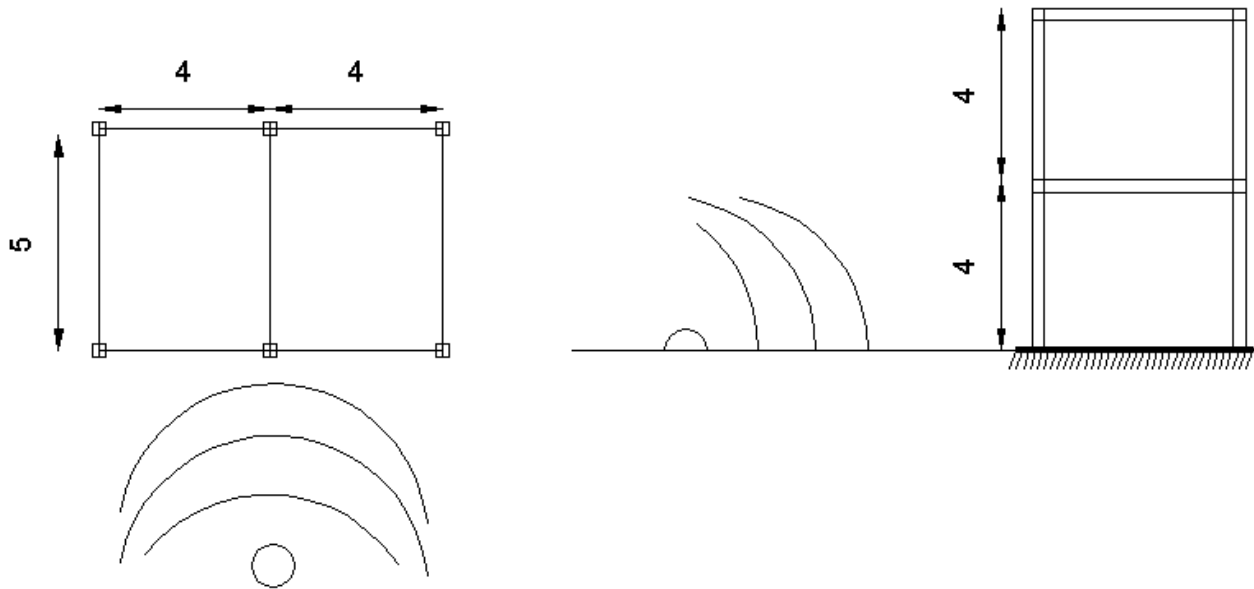
Fig. 32: Building 2, measurements are in m.

In this second case, we have a structure with a larger exposed surface and less stiffness than building 1.

Actually, in order to calculate stiffness of the equivalent SDOF, a simplified method is used. The assumption of an impulsive load regime was already considered, and a F.E. model was constructed. To identify the first modal shape an upper horizontal load of 1000 N (see Fig. 33) is considered. Then, the displacement in the node where the force is applied is calculated. From the ratio force/displacement, equivalent stiffness is determined. Obviously, the use of an equivalent SDOF for this building is a rough approximation, as equivalent stiffness is calculated very simply.
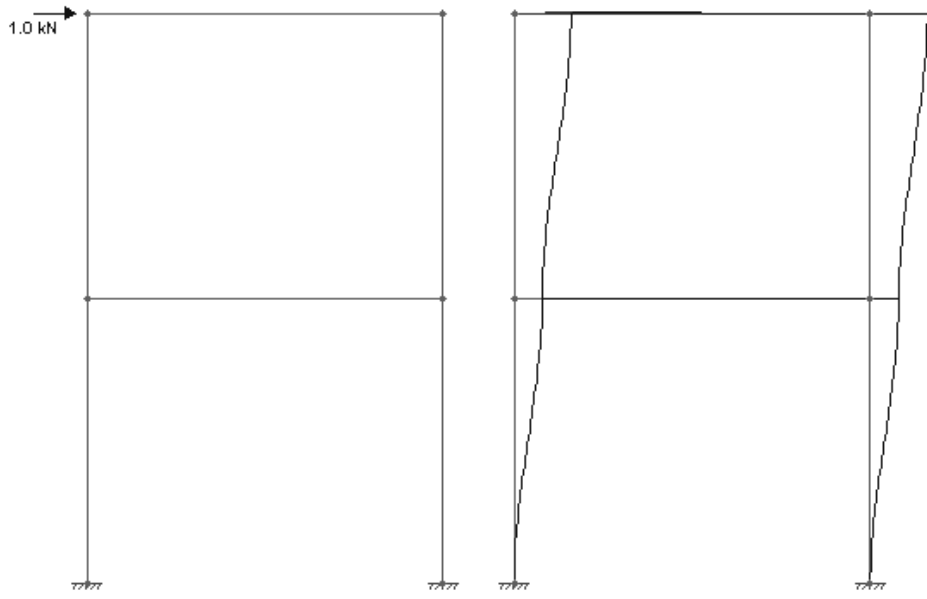
Fig. 33: Calculation of equivalent stiffness for building 2.

From the calculation, the characteristics of the equivalent SDOF are:

k	N/m =	9.325.458,50
M	kg=	59.480,00
$\omega = \sqrt{\dfrac{k}{M}}$	1/sec=	12,52

Table 12 : Properties of the equivalent SDOF model for building 2.

Following the same procedure developed for building 1(considering an incidence area of 48 m^2, and the characteristics reported in Table 12), to avoid encumbering the discussion, in Fig. 34 is depicted the percentage trend of E_{ABS}/E_{RTOT} for this case.
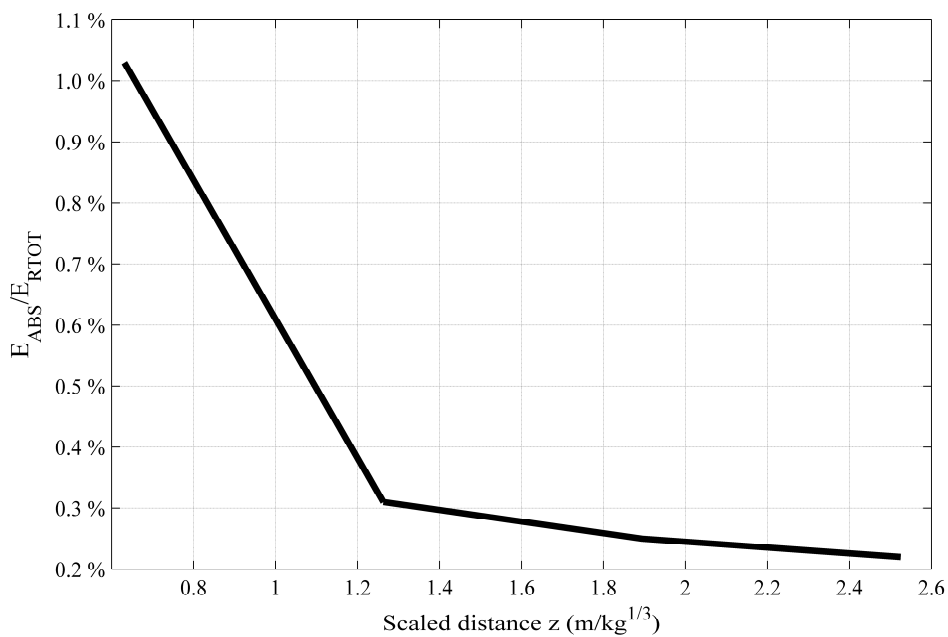
Fig. 34: Incidence % E_{ABS}/E_{TOT} depending on z for 500 kg of TNT for building 2.

2.1.4 Discussion

The aim of this analysis is to quantify the amount of energy absorbed by the building from the shock wave. Given that the scenario assumes fundamental importance and that the study of many other cases is necessary for a complete analysis, results show a clear trend. The largest amount of energy absorbed by buildings occurred with 500 kg of TNT placed 5 m away from building 1 with a ratio $E_{ASB}/E_{RTOT} = 1,04$ %. It is important to point out that this percentage can increase taking into account that the real angle of incidence can be zero only for a very small part of the façade. Everywhere else, there is a component of the velocity of the blast-wave front parallel to the building façade, and even less energy is transferred to the building. These results can be affected by other inaccuracies in calculation and modelling, as the idea of representing two-storey buildings (see Building 2) with a SDOF is clearly a rough approximation. Actually, even with more refined modelling, the result trend does not change. Difficulty in the exchange of energy between wave and building is caused by different characteristic loading and structural response times. Detonations have a very short development time (order of milliseconds); they are typically a real pulse for the structure. Therefore, the energy transmitted by the wave "travels" through the structure at too high a speed and cannot be absorbed by the building.

It is clear that, after the blast wave has interacted with the structure, it has not by any means lost all its energy (i.e. the blast wave does not "disappear") but will reflect from the building, diffract around it and also re-form behind it. Deformation of the building removes energy, but not, by any means, all of it. The blast wave will continue to propagate (having lost some energy in deforming the structure) away from the detonation. Though the flow field of the portion of the blast wave front that has actually interacted with the building will be more complex than that which has not interacted, in general the wave front will continue to expand.

Finally, by splitting the structure up into much smaller elements, it is possible to assess its response more accurately. The SDOF approach was really developed for discrete structural components rather than whole buildings. In addition, SDOF deals with small masses that can easily be carried away by the wave, so they are able to deform, acquiring more elastic potential energy and kinetic energy. There are numerous design procedures and papers (i.e. [106]) in which particular components of the structural system are sacrificed as points in which deformations are concentrated, as if they were structural fuses. In this way, some parts of the structure are independent of each other and in case of failure, global collapse is prevented.

In conclusion, this chapter shows that a very small part of the total energy of the explosive charge interacts with the structure. On the other hand, this small amount of energy can be of paramount relevance in assessing whether or not a structure can resist blast action. Actually, even if only an infinitesimal percentage of explosion energy is absorbed by the structure, it can produce local failure or global failure. The next chapter reports an energy approach for calculating the displacement and deformation of beams under blast load, based completely on the principle of energy conservation, without using motion equations.

Chapter 2.2 Balance of Energy approach for continuous beams

The conservation of energy requires that Eq. (109) must be fulfilled for each previous dynamic model:

$$WE(t) = KE(t) + SE(t) .$$

(109)

In equation (109):

- *WE(t)* represents the external work done by loads (blast wave in our analysis) at time *t*.
- *KE(t)* represents the kinetic energy acquired by the beam at time *t*.
- *SE(t)* represents the strain energy (both plastic and elastic) absorbed by the beam at time *t*.

Referring to the case of simple supported beams under the uniformly space-distributed blast load already discussed in Section 1 (for the meaning of each symbol, see §1.1-1.3.1-1.6), it is possible to specify Eq. (109) in Eq.(110) with positional correspondence between each term:

$$\int_0^l \int_0^t q(t) \cdot \frac{\partial u(x,t)}{\partial t} \, dt \, dx = \int_0^l \frac{1}{2}\mu \cdot \left(\frac{\partial u(x,t)}{\partial t}\right)^2 dx + \int_0^l \int_0^{\theta(x,t)} \overline{M} \tanh\left(\frac{\overline{K}}{\overline{M}}\theta(x,t)\right) d\theta \, dx .$$

(110)

Actually, this approach contains some approximations: sectional behaviour is expressed by the Bending Moment-Curvature Relationship previously presented (see Eq. (78)), and rotational inertia is not considered. The second integral on the right side of Eq. (110) can be developed and yields Eq. (111).

$$\int_0^l \int_0^t q(t) \cdot \frac{\partial u(x,t)}{\partial t} \, dt \, dx = \int_0^l \frac{1}{2}\mu \cdot \left(\frac{\partial u(x,t)}{\partial t}\right)^2 dx + \int_0^l \frac{\overline{M}^2}{\overline{K}} \ln\left(\cosh\left(-\frac{\overline{K}}{\overline{M}}\frac{\partial u^2(x,t)}{\partial x^2}\right)\right) dx .$$

(111)

The continuous beam dynamic model of §1.3 has been considered a benchmark for this calculation. In other words, both members of Eq (111) have been numerically calculated referring to beams labelled B40-D5 and B200/40-D3. Time and space steps are the same as in the dynamic calculation (respectively $k=10^{-6}$ sec, $h=0.05$ m), as finite difference expressions are expressed in Eqs. (112)-(114):

$$\int_0^l \int_0^t q(t) \cdot \frac{\partial u(x,t)}{\partial t} \, dt \, dx \cong \sum_{i=1}^{n+1} \sum_{m=1}^j q_{(m)} \cdot \frac{u_{(i,m+1)} - u_{(i,m-1)}}{2} \cdot h ,$$

(112)

$$\int_0^l \frac{1}{2}\mu \cdot \left(\frac{\partial u(x,t)}{\partial t}\right)^2 dx \cong \sum_{i=1}^{n+1} \frac{1}{2}\mu \left(\frac{u_{(i,m+1)} - u_{(i,m-1)}}{2k}\right)^2 \cdot h ,$$

(113)

$$\int_0^l \frac{\overline{M}^2}{\overline{K}} \ln\left(\cosh\left(-\frac{\overline{K}}{\overline{M}}\frac{\partial u^2(x,t)}{\partial x^2}\right)\right) dx \cong \sum_{i=1}^{n+1} \frac{\overline{M}^2}{\overline{K}} \ln\left(\cosh\left(-\frac{\overline{K}}{\overline{M}}\frac{u_{(j,i-1)} - 2u_{(j,i)} + u_{(j,i+1)}}{h^2}\right)\right) \cdot h .$$

(114)
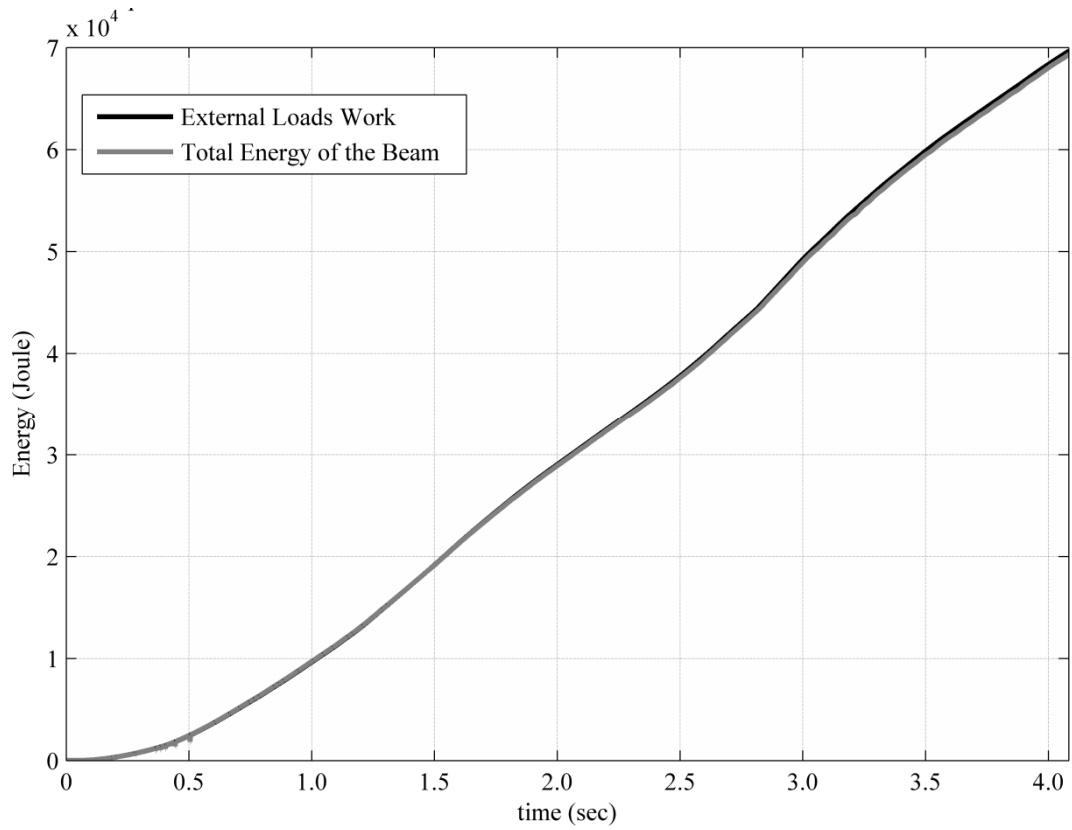
Fig. 35: Comparison between external work of loads and total energy of beam B40-D5.
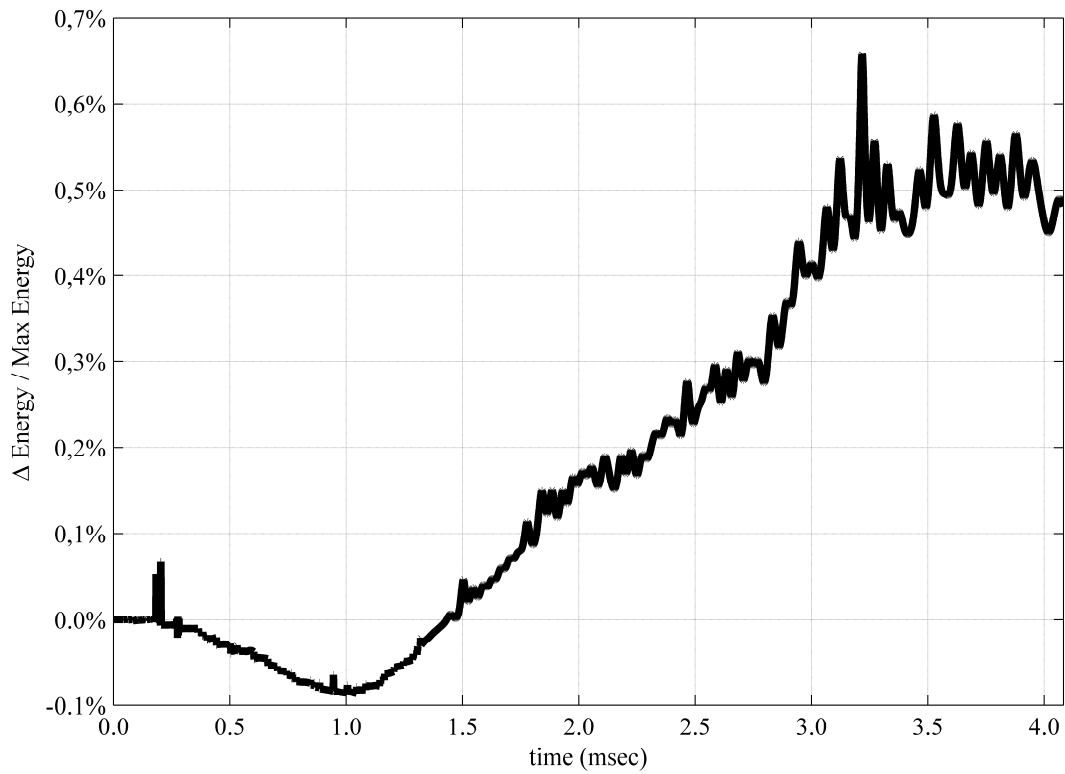
Fig. 36: Normalised ΔEnergy of beam B40-D5.

As concerns B40-D5, Fig. 35 shows the comparison between work done by the external load (equal to the left side of Eq (111) – black line) and the sum of the kinetic energy and strain energy of the beam (equal to the right side of Eq (111) – gray line). As is easy to see, the two lines are identical, even if there are some numerical approximations. In order to better estimate these approximations, the difference between the two curves is defined and normalised in Eq. (115) and shown in Fig. 36. Note that the highest value is below 0.7%.

$$\Delta Energy(t) = \frac{\int_0^l \int_0^t q(t) \cdot \frac{\partial u(x,t)}{\partial t} dt\, dx - \int_0^l \frac{1}{2}\mu \cdot \left(\frac{\partial u(x,t)}{\partial t}\right)^2 dx + \int_0^l \frac{\overline{M}^2}{\overline{K}} \ln\left(\cosh\left(-\frac{\overline{K}}{\overline{M}}\frac{\partial u^2(x,t)}{\partial x^2}\right)\right) dx}{MAX\left\{WE(t), SE(t) + KE(t)\right\}}. \qquad (115)$$
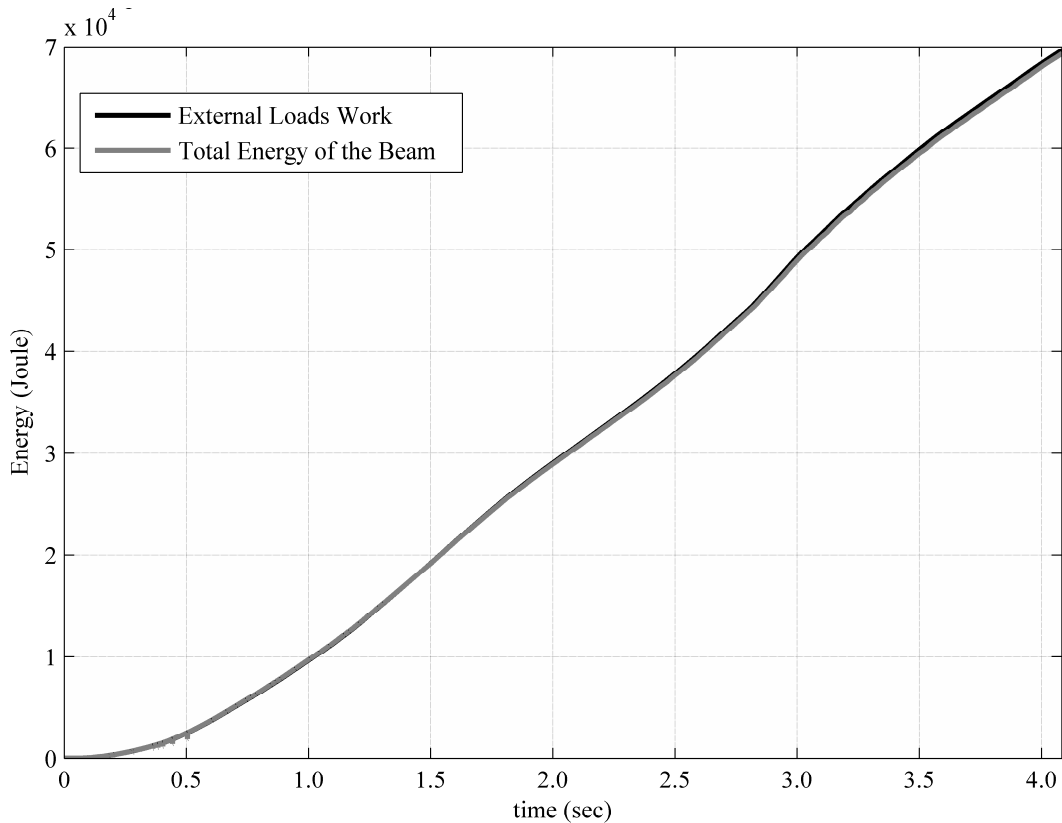
Fig. 37: Comparison between external work of the loads and total energy of beam B200/40-D3.

The same calculations are developed for beam B200/40-D3 and the results shown in Fig. 37 and Fig. 38. Referring to the value of $\Delta Energy(t)$ (defined in Eq (115)), the maximum value is below 0.3%.

These results suggest that Eq. (111) can be a powerful tool: indeed, it can be exploited to determine the displacement of the beam in a step-by-step approach.
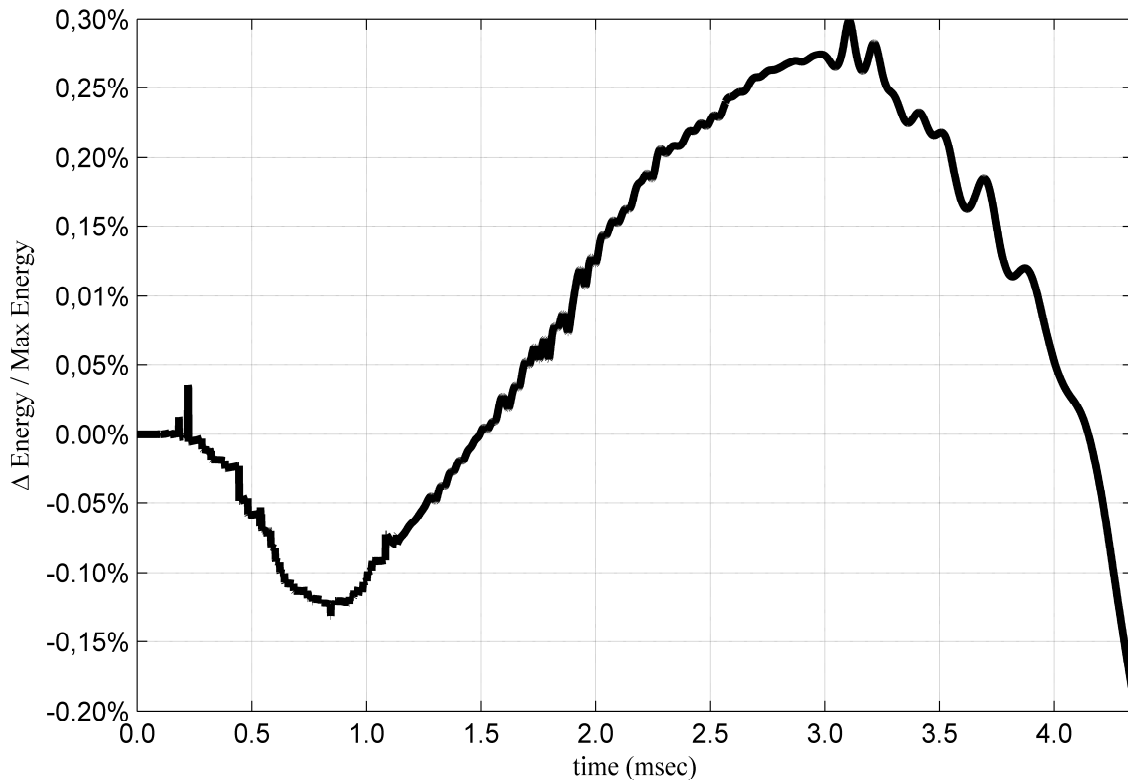
Fig. 38: Normalised Δenergy of beam B200/40-D3.

2.2.1 Calculation of displacement by means of balance-of-energy

The general deformed shape of a simple supported beam under uniform load can be expressed as a sum of odd[12] sinusoidal modes (116) (see [92]). In an early work, Cox et al. demonstrate that*".. the difference between a one mode (the first) and a three mode approximation is less than 3%..".*

$$u(x) = u_0 \sum_{i=1,3,5,..}^{\infty} A_i \sin \frac{i\pi x}{l} . \qquad (116)$$

In addition, consider the results from the dynamic model in §1.6 (i.e. Fig. 26): after 1 *msec,* the deformed shape of the beam seems to be a "pure" sinusoidal curve. For this reason, the simplifying assumption can be expressed by Eq. (117).

$$u(x,t) = u_0(t) \cdot \sin \frac{\pi x}{l} . \qquad (117)$$

After this assumption, it is easy to calculate the relationship between curvature and displacement:

$$\theta(x,t) = -\frac{\partial^2 u(x,t)}{\partial x^2} = \left(\frac{\pi}{l}\right)^2 u_0(t) \cdot \sin \frac{\pi x}{l} . \qquad (118)$$

The introduction of Eq. (118) into Eq.(111) yields:

---

[12] Even modes are not significant due to the symmetry of the structure and of the load condition.

$$\int_0^l \int_0^t q(t) \cdot \frac{\partial u_0(t)}{\partial t} \cdot \sin\frac{\pi x}{l} \, dt \, dx = \int_0^l \frac{1}{2}\mu \cdot \left(\frac{\partial u_0(t)}{\partial t} \cdot \sin\frac{\pi x}{l}\right)^2 dx + \int_0^l \frac{\overline{M}^2}{\overline{K}} \ln\left(\cosh\left(\frac{\overline{K}}{\overline{M}} \cdot \left(\frac{\pi}{l}\right)^2 u_0(t) \cdot \sin\frac{\pi x}{l}\right)\right) dx . \quad (119)$$

Furthermore, the numerical approximation of each term in Eq.(119) is represented below:

$$\int_0^l \sum_{m=1}^{j} q_{(m)} \cdot \frac{u_{0(m+1)} - u_{0(m-1)}}{2} \sin\left(\frac{\pi x}{l}\right) dx = \left(\frac{2l}{\pi}\right) \cdot \sum_{m=1}^{j} q_{(m)} \cdot \frac{u_{0(m+1)} - u_{0(m-1)}}{2} , \quad (120)$$

$$\int_0^l \frac{\mu}{2k^2} \cdot \left(\frac{u_{0(m+1)} - u_{0(m-1)}}{2} \sin\left(\frac{\pi x}{l}\right)\right)^2 dx = \left(\frac{l}{2}\right) \cdot \frac{\mu}{2k^2} \cdot \left(\frac{u_{0(m+1)} - u_{0(m-1)}}{2}\right)^2 , \quad (121)$$

$$\int_0^l \frac{\overline{M}^2}{\overline{K}} \ln\left(\cosh\left(\left(\frac{\pi}{l}\right)^2 u_{0(j)} \sin\left(\frac{\pi x}{l}\right)\frac{\overline{K}}{\overline{M}}\right)\right) dx = \sum_{i=1}^{n+1} \frac{\overline{M}^2}{\overline{K}} \ln\left(\cosh\left(\left(\frac{\pi}{l}\right)^2 u_{0(j)} \sin\left(\frac{\pi x_i}{l}\right)\frac{\overline{K}}{\overline{M}}\right)\right) h . \quad (122)$$

Considering Eqs.(119)-(122), it is possible to set up a procedure to determine displacement u_0 for each time step:

- Introduce the numerical approximation Eqs.(120)-(122) into Eq.40 and write it at j-th instant in time:

$$u_0^2{}_{(j+1)}\left\{\frac{\mu l}{16k^2}\right\} + u_{0(j+1)}\left\{-\frac{\mu l}{8k^2}u_{0(j-1)} - q_{(j)}\frac{l}{\pi}\right\} + \left\{\begin{array}{l}\frac{\mu l}{16k^2}u_0^2{}_{(j-1)} + \sum_{i=1}^{n+1}\frac{\overline{M}^2}{\overline{K}}\ln\left(\cosh\left(\left(\frac{\pi}{l}\right)^2 u_{0(j)}\sin\left(\frac{\pi x_i}{l}\right)\frac{\overline{K}}{\overline{M}}\right)\right)h + \\ -\left(\frac{2l}{\pi}\right) \cdot \sum_{m=1}^{j-1}q_{(m)} \cdot \frac{u_{0(m+1)} - u_{0(m-1)}}{2} + q_{(j)}\frac{u_{0(j-1)}}{2}\left(\frac{l}{\pi}\right)\end{array}\right\} . \quad (123)$$

- Determine the unique unknown $u_{0(j+1)}$ and calculate the sinusoidal distribution of displacement and, consequently, curvature at midspan.

- Then, considering previous curvature, calculate the curvature rate $\dot{\theta} = \partial\theta/\partial t$.

- Determine the bending moment *M*, corresponding to curvature θ from Eq. (78).

- Calculate the neutral axis depth from rotational equilibrium around the tensile reinforcement under the applied bending moment *M*.

- Determine strain on concrete and steel reinforcements by using the linear deformation diagram and curvature value.

- Determine the strain rates of concrete and steel reinforcements;

- Calculate the updated dynamic properties of materials by means of Eqs. (81)-(84);

- Determine the updated values of the mechanical characteristics (x_y, M_y, x_u, M_u), by which the

values of $\bar{K}$ and $\bar{M}$ are modified.

The loop is closed, as explained in Section 1, when maximum concrete strain (ultimate state), is obtained.

Chapter 2.3 Applications

As in Section 1, the theoretical Energy Model is applied to a practical example: a simply- supported beam subjected to a uniformly-distributed load generated by an explosion is considered.

Theoretical results are compared with experimental findings obtained by Magnusson and Hallgren [16]. See Chapter 1.6 for all details regarding the beams examined.

Fig. 39 depicts the time-histories of the midspan displacement of the beam labelled B40-D5. The grey line represents the result obtained by means of the energetic theoretical model, while the black one corresponds to the experimental findings already presented in Chapter 1.3.
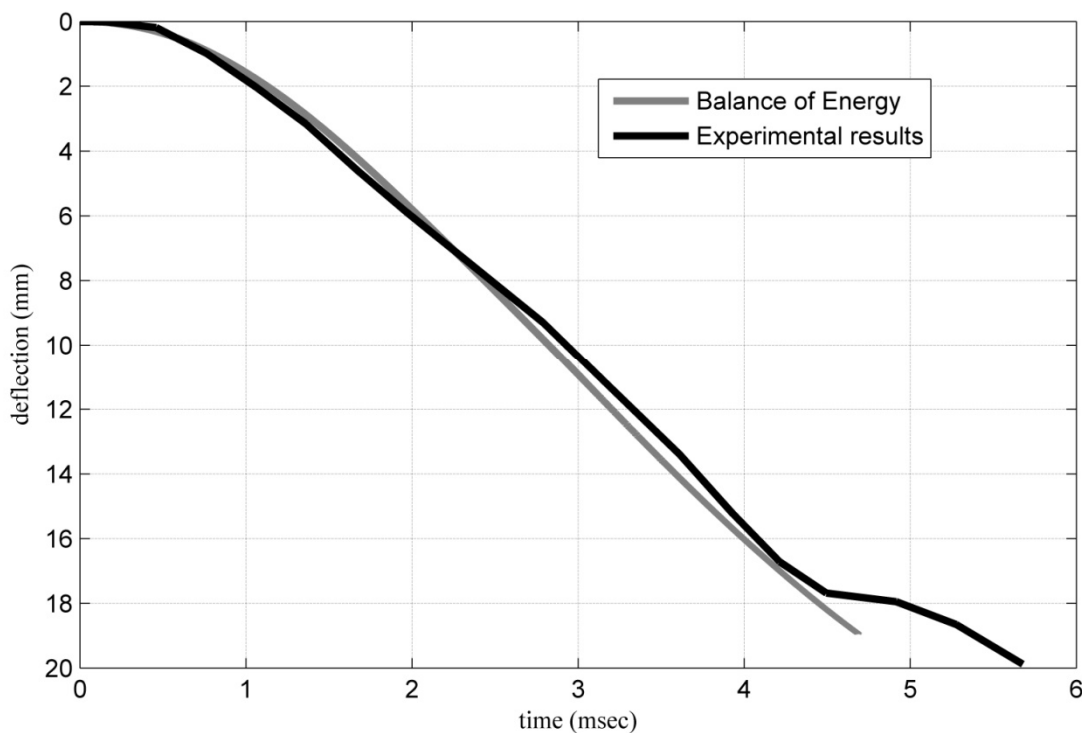
Fig. 39: Time-histories of the maximum deflection of beam B40-D5 (tested in [16]), calculated by means of balance of energy and comparison with experimental findings.

Fig. 40 represents the time-histories of the maximum deflection of beam B40-D5, calculated by means of different theoretical (dynamic and energy) models, as compared with experimental findings. It is clear that the energy model presented in Chapter 2.2, even with the rough simplification regarding the deformed-shape assumption, fits experimental results. In addition, it performed better than the continuous beam dynamic model as regards ultimate displacement (18.9 mm). The ultimate strain on concrete obtained by this model is $\varepsilon_{c,lim,dyn} = 0.0045$, while maximum steel strain is $\varepsilon_s = 0.0061$ and $\varepsilon_{ss} = 0.0020$. Table 13 reports the comparison between the strain result for concrete and strain, referring to different models and experimental results. The energy model proves to be reliable in defining these values as well.

Beam Label: B40-D5	Energy	Cont. Beam Dynamic	Experimental
Maximum strain on concrete	0.0045	0.0044	0.0037
Maximum strain on tensile steel	0.0061	0.0056	-
Maximum strain on compressed steel	0.0020	0.0020	-

Table 13 : Beam B40-D5, strains on concrete and steel obtained by continuous-beam dynamic model, energy model and experimental findings.

Fig. 41 represents the time history of of the maximum curvature of beam B40-D5, calculated by means of balance of energy in comparison with dynamic continuous beam findings.

In order to better appreciate the importance of this energy model, the author has also calculated displacement and curvature distribution along the beam axis. Fig. 42 represents a comparison between curvatures of beam B40-D5 at different times, predicted by the continuous beam model and the balance of energy model. Thus, the sinusoidal shape of displacement also influences curvature distribution and, obviously, during initial instants, the difference between the dynamic approach and the energy approach is clear. After a few msecs, the energy model improves its performance, reducing this difference.
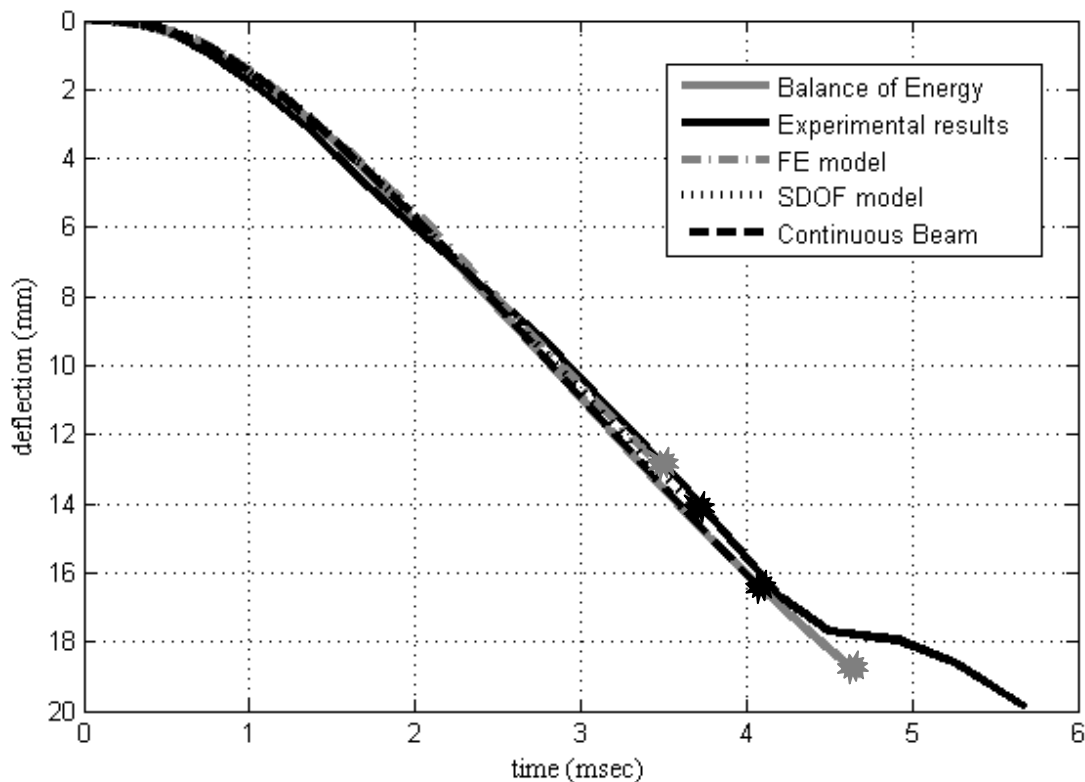
Fig. 40: Time-histories of the maximum deflection of beam B40-D5 (tested in [16]), calculated by means of different theoretical (dynamic and energy) models, and comparison with experimental findings. The spots represent the collapse for each theoretical model.
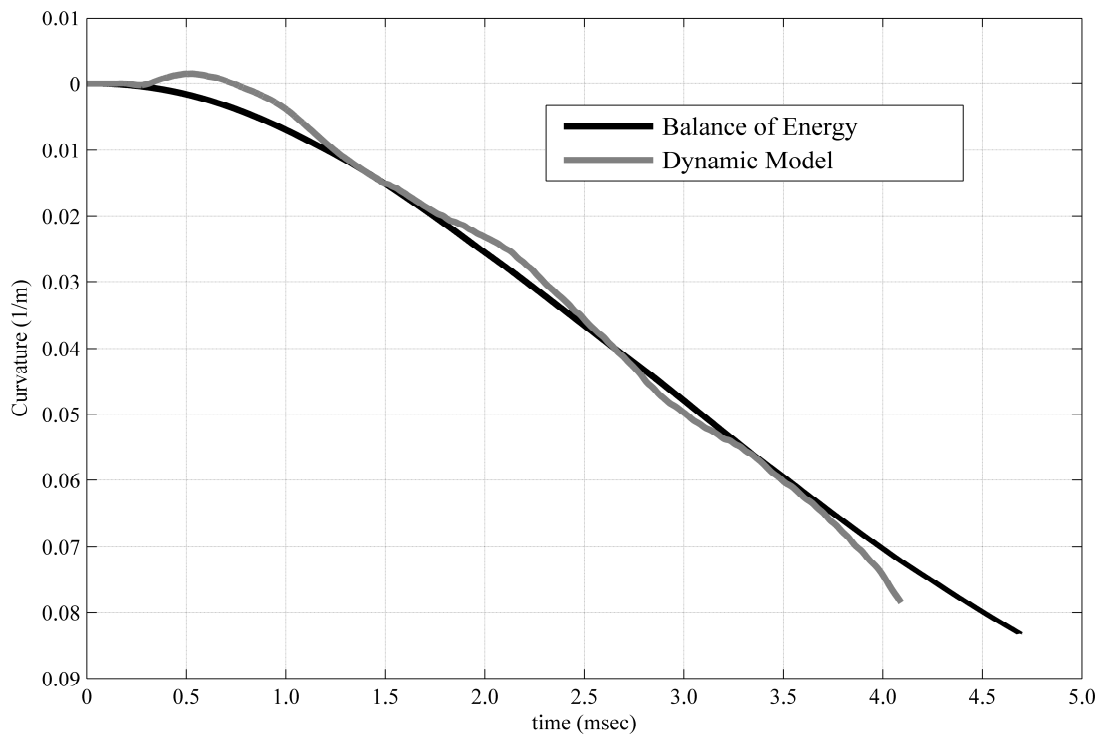
Fig. 41: Time-histories of the maximum curvature of beam B40-D5, calculated by means of balance of energy, and comparison with dynamic continuous beam findings.
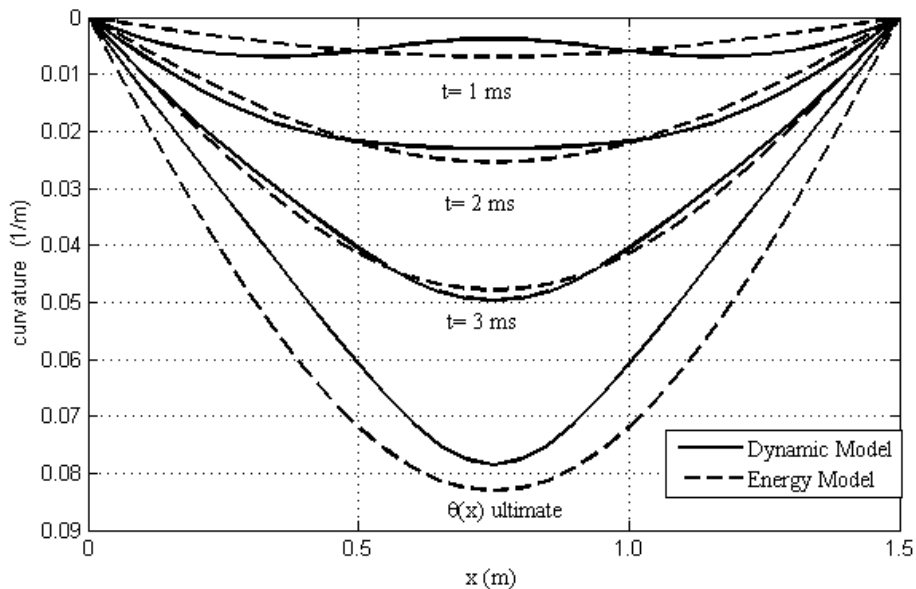
Fig. 42: Comparison between curvatures of beam B40-D5 at different times, predicted by the continuous beam model and the balance of energy model.

The comparison between displacements of beam B40-D5 at different times, predicted by the continuous beam model and the balance of energy model, is depicted in Fig. 43. In the case of displacement analysis, the sinusoidal shape shows some differences as compared with the continuous dynamic model.
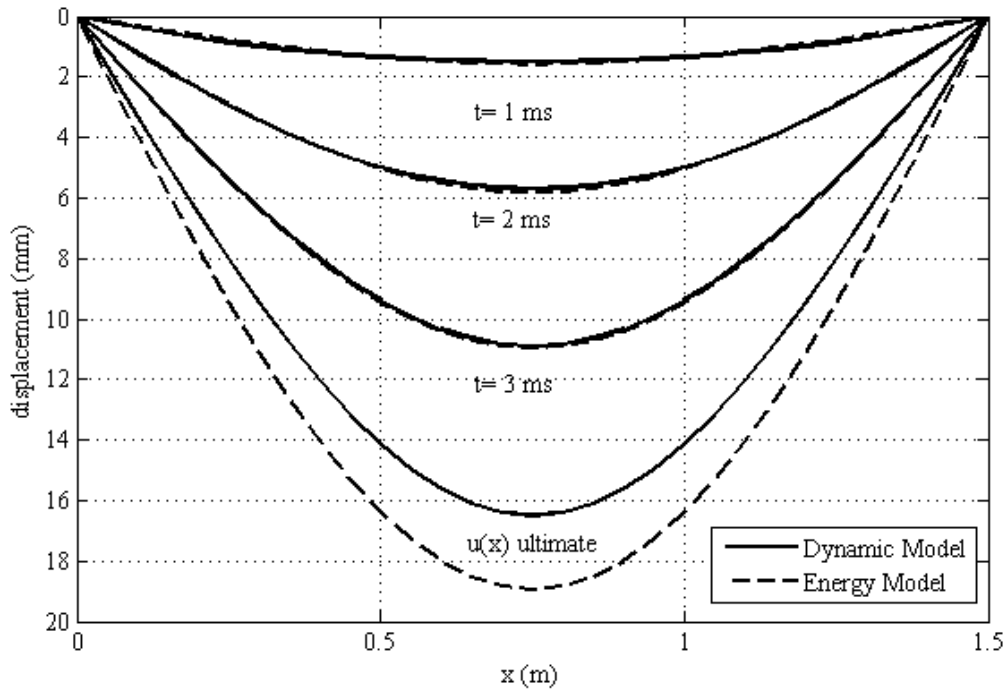
Fig. 43: Comparison between displacements of beam B40-D5 at different times, predicted by the continuous beam model and the balance of energy model.
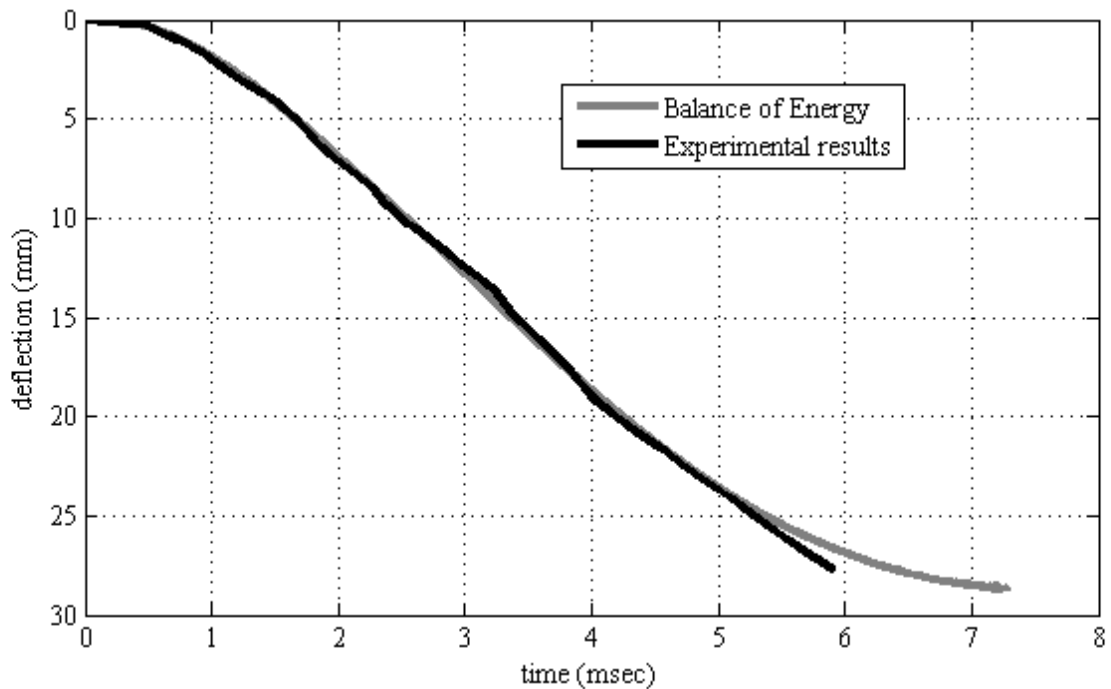
Fig. 44: Time-histories of the maximum deflection of beam B200/40-D3 (tested in [16]), calculated by means of balance of energy, and comparison with experimental findings.

To synthesize, only the most significant results concerning the beam labelled B200/40-D3 are presented. Fig. 44 represents time-histories of the maximum deflection calculated by means of

balance of energy, and comparison with experimental findings. The grey line corresponds to the energy model, the black one to experimental findings. It is important to underline that in this case the model overestimates the structural response of the beam, even if its performance is good. Fig. 45 shows the time-histories of the maximum deflection of beam B200/40-D3, calculated by means of different theoretical (dynamic and energy) models, as compared with experimental findings. The energy model fits experimental data better than the others as regards deflection. On the other hand, considering Table 14, the maximum materials strain produced by this model is lower than experimental and continuous-beam dynamic model results.
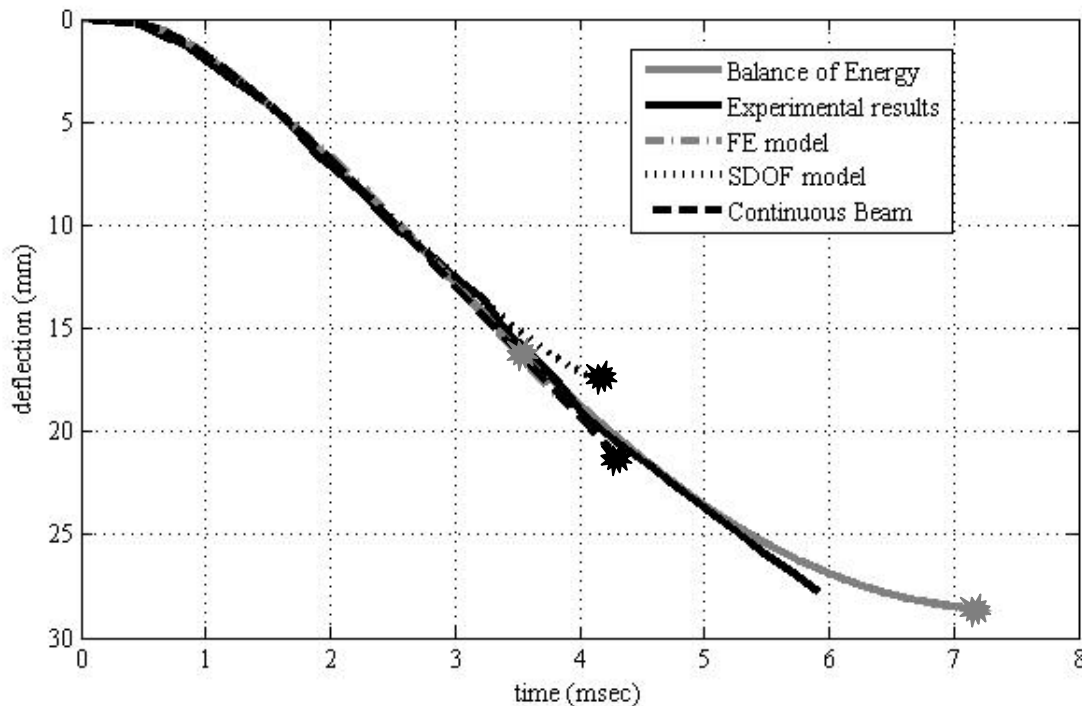
Fig. 45: Time-histories of the maximum deflection of beam B200/40-D3 (tested in [16]), calculated by means of different theoretical (dynamic and energy) models, and comparison with experimental findings. The spots represent the collapse for each theoretical model.

Beam Label: B200/40-D3	Energy	Cont. Beam Dynamic	Experimental
Maximum strain on concrete	0.0034	0.0050	0.0050
Maximum strain on tensile steel	0.0128	0.0280	-
Maximum strain on compressed steel	0.0004	0.0026	-

Table 14 : Beam B200/40-D3, strain on concrete and steel obtained by continuous beam dynamic model, energy model and experimental findings.

SECTION 3:

SENSITIVITY ANALYSIS

Chapter 3.0 Section Introduction

The random nature of the explosion load, associated with the random nature of material properties and geometric dimensional characteristics, implies the need to consider them in the analysis in order to have a more correct estimation of structural behaviour. Therefore, when the randomness of these parameters is taken into consideration, the response of the structure assumes a probabilistic nature, making it necessary to look into the reliability measure. The probabilistic approach to structural reliability in the case of a blast load is a current topic in structural engineering. In quite an early work [107], Low and Hao presented results from a parametric investigation of the reliability of reinforced concrete slabs under blast loading. The authors considered an equivalent non-linear SDOF system, also taking into account the strain-rate effect. To verify the validity of the SDOF simplification, a Monte Carlo simulation was performed to estimate failure probabilities. Then a parametric calculation was developed in order to investigate the effects of various parameters on slab reliability. In [108], Rong and B. Li developed a probabilistic analysis of maximum displacement and ductility factors for a reinforced concrete flexural member under blast loading, using a non-linear dynamic analysis of its equivalent SDOF system. The Monte Carlo simulation method was used in this paper, and the authors obtained two non-dimensional indices quantifying differences between real response and the one obtained by means of the SDOF model. An interesting sensitivity analysis was obtained by Borenstein and Benaroya in [109] in order to determine which parameter uncertainties have the greatest effect on the maximum deflection of a clamped aluminium plate subjected to a blast load. The Monte Carlo simulation was also used in this case. The authors took into account some blast-wave parameters such as loading duration time. Actually, they state that the response of the plate is most sensitive to the latter variable.

In some recent works [2], [3], [4], the same topic is analysed, and some of the results obtained in these papers are presented through this thesis in an extended version.

Chapter 3.1 Sensitivity analysis methodology

The complexity of blast-loading problems from a structural viewpoint was discussed in the previous sections of this work (Section 1 and Section 2). In order to face such a complex problem, it is essential to determine the key parameters in blast load response. For this reason, a sensitivity analysis is developed in this part of the thesis. Numerical simulations by means of the previous SDOF model[13] (see §1.2) are developed, considering different load scenarios and beam geometrical and strength characteristics. In this way, it is possible to search for any correlations between the response of the SDOF in terms of displacement/velocity and the different parameters defining the dynamic problem: peak load, slenderness, span length, etc.

3.1.1 Load and geometrical/strength characteristics

Two kinds of uniformly-distributed loads characterized by a triangular time history are assumed (see Fig. 46): high load and low load. The former is defined by a peak load P randomly varying between 0.8-0.4·10^6 N and positive phase duration between 2.7 and 5 msec, the latter by a peak pressure between 0.4 and 0.1·10^6 N and positive phase duration between 2.7 and 5 msec
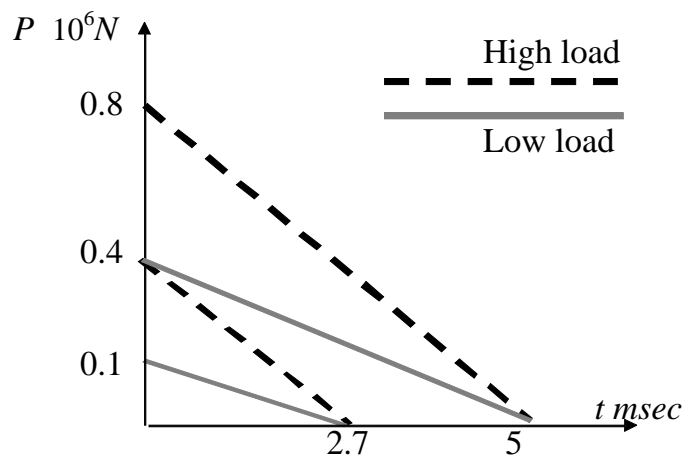
Fig. 46: Time-histories of the two load conditions: low and high.

The beams considered in the simulations are simply supported, and their geometrical/strength characteristics vary randomly within the limits reported in Table 15. In this way, it is possible to consider a wider range of solutions referring to the most common real cases.

---

[13] This SDOF dynamic model was chosen because it is very convenient from a computational point of view even if it is less accurate than the dynamic/energy continuous beams model. As it will become clear in the following paragraphs the need of short computational time is of fundamental importance in this analysis.
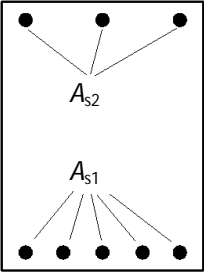
Span m	6÷12
Slenderness L/h	9-15
Width	h/2.5
$\rho_{s1} = \dfrac{A_{s1}}{b \cdot d}$	0.005÷0.01
$\rho_{As} = \dfrac{A_{s2}}{A_{s1}}$	0.25÷0.5
Concrete MPa	fck=20÷40
Steel	B450 C

Table 15 : Geometrical and strength characteristics of beams with their variation range.

3.1.2 Reliability measures

4000 runs of the SDOF model were performed, 2000 under high load and 2000 under low load. A summary of the ultimate state check is shown in Fig. 47. For the sake of clarity it is important to remember that the collapse criterion is always the same considered in the previous sections and it corresponds to the attainment of the ultimate concrete strain. It is clear that in the case of high load and slenderness greater than 12, the percentage of failures reaches 50%; on the contrary, in case of low load and lower slenderness, almost all beams resist the blast load.
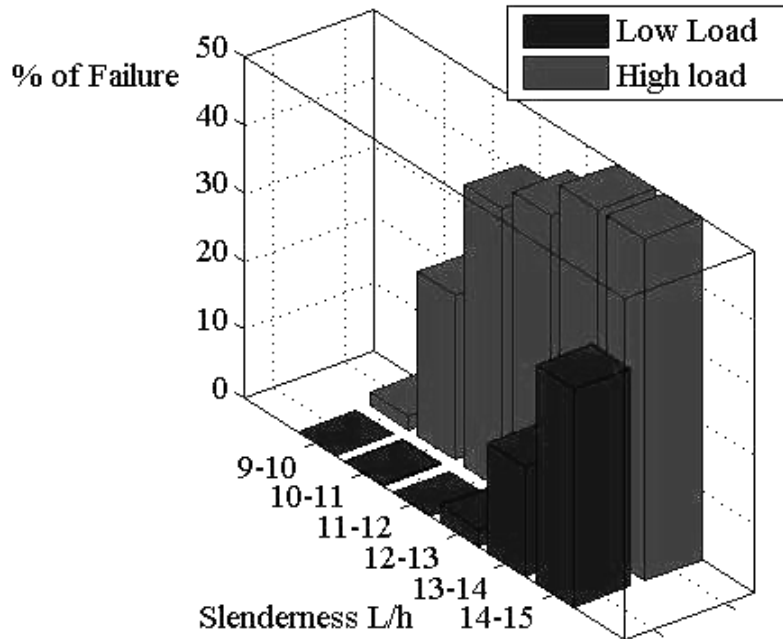
Fig. 47: Collapse percentage of the beams examined with reference to both load scenarios.

These results are important because they underline the role of an important parameter: slenderness of the beam defined as the ratio between span length and the effective height of the cross-section. Correlation between structural reliability and slenderness is possible, and it is obviously linked to the fact that in the case of flexural models, beam stiffness is strictly dependent on the latter parameter.

3.1.3 Validity of fitting parameters

In the following § 3.2, a thorough analysis will be developed considering various fitting models representing different relationships between variables in the problems considered. In order to quantitatively evaluate the quality of fitting, it is necessary to define some statistical parameters:

- Sum of Squares Due to Error: it is simply the sum of the squared difference between response value y_i and the predicted response value $\hat{y}_i$ (see Eq. (124)).

$$SSE = \sum_{i=1}^{n}(y_i - \hat{y}_i)^2 .$$

(124)

- R-Square: it is an index representing how fit explains variation in data. It is defined in Eq. (127) as the ratio between the sum of squares regarding the mean $\overline{y}$ of regression (Eq.(125)) and the sum of squares regarding the mean $\overline{y}$ of the response value (see Eq. (126)). Due to its definition, R-Square assumes values between zero and one. A value equal to 0.72 means that fit explains 72% of the total variation in data as regards the average. For this reason, the best fits have higher R-Square values.

$$SSR = \sum_{i=1}^{n}(\hat{y}_i - \overline{y})^2 ,$$

(125)

$$SST = \sum_{i=1}^{n}(y_i - \overline{y})^2 ,$$

(126)

$$R_{-SQUARE} = \frac{SSR}{SST} .$$

(127)

- Adjusted R-square: it is an optimal indicator of fit validity when it is necessary to compare different models with different numbers of coefficients if residual degrees of freedom v are defined as the difference between response values m and fitted coefficients h, estimated from response values (see Eq (128)). The AR-square is defined by Eq. (129) and can have only a value less than or equal to one. Models with AR-square near 1 are better. There is the possibility of negative values; in this case, it means that the model contains terms that do not help in predicting response.

$$v = h - m ,$$

(128)

$$adjusted\ R_{-SQUARE} = 1 - \frac{SSE\,(h-1)}{SST\,(v)} .$$

(129)

- Root Mean Squared Error: it is a measure of the standard deviation of the random component in the data. It is defined by Eq. (130) and values closer to zero mean that the model fits well with response values.

$$RMSE = \sqrt{\frac{SSE}{v}} \, .$$

(130)

Chapter 3.2 Results

3.2.1 Two-dimensional relationship

In the case of a blast load on reinforced concrete beams, several parameters should be considered, as shown in the previous sections of this work. In this paragraph, the influence of three variables is discussed: span length, slenderness and peak load. Indeed, given the slenderness the span length corresponds to the mass of the beam and, in impulsive load regime, it is crucial to determine the initial velocity see Eq. (15). The slenderness is strictly linked to the beam flexural stiffness and the peak load is a key parameter to identify the load. In order to discover the influence of these variables, Fig. 48 - Fig. 59 have been prepared. In these figures correlations between maximum deflection or velocity (obtained by SDOF during numerical simulations) and span length, slenderness and peak load are investigated, considering only beams which have withstood the load. In the same figures, the fitting polynomial expressions obtained by means of the least square interpolation method are shown with their fitting goodness.

It is important to distinguish between high-load (Fig. 48 - Fig. 53) and low-load (Fig. 54- Fig. 59) conditions. In the former case, the number of non-collapsed beams is greatly inferior as compared to the case of low load.
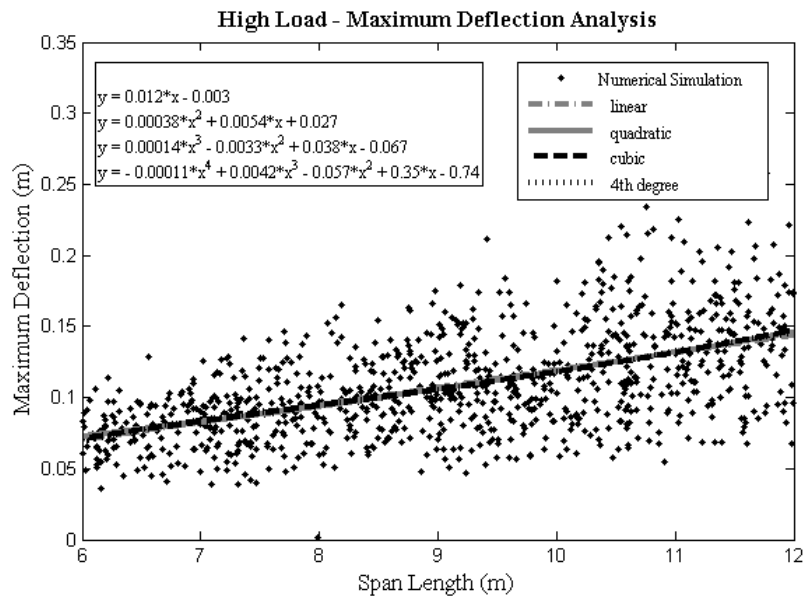
Goodness of fit:

Function	SSE m^2	R-square	Adjusted R-square:	RMSE m
Linear	0.9585	0.2892	0.2884	0.03207
Quadratic	0.9576	0.2898	0.2883	0.03207
Cubic	0.9574	0.2900	0.2877	0.03208
4th degree	0.9569	0.2903	0.2873	0.03209

Fig. 48: High Load, Max. Def. – Span Length: different kinds of polyn. interpolations.
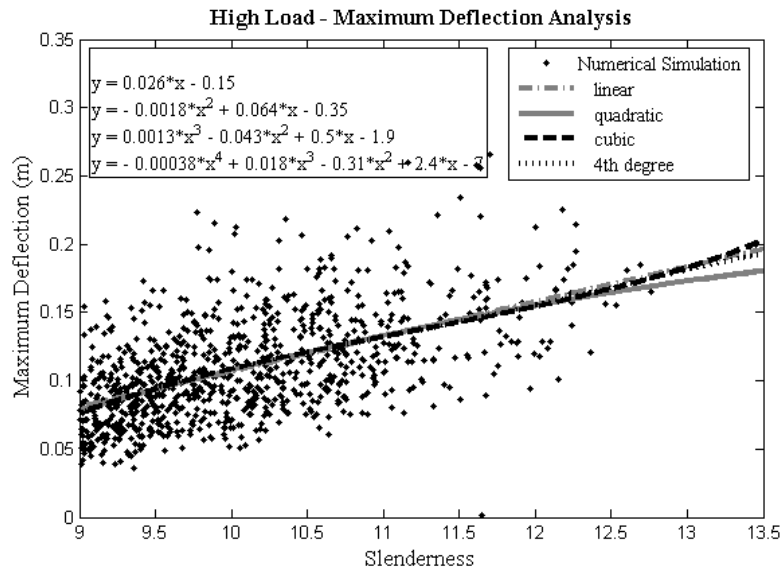
Goodness of fit:

Function	SSE m^2	R-square	Adjusted R-square:	RMSE m
Linear	0.9583	0.2893	0.2886	0.03207
quadratic	0.9562	0.2909	0.2893	0.03205
Cubic	0.9550	0.2918	0.2895	0.03204
4th degree	0.9548	0.2919	0.2889	0.03206

Fig. 49: High Load, Max. Def. – Slenderness different kinds of polyn. interpolations.

Goodness of fit:

Function	SSE m^2	R-square	Adjusted R-square:	RMSE m
linear	1.265	0.06206	0.06105	0.03684
quadratic	1.263	0.06364	0.06163	0.03683
cubic	1.262	0.06400	0.06098	0.03684
4th degree	1.261	0.06504	0.06101	0.03684

Fig. 50: High Load, Max. Def. – Peak Load: different kinds of polyn. interpolations.

Referring to Fig. 48, Fig. 49 and Fig. 50 (depicting high load–maximum deflection results), it is possible to note that beams with slenderness greater than 12 and peak load greater than $7 \cdot 10^5$ N have almost all failed. Hence, the influence of these two important parameters is inferior as compared to what happens in the case of low load. In other words, only beams with a narrow range of slenderness (9-11) and peak-load variation (4-$7 \cdot 10^5$ N) can be considered in the analysis. For this reason, the influence of span length is quite important in the case of high load and less significant in the other load condition.

The general trend in these figures (Fig. 48 - Fig. 50) is that the SSE index decrease as the number of model coefficients increases, while the best AR-square is obtained for the cubic function taking into account correlations between displacement and slenderness or displacement and peak load. Regarding Fig. 48 (correlation between displacement and span length), the AR-square best value corresponds to the linear model; the adding of other coefficients to the model produces a small reduction in SSE but no improvement in variation fitting.

Fig. 51-Fig. 53 depict the curves fitting the correlation between maximum velocities obtained by the SDOF model and the above-mentioned structural parameters in the case of high load. Fitting goodness is not significant for Fig. 51, where the correlation between maximum velocity and span length is investigated: AR-square values are always negative and SSE values are high. Better (but still not very significant) results are obtained for the correlation between maximum velocity and slenderness shown in Fig. 52. In this case, SSE values are lower than in the previous case, but still too high. In Fig. 53, the correlation between maximum velocity and peak load is stated; SSE values are quite low, and AR-square attains better values than in previous cases. Therefore, the best correlation concerning velocity seems to be the one with peak load.
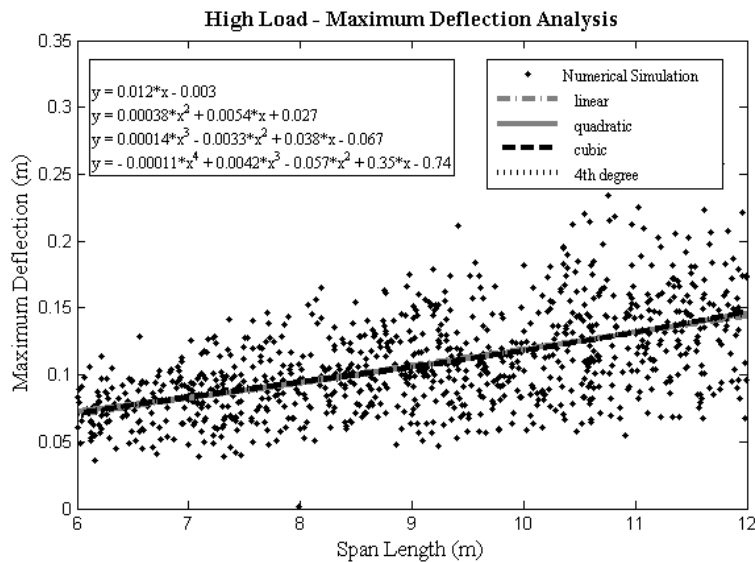
Goodness of fit:

Function	SSE m²/sec²	R-square	Adjusted R-square:	RMSE m/sec
linear	627.8	0.0001453	-0.0009275	0.8207
quadratic	627.4	0.000675	-0.0014720	0.8209
cubic	627.0	0.001370	-0.0018510	0.8211
4th degree	627.0	0.001414	-0.002886	0.8215

Fig. 51: High Load, Max. Vel. – Span Length: different kinds of polyn. interpolations.
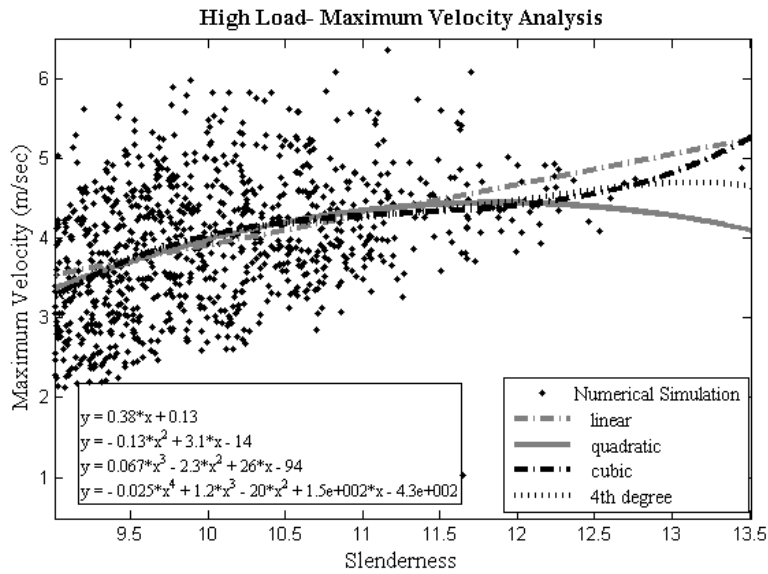
Goodness of fit:

Function	SSE m^2/sec^2	R-square	Adjusted R-square:	RMSE m/sec
linear	542.6	0.1358	0.1349	0.7630
quadratic	532.2	0.1524	0.1505	0.7561
cubic	528.7	0.1579	0.1552	0.7540
4th degree	527.8	0.1593	0.1557	0.7538

Fig. 52: High Load, Max. Vel. – Slenderness: different kinds of polyn. interpolations.
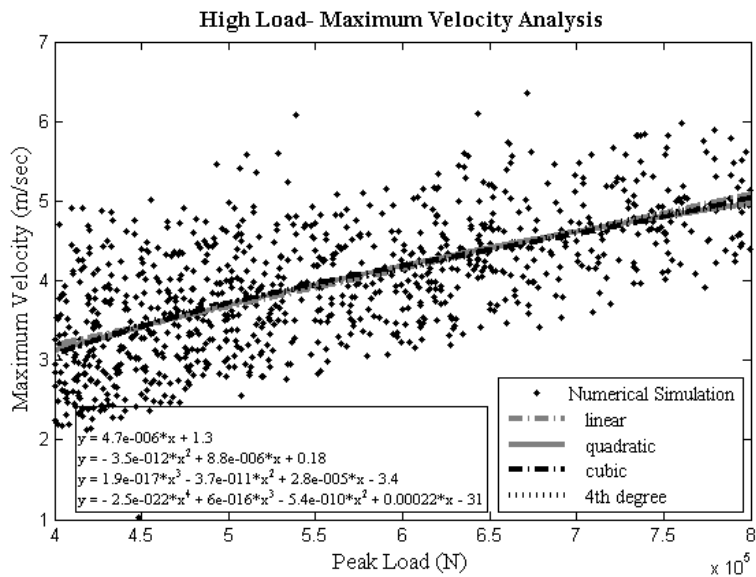
Goodness of fit:

Function	SSE m^2/sec^2	R-square	Adjusted R-square:	RMSE m/sec
linear	371.5	0.4083	0.4077	0.6314
quadratic	370.0	0.4107	0.4095	0.6304
cubic	369.5	0.4115	0.4096	0.6303
4th degree	368.7	0.4128	0.4102	0.6300

Fig. 53: High Load, Max. Vel. – Peak Load: different kinds of polyn. interpolations.

Correlations between maximum deflection reached by the SDOF during numerical simulations in

the case of low load and span length, slenderness and peak load are respectively depicted in Fig. 54, Fig. 55 and Fig. 56. From the analysis of SSE and AR-square indexes, best fits are obtained, considering slenderness as an independent variable. In particular, the cubic function produces the highest AR-square and lowest deviation expressed by quite low SSE and RMSE. In the other two cases, SSE tends to decrease slightly as the number of model coefficients increases, but fit is always worse than in the previous case.

In Fig. 57, Fig. 58 and Fig. 59, correlations between the maximum velocity obtained in the case of low load are investigated. As it is happened in high load condition, the best correlation concerns peak load and maximum velocity. This is the case Fig. 59) with the highest variation index (R-square and AR-square) and lowest deviation index (SSE , RMSE). In particular, the 4th degree polynomial function produces the best fit. Correlation between maximum velocity and span length does not appear, and fittings shown in Fig. 57 obtained poor results. Better results are obtained as regards the statistical relationship between maximum velocity and slenderness shown in Fig. 58. In this case as well, SSE decreases as the number of model coefficients increases, but the AR-square, differently from what is shown in other cases, increases as the degree of the fitting polynomial increases.
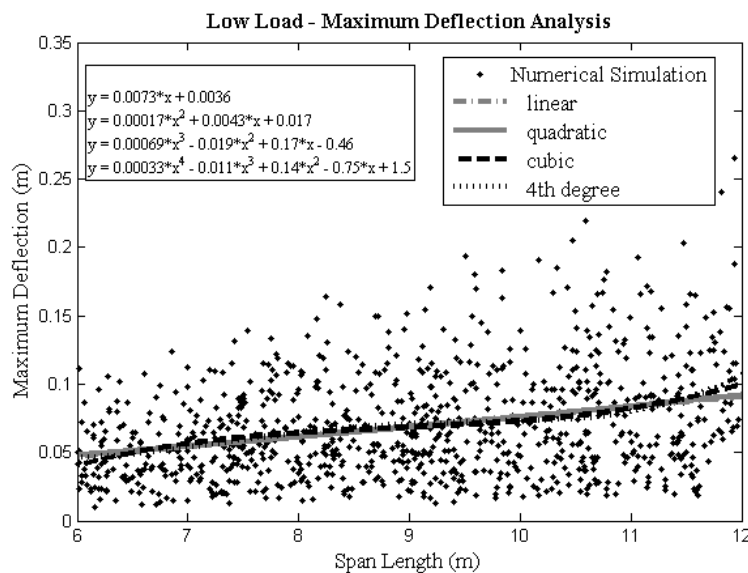
Goodness of fit:

Function	SSE m^2	R-square	Adjusted R-square:	RMSE m
Linear	2.601	0.09676	0.09627	0.03728
Quadratic	2.600	0.09688	0.09591	0.03729
Cubic	2.586	0.10180	0.10040	0.03720
4th degree	2.579	0.10440	0.10250	0.03715

Fig. 54: Low Load, Max. Def. – Span Length: different kinds of polyn. interpolations.
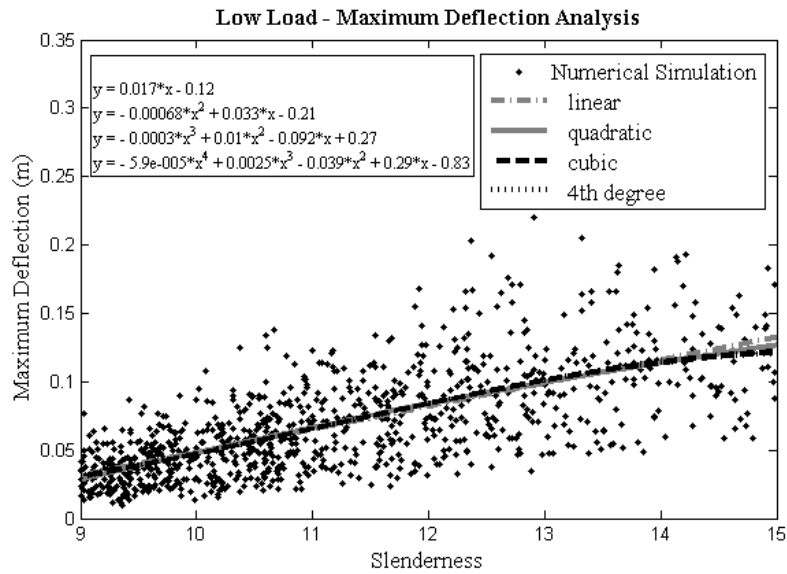
Goodness of fit:

Function	SSE m^2	R-square	Adjusted R-square:	RMSE m
Linear	1.554	0.4601	0.4599	0.02882
Quadratic	1.549	0.4621	0.4615	0.02878
Cubic	1.546	0.4629	0.4621	0.02876
4th degree	1.546	0.4630	0.4619	0.02877

Fig. 55: Low Load, Max. Def. – Slenderness: different kinds of polyn. interpolations.
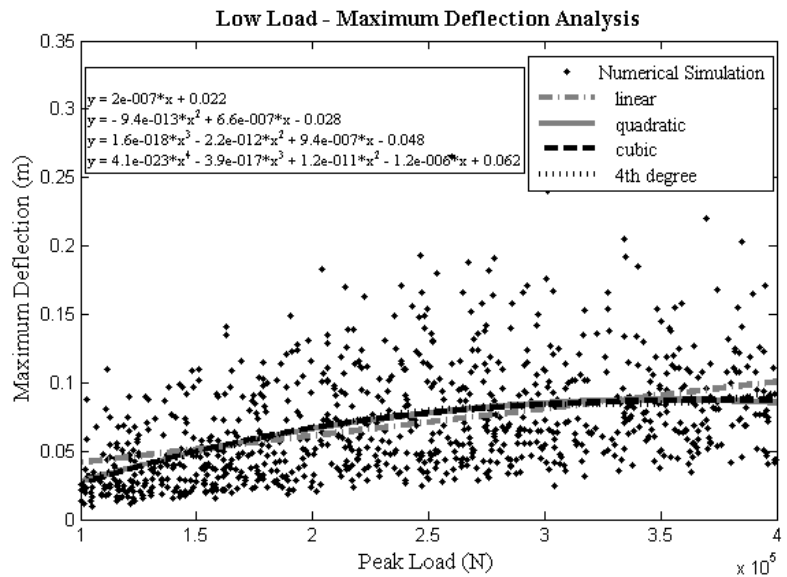
Goodness of fit:

Function	SSE m^2	R-square	Adjusted R-square:	RMSE m
Linear	2.358	0.1811	0.1807	0.03550
Quadratic	2.285	0.2064	0.2056	0.03496
Cubic	2.284	0.2069	0.2056	0.03496
4th degree	2.279	0.2085	0.2068	0.03493

Fig. 56: Low Load, Max. Def. – Peak Load: different kinds of polyn. interpolations.
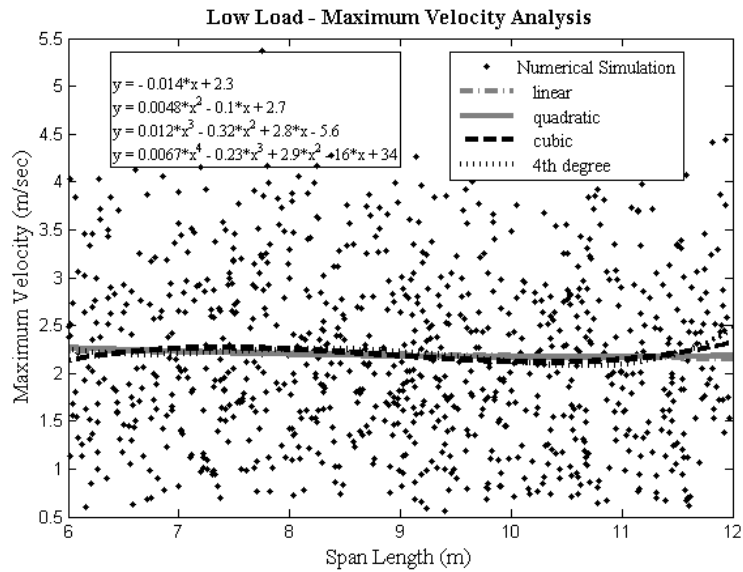
Goodness of fit:

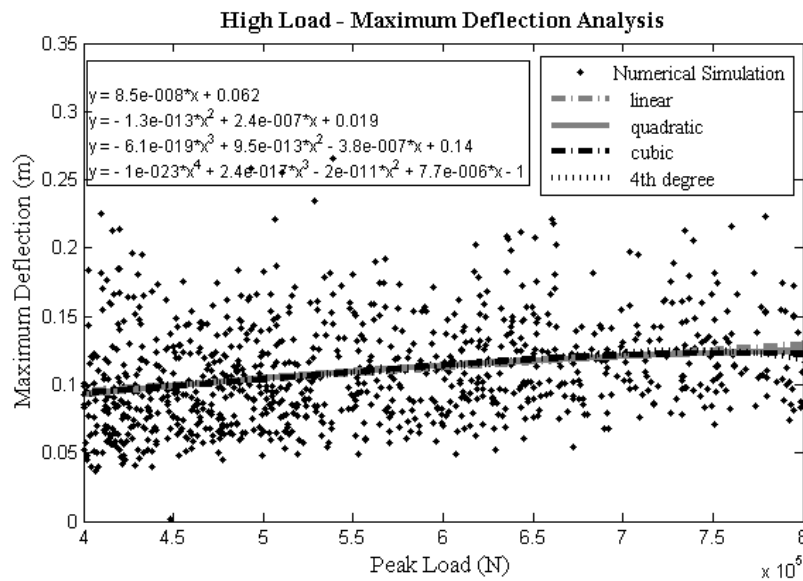| Function	SSE m²/sec²	R-square	Adjusted R-square:	RMSE m/sec
Linear	1520	0.0006535	0.0001194	0.9013
Quadratic	1520	0.0008467	-0.0002219	0.9015
Cubic	1515	0.003721	0.002122	0.9004
4th degree	1512	0.005721	0.003592	0.8998

Fig. 57: Low Load, Max. Veloc.. – Span Length: different kinds of polyn. interpolations.
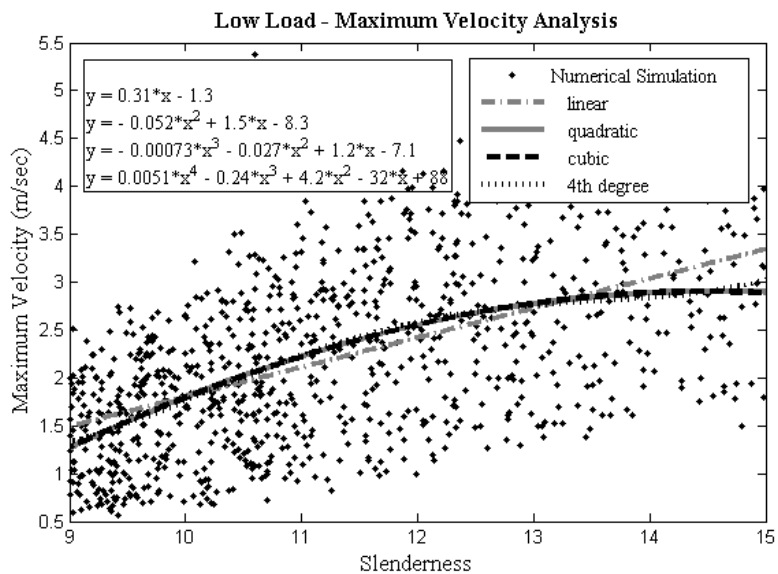
Goodness of fit:

Function	SSE m²/sec²	R-square	Adjusted R-square:	RMSE m/sec
Linear	1077	0.2919	0.2915	0.7587
Quadratic	1045	0.3132	0.3124	0.7474
Cubic	1045	0.3132	0.3121	0.7476
4th degree	1043	0.3143	0.3128	0.7472

Fig. 58: Low Load, Max. Veloc.– Slenderness: different kinds of polyn. interpolations.
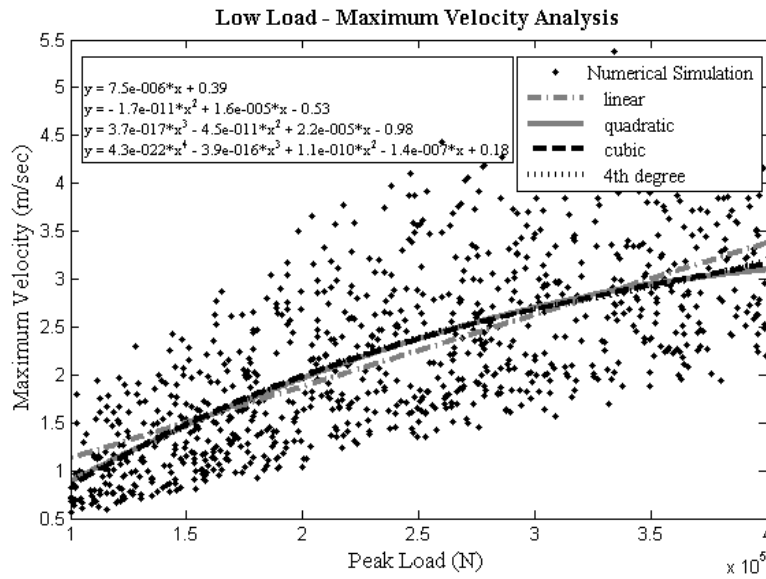
Goodness of fit:

Function	SSE m²/sec²	R-square	Adjusted R-square:	RMSE m/sec
Linear	768.5	0.4947	0.4944	0.6409
Quadratic	744.6	0.5105	0.5100	0.6310
Cubic	743.9	0.5109	0.5101	0.6309
4th degree	743.4	0.5113	0.5102	0.6308

Fig. 59: Low Load, Max. Veloc.– Peak Load: different kinds of polyn. interpolations.

3.2.2 Three-dimensional relationship

In this paragraph, correlations between maximum displacement (deflection) or velocity and some load-structural parameters are investigated in a three-dimensional space. Z is assumed to be the maximum deflection or the maximum velocity and x, y represent the other parameters. Several least squares fitting functions are compared in order to determine better fitting of SDOF numerical results. In order to avoid badly conditioned equations, independent variables are normalised by their mean and standard deviation (see Table 16 and Table 17).

First, Fig. 60 - Fig. 83 show fitting goodness in the case of high load, as concerns maximum displacement. A synthesis of this analysis is shown in Table 18, where the lowest SSE is obtained by a 5th degree polynomial function of span length and slenderness (see Fig. 69). This function also presents the best AR-square index. This leads to the conclusion that P.Load influence is less important than span length as regards maximum deflection in the case of a high load. This can be explained by the fact that the variation range of peak load for this analysis is very narrow (only a few number of beams withstood the load) and so it does not have a strict correlation with variations in results.

variable	mean	Standard Deviation
Slenderness	10.08	0.7963
P.Load	$0.5575 \cdot 10^6$ N	$0.1109 \cdot 10^6$ N
Span	9.167 m	1.669 m
C.Strength	30.26 MPa	2.837 MPa
R.Ratio	0.0076	0.0014

Table 16 : Mean and standard deviation of the parameters considered for high-load analysis.

variable	mean	Standard Deviation
Slenderness	11.27	1.579
P.Load	$0.2419 \cdot 10^6$ N	$0.0845 \cdot 10^6$ N
Span	9.071 m	1.668 m
C.Strength	30.12 MPa	2.85 MPa
R.Ratio	0.0075	0.0014

Table 17 : Mean and standard deviation of the parameters considered for low-load analysis.

x – y	Fit type	SSE m^2	R-SQUARE	AR-SQUARE	RMSE m	Coefficients
Span –Slend.	poly55	0.599829	0.551294	0.541454	0.025646	21
Slend- P.Load	poly55	0.601113	0.550334	0.540473	0.025673	21
Span-Slend.	poly44	0.604141	0.548069	0.541177	0.025654	15
Slend- P.Load	poly44	0.605854	0.546787	0.539876	0.025690	15
Span-Slend.	poly33	0.606089	0.546612	0.542191	0.025625	10
Span-Slend.	poly22	0.606666	0.546180	0.543733	0.025582	6
Slend- P.Load	poly33	0.60937	0.544157	0.539712	0.025694	10
Slend- P.Load	poly22	0.613641	0.540963	0.538487	0.025729	6
Span-Slend.	poly44	0.618171	0.541562	0.534578	0.025936	15
Slend- P.Load	poly11	0.629505	0.529095	0.528083	0.026017	3
Span-Slend.	poly11	0.633605	0.526028	0.525009	0.026102	3
Slend- R.Ratio	poly55	0.664026	0.507555	0.496768	0.026969	21
Span- P.Load	poly55	0.846643	0.372126	0.358372	0.030452	21
Slend.-C.Strength	poly55	0.938409	0.304072	0.288827	0.032060	21

Table 18 : Fitting goodness for high-load maximum deflection results.

From Table 18, it is clear that concrete strength (see Fig. 71) and reinforcement ratio (see Fig. 70) have poor correlation with maximum deflection, and it is important to underline how it is possible to have good fit even with a simple cubic function of slenderness and span length (see Fig. 67).
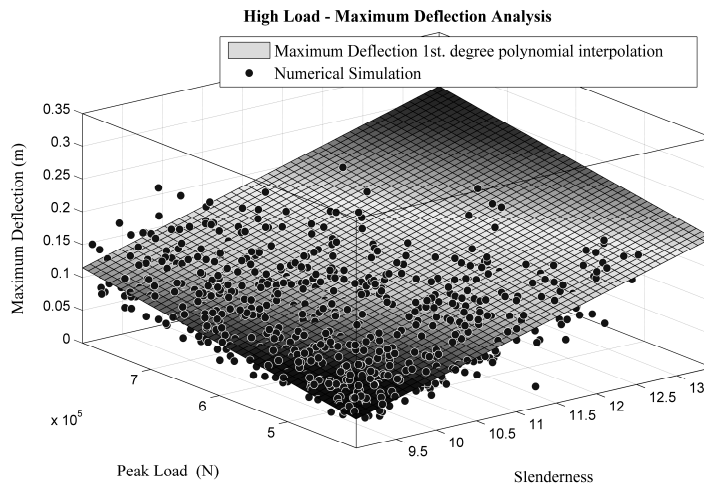
$$f(x, y) = p_0 + p_{10}x + p_{01}y$$

P_0	P_{10}	P_{01}
0.1094	0.02781	0.01948

Goodness of fit:

SSE m^2	R-square	Adjusted R-square:	RMSE m
0.6295	0.5291	0.5281	0.02602

Fig. 60: High Load, Max. Defl. – Peak Load-Slenderness 1st polyn. Interp. and goodness of fit.
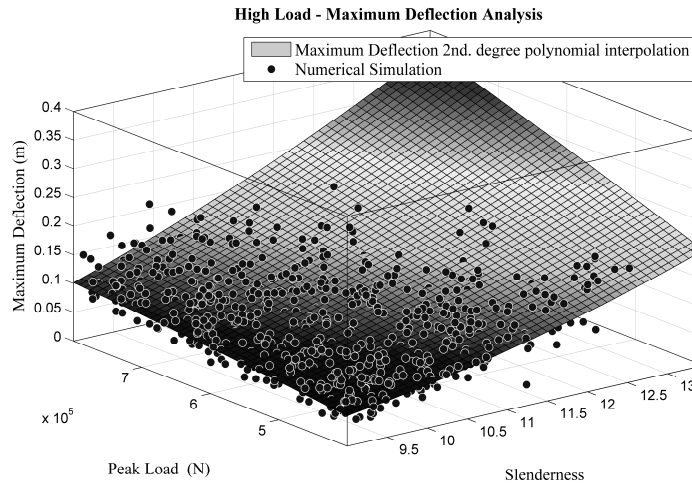
$$f(x, y) = p_0 + p_{10}x + p_{01}y + p_{20}x^2 + p_{11}xy + p_{02}y^2$$

P_0	P_{10}	P_{01}	P_{20}	P_{11}	P_{02}
0.110	0.029	0.022	0.002	0.006	-0.001

Goodness of fit:

SSE m^2	R-square	Adjusted R-square:	RMSE m
0.6136	0.541	0.5385	0.02573

Fig. 61: High Load, Max. Defl. – Peak Load-Slenderness: 2nd deg. polyn. interpolation and goodness of fit.
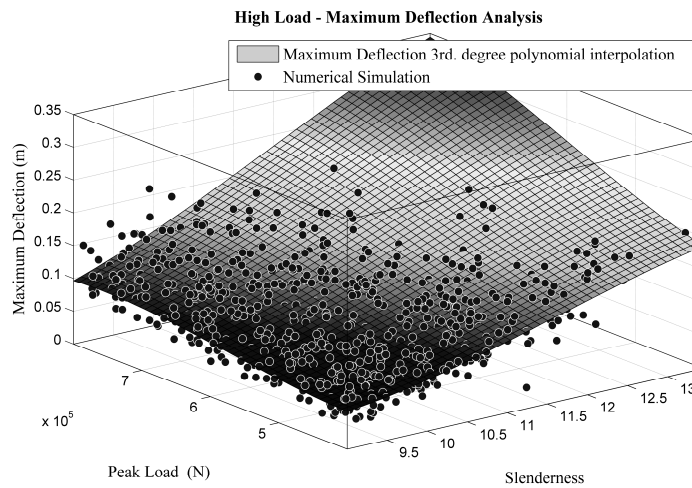
$$f(x, y) = p_0 + p_{10}x + p_{01}y + p_{20}x^2 + p_{11}xy + p_{02}y^2 + p_{30}x^3 + p_{21}x^2y + p_{12}xy^2 + p_{03}y^3$$

P_0	P_{10}	P_{01}	P_{20}	P_{11}	P_{02}	P_{30}	P_{21}	P_{12}	P_{03}
0.108	0.030	0.026	0.003	0.006	0.001	-0.001	-0.000	0.000	-0.002

Goodness of fit:

SSE m^2	R-square	Adjusted R-square:	RMSE m
0.6094	0.5442	0.5397	0.02569

Fig. 62: High Load, Max.- Peak Load - Span-Slenderness 3rd deg. polyn. Interp. and goodness of fit.

$$f(x, y) = p_0 + p_{10}x + p_{01}y + p_{20}x^2 + p_{11}xy + p_{02}y^2 + p_{30}x^3 + p_{21}x^2y + p_{12}xy^2 + p_{03}y^3 + p_{40}x^4 + p_{31}x^3y +$$
$$+ p_{22}x^2y^2 + p_{13}xy^3 + p_{04}y^4$$

P_0	P_{10}	P_{01}	P_{20}	P_{11}	P_{02}	P_{30}	P_{21}	P_{12}	P_{03}	P_{40}	P_{31}	P_{22}	P_{13}	P_{04}
0.109	0.031	0.025	0.004	0.011	0.002	-0.001	0.001	0.000	-0.001	-0.000	-0.002	-0.000	-0.001	-0.001

Goodness of fit:

SSE m^2	R-square	Adjusted R-square:	RMSE m
0.6059	0.5468	0.5399	0.02569

Fig. 63: High Load, Max. Defl. – Peak Load-Slenderness 4th deg. polyn. interpolation and goodness of fit.

$$f(x, y) = p_0 + p_{10}x + p_{01}y + p_{20}x^2 + p_{11}xy + p_{02}y^2 + p_{30}x^3 + p_{21}x^2y + p_{12}xy^2 + p_{03}y^3 + p_{40}x^4 + p_{31}x^3y +$$
$$+ p_{22}x^2y^2 + p_{13}xy^3 + p_{04}y^4 + p_{50}x^5 + p_{41}x^4y + p_{32}x^3y^2 + p_{23}x^2y^3 + p_{14}xy^4 + p_{05}y^5$$

P_0	P_{10}	P_{01}	P_{20}	P_{11}	P_{02}	P_{30}	P_{21}	P_{12}	P_{03}	P_{40}	P_{31}	P_{22}	P_{13}	P_{04}	P_{50}	P_{41}	P_{32}	P_{23}	P_{14}	P_{05}
0.107	0.031	0.023	0.008	0.013	0.003	0.000	0.005	0.004	-0.001	-0.002	-0.002	-0.001	-0.002	-0.001	0.000	-0.000	0.000	-0.002	0.001	0.001

Goodness of fit:

SSE m^2	R-square	Adjusted R-square:	RMSE m
0.6011	0.5503	0.5405	0.02567

Fig. 64: High Load, Max. Defl. - P. Load-Slenderness 5th polyn. interpolation and goodness of fit.

$$f(x, y) = p_0 + p_{10}x + p_{01}y$$

P_0	P_{10}	P_{01}
0.1094	0.0181	0.0185

Goodness of fit:

SSE m^2	R-square	Adjusted R-square:	RMSE m
0.6336	0.526	0.525	0.0261

Fig. 65: High Load, Max. Defl. – Slenderness –Span 1st polyn. interp. and goodness of fit.
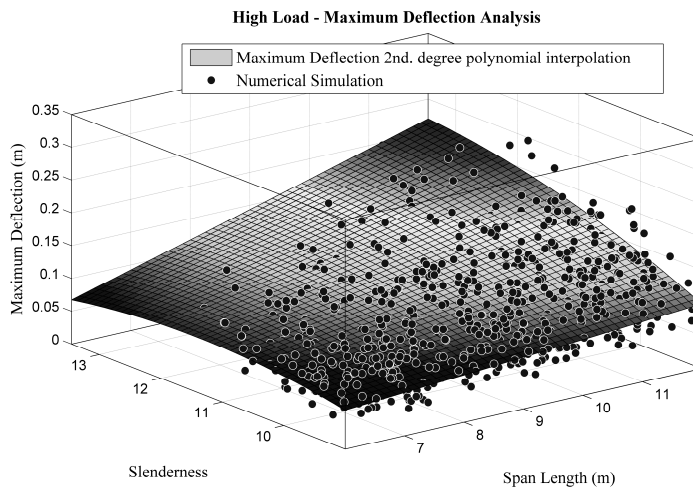
$$f(x, y) = p_0 + p_{10}x + p_{01}y + p_{20}x^2 + p_{11}xy + p_{02}y^2$$

P_0	P_{10}	P_{01}	P_{20}	P_{11}	P_{02}
0.111	0.018	0.019	0.000	0.005	-0.002

Goodness of fit:

SSE m^2	R-square	Adjusted R-square:	RMSE m
0.6067	0.5462	0.5437	0.02558

Fig. 66:High Load, Max. Defl. –Slenderness - Span 2nd deg. polyn. interpolation and goodness of fit.
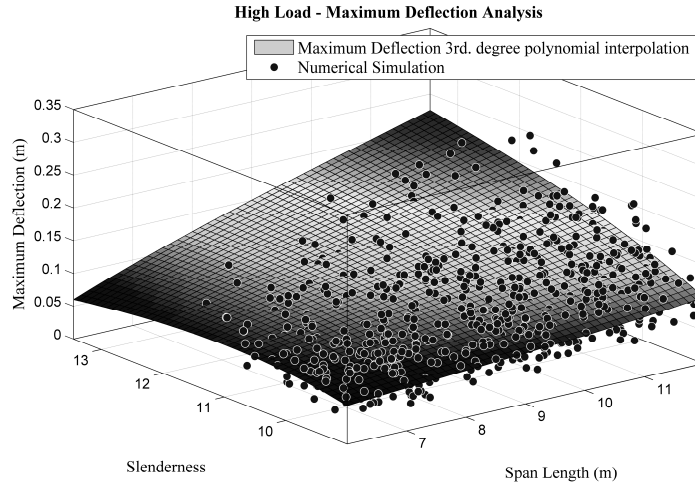
$$f(x, y) = p_0 + p_{10}x + p_{01}y + p_{20}x^2 + p_{11}xy + p_{02}y^2 + p_{30}x^3 + p_{21}x^2y + p_{12}xy^2 + p_{03}y^3$$

P_0	P_{10}	P_{01}	P_{20}	P_{11}	P_{02}	P_{30}	P_{21}	P_{12}	P_{03}
0.111	0.017	0.020	0.003	0.005	-0.002	0.001	-0.001	-0.000	0.000

Goodness of fit:

SSE m^2	R-square	Adjusted R-square:	RMSE m
0.6061	0.5466	0.5422	0.02563

Fig. 67: High Load, Max Def.- Slenderness - Span 3rd deg. polyn. interp. and goodness of fit.
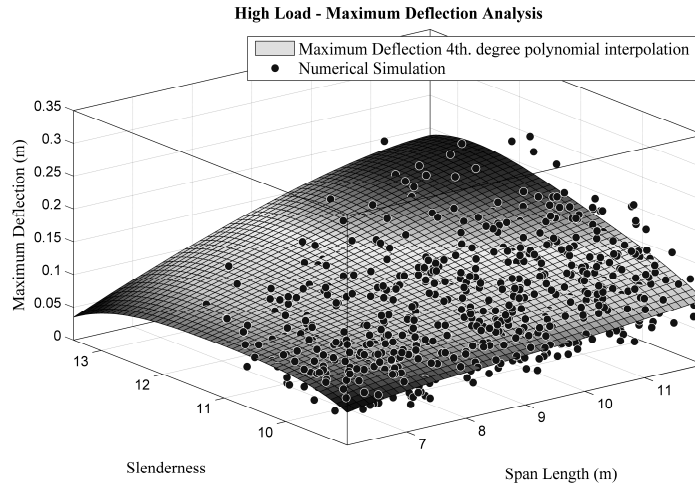
$$f(x, y) = p_0 + p_{10}x + p_{01}y + p_{20}x^2 + p_{11}xy + p_{02}y^2 + p_{30}x^3 + p_{21}x^2y + p_{12}xy^2 + p_{03}y^3 + p_{40}x^4 + p_{31}x^3y +$$
$$+ p_{22}x^2y^2 + p_{13}xy^3 + p_{04}y^4$$

P_0	P_{10}	P_{01}	P_{20}	P_{11}	P_{02}	P_{30}	P_{21}	P_{12}	P_{03}	P_{40}	P_{31}	P_{22}	P_{13}	P_{04}
0.111	0.017	0.017	0.002	0.005	-0.002	0.001	-0.000	0.000	0.002	-0.000	-0.000	-0.000	0.000	-0.000

Goodness of fit:

SSE m^2	R-square	Adjusted R-square:	RMSE m
0.6041	0.5481	0.5412	0.02565

Fig. 68: High Load, Max. Defl. –Slenderness Span 4th deg. polyn. interpolation and goodness of fit.

$$f(x,y) = p_0 + p_{10}x + p_{01}y + p_{20}x^2 + p_{11}xy + p_{02}y^2 + p_{30}x^3 + p_{21}x^2y + p_{12}xy^2 + p_{03}y^3 + p_{40}x^4 + p_{31}x^3y +$$

$$+ p_{22}x^2y^2 + p_{13}xy^3 + p_{04}y^4 + p_{50}x^5 + p_{41}x^4y + p_{32}x^3y^2 + p_{23}x^2y^3 + p_{14}xy^4 + p_{05}y^5$$

P_0	P_{10}	P_{01}	P_{20}	P_{11}	P_{02}	P_{30}	P_{21}	P_{12}	P_{03}	P_{40}	P_{31}	P_{22}	P_{13}	P_{04}	P_{50}	P_{41}	P_{32}	P_{23}	P_{14}	P_{05}
0.110	0.010	0.016	0.002	0.005	-0.000	0.007	0.000	0.004	0.003	-0.001	0.001	0.000	-0.000	-0.001	-0.001	0.000	-0.002	-0.000	0.000	0.000

Goodness of fit:

SSE m^2	R-square	Adjusted R-square:	RMSE m
0.5998	0.5513	0.5415	0.02565

Fig. 69: High Load, Maximum Defl. – Slenderness - Span 5th polyn. interp. and goodness of fit.

$$f(x,y) = p_0 + p_{10}x + p_{01}y + p_{20}x^2 + p_{11}xy + p_{02}y^2 + p_{30}x^3 + p_{21}x^2y + p_{12}xy^2 + p_{03}y^3 + p_{40}x^4 + p_{31}x^3y +$$

$$+ p_{22}x^2y^2 + p_{13}xy^3 + p_{04}y^4 + p_{50}x^5 + p_{41}x^4y + p_{32}x^3y^2 + p_{23}x^2y^3 + p_{14}xy^4 + p_{05}y^5$$

P_0	P_{10}	P_{01}	P_{20}	P_{11}	P_{02}	P_{30}	P_{21}	P_{12}	P_{03}	P_{40}	P_{31}	P_{22}	P_{13}	P_{04}	P_{50}	P_{41}	P_{32}	P_{23}	P_{14}	P_{05}
0.112	0.024	-0.015	-0.006	-0.002	-0.006	0.000	-0.001	-0.008	0.000	0.002	-0.001	-0.000	0.000	0.004	-0.000	0.001	0.000	-0.001	0.002	0.000

Goodness of fit:

SSE m^2	R-square	Adjusted R-square:	RMSE m
0.664	0.5076	0.4968	0.02697

Fig. 70: High Load, Max. Defl. – Reinf. Ratio- Slenderness 5th polyn. interp. and goodness of fit.

High Load - Maximum Deflection Analysis
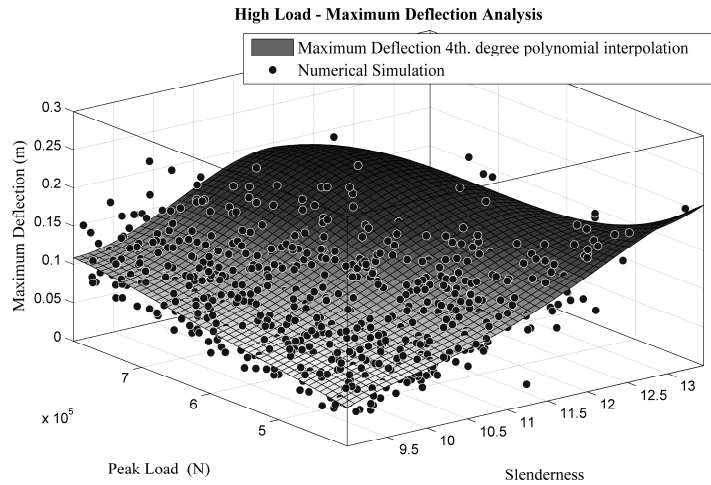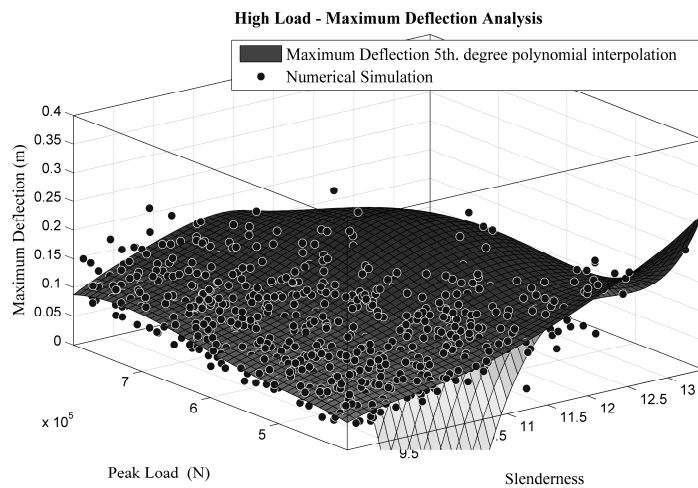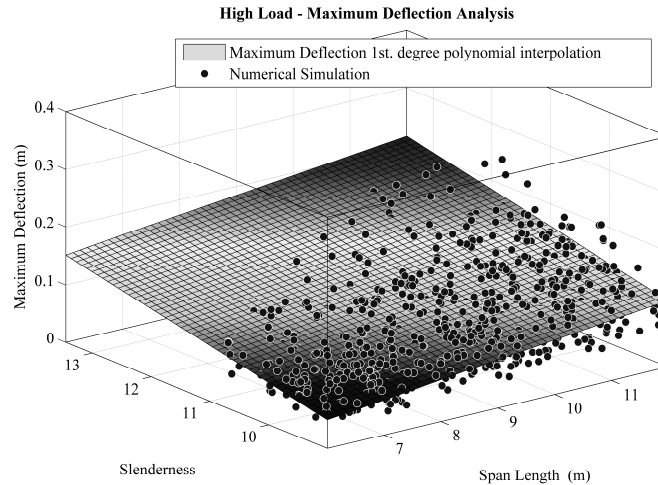
$$f(x,y) = p_0 + p_{10}x + p_{01}y + p_{20}x^2 + p_{11}xy + p_{02}y^2 + p_{30}x^3 + p_{21}x^2y + p_{12}xy^2 + p_{03}y^3 + p_{40}x^4 + p_{31}x^3y +$$

$$+ p_{22}x^2y^2 + p_{13}xy^3 + p_{04}y^4 + p_{50}x^5 + p_{41}x^4y + p_{32}x^3y^2 + p_{23}x^2y^3 + p_{14}xy^4 + p_{05}y^5$$

P_0	P_{10}	P_{01}	P_{20}	P_{11}	P_{02}	P_{30}	P_{21}	P_{12}	P_{03}	P_{40}	P_{31}	P_{22}	P_{13}	P_{04}	P_{50}	P_{41}	P_{32}	P_{23}	P_{14}	P_{05}
91.89	-23.83	-0.000	0.419	0.000	-0.000	0.508	-0.000	0.000	0.000	-0.043	0.000	0.000	-0.000	0.000	0.001	-0.000	-0.000	0.000	0.000	-0.000

Goodness of fit:

SSE m^2	R-square	Adjusted R-square:	RMSE m
0.9384	0.3041	0.2888	0.03206

Fig. 71: High Load, Max. Defl. – Conc. Strength- Slenderness 5th polyn. interp. and goodness of fit.

Fig. 72 - Fig. 83 represent fitting goodness in the case of high load, as concerns maximum velocity. A synthesis of this analysis is shown in Table 19, where the lowest SSE is obtained by a 5th degree polynomial function of slenderness and peak load (see Fig. 76). The best AR-square index corresponds to a 3rd degree polynomial function of the same variables. From these results, it is clear that the most important parameters fitting maximum velocity/high load results are peak load and slenderness. Other variables obtained dramatically worse results. Finally, it is interesting to underline the importance of the peak load, whose function occupies the first seven positions in Table 19. Actually, the slenderness function develops worse fitting goodness, these observations confirming what was stated about Fig. 53 in the previous paragraph 3.2.1

| x – y	Fit type	SSEm^2/sec^2	R-SQUARE	AR-SQUARE	RMSE m/sec	Coefficients
Slend.-P.Load	poly55	91.67459508	0.851965086	0.848718707	0.317049506	21
Slend.-P.Load	poly44	92.23189316	0.851065169	0.848793832	0.316970774	15
Slend.-P.Load	poly33	92.49950564	0.850633032	0.849176583	0.316569343	10
Slend.-P.Load	poly22	92.92596403	0.849944393	0.849135031	0.316612947	6
Slend.-P.Load	poly11	98.40803253	0.841092021	0.840750284	0.325292313	3
P.Load.-C.Stren.	poly33	357.6543056	0.422464597	0.416833157	0.622487849	10
P.Load – Span.	poly33	362.5423019	0.414571526	0.408863122	0.626727128	10
Slend.-Span	poly55	508.139387	0.179463294	0.161469068	0.746438464	21
Slend.-Span	poly44	510.7910993	0.175181345	0.162602411	0.745933857	15
Slend.-C.Stren.	poly33	511.2570454	0.174428941	0.166378952	0.74424993	10
Slend.-Span	poly33	512.3703241	0.172631233	0.164563716	0.745059803	10
Slend.-Span	poly22	515.5991811	0.167417318	0.162926581	0.745789462	6
Slend.-Span	poly11	529.3251071	0.145252876	0.14341471	0.75443143	3

Table 19 : Fitting goodness for high-load maximum velocity results.
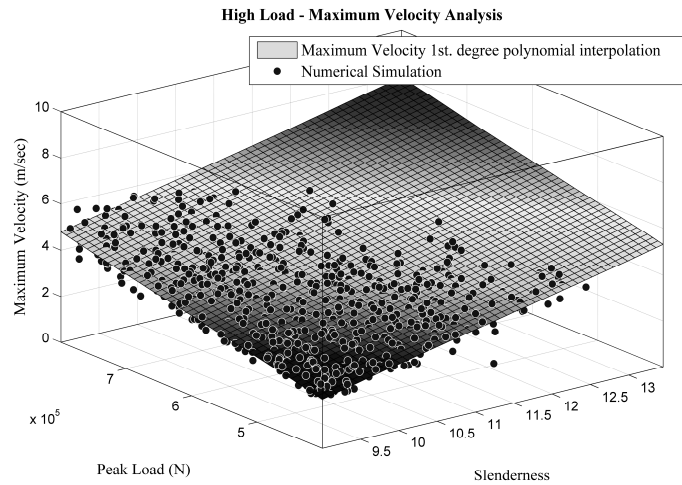
$$f(x, y) = p_0 + p_{10}x + p_{01}y$$

P_0	P_{10}	P_{01}
3.952	0.5749	0.7306

Goodness of fit:

SSE m^2/sec^2	R-square	Adjusted R-square:	RMSE m/sec
98.41	0.8411	0.8408	0.3253

Fig. 72: High Load, Max. Vel. – Peak Load – Span 1st polyn. interp. and goodness of fit.
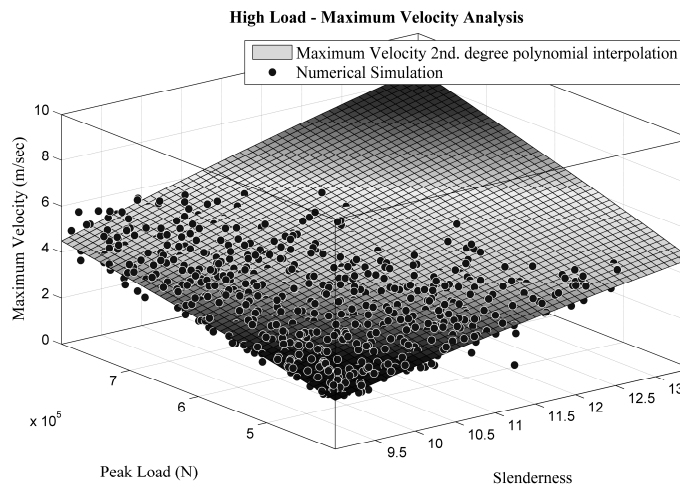
$$f(x, y) = p_0 + p_{10}x + p_{01}y + p_{20}x^2 + p_{11}xy + p_{02}y^2$$

P_0	P_{10}	P_{01}	P_{20}	P_{11}	P_{02}
4.021	0.6205	0.7622	-0.0169	0.0593	-0.0300

Goodness of fit:

SSE m^2/sec^2	R-square	Adjusted R-square:	RMSE m/sec
92.93	0.8499	0.8491	0.3166

Fig. 73:High Load, Max. Vel. –Peak Load - Slenderness 2nd deg. polyn. interpolation and goodness of fit.
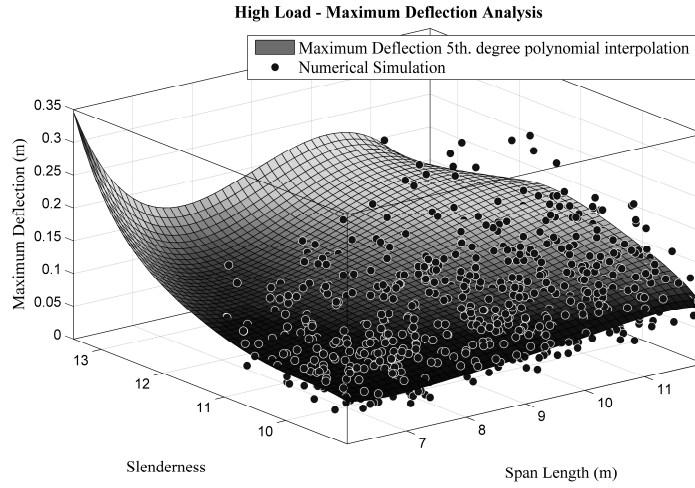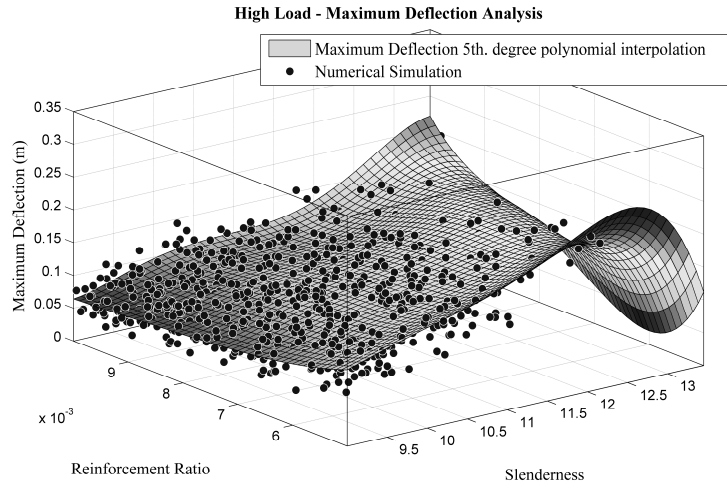
$$f(x,y) = p_0 + p_{10}x + p_{01}y + p_{20}x^2 + p_{11}xy + p_{02}y^2 + p_{30}x^3 + p_{21}x^2y + p_{12}xy^2 + p_{03}y^3$$

P_0	P_{10}	P_{01}	P_{20}	P_{11}	P_{02}	P_{30}	P_{21}	P_{12}	P_{03}
4.017	0.652	0.791	-0.010	0.056	-0.035	0.0135	-0.030	-0.024	-0.008

Goodness of fit:

SSE m^2/sec^2	R-square	Adjusted R-square:	RMSE m/sec
92.5	0.8506	0.8492	0.3166

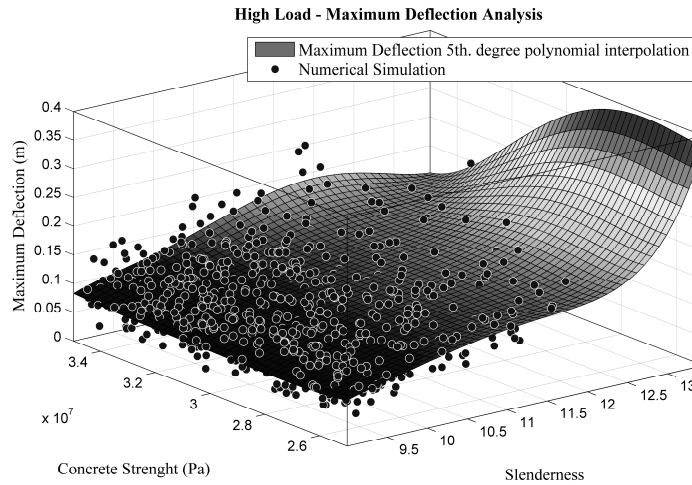Fig. 74: High Load, Max. Vel.-Peak Load - Slenderness 3rd deg. polyn. interp. and goodness of fit.

$$f(x,y) = p_0 + p_{10}x + p_{01}y + p_{20}x^2 + p_{11}xy + p_{02}y^2 + p_{30}x^3 + p_{21}x^2y + p_{12}xy^2 + p_{03}y^3 + p_{40}x^4 + p_{31}x^3y +$$
$$+ p_{22}x^2y^2 + p_{13}xy^3 + p_{04}y^4$$

P_0	P_{10}	P_{01}	P_{20}	P_{11}	P_{02}	P_{30}	P_{21}	P_{12}	P_{03}	P_{40}	P_{31}	P_{22}	P_{13}	P_{04}
4.018	0.6228	0.772	-0.024	0.059	-0.017	0.007	-0.025	-0.014	0.009	-0.001	0.016	0.0193	-0.008	-0.014

Goodness of fit:

SSE m^2/sec^2	R-square	Adjusted R-square:	RMSE m/sec
92.23	0.8511	0.8488	0.317

Fig. 75: High Load, Max. Vel. –Peak Load - Slenderness 4th deg. polyn. interpolation and goodness of fit.

$$f(x,y) = p_0 + p_{10}x + p_{01}y + p_{20}x^2 + p_{11}xy + p_{02}y^2 + p_{30}x^3 + p_{21}x^2y + p_{12}xy^2 + p_{03}y^3 + p_{40}x^4 + p_{31}x^3y +$$

$$+ p_{22}x^2y^2 + p_{13}xy^3 + p_{04}y^4 + p_{50}x^5 + p_{41}x^4y + p_{32}x^3y^2 + p_{23}x^2y^3 + p_{14}xy^4 + p_{05}y^5$$

P_0	P_{10}	P_{01}	P_{20}	P_{11}	P_{02}	P_{30}	P_{21}	P_{12}	P_{03}	P_{40}	P_{31}	P_{22}	P_{13}	P_{04}	P_{50}	P_{41}	P_{32}	P_{23}	P_{14}	P_{05}
3.991	0.599	0.769	0.055	0.084	0.020	0.033	0.016	-0.013	-0.005	-0.038	0.003	0.010	-0.016	0.033	0.005	-0.008	-0.011	-0.018	0.000	0.009

Goodness of fit:

SSE m^2/sec^2	R-square	Adjusted R-square:	RMSE m/sec
91.67	0.852	0.8487	0.317

Fig. 76: High Load, Max. Vel. – Peak Load - Slenderness 5th polyn. interp. and goodness of fit.

$$f(x,y) = p_0 + p_{10}x + p_{01}y$$

P_0	P_{10}	P_{01}
3.952	0.3128	-0.0298

Goodness of fit:

SSE m^2/sec^2	R-square	Adjusted R-square:	RMSE m/sec
529.3	0.1453	0.1434	0.7544

Fig. 77: High Load, Max. Vel. – Span - Slenderness 1st polyn. interp. and goodness of fit.
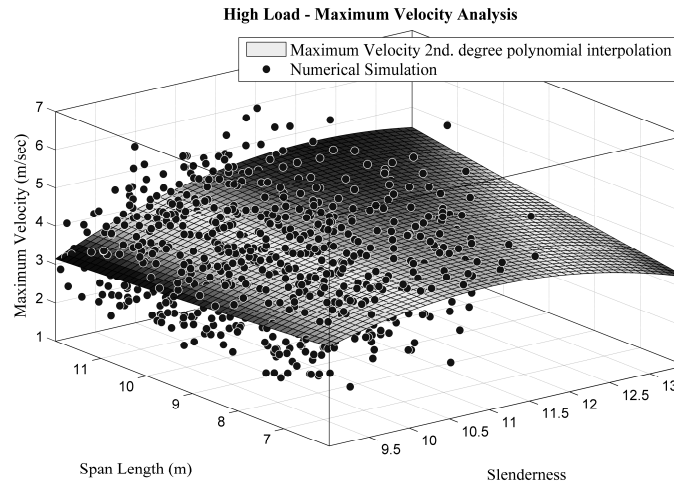
$$f(x, y) = p_0 + p_{10}x + p_{01}y + p_{20}x^2 + p_{11}xy + p_{02}y^2$$

P_0	P_{10}	P_{01}	P_{20}	P_{11}	P_{02}
4.031	0.3804	-0.023	-0.0914	0.072	0.0034

Goodness of fit:

SSE m^2/sec^2	R-square	Adjusted R-square:	RMSE m/sec
515.6	0.1674	0.1629	0.7458

Fig. 78:High Load, Max. Vel. –Span - Slenderness 2nd deg. polyn. interpolation and goodness of fit.

$$f(x, y) = p_0 + p_{10}x + p_{01}y + p_{20}x^2 + p_{11}xy + p_{02}y^2 + p_{30}x^3 + p_{21}x^2y + p_{12}xy^2 + p_{03}y^3$$

P_0	P_{10}	P_{01}	P_{20}	P_{11}	P_{02}	P_{30}	P_{21}	P_{12}	P_{03}
4.066	0.345	-0.062	-0.155	0.075	0.010	0.0322	-0.015	-0.014	0.029

Goodness of fit:

SSE m^2/sec^2	R-square	Adjusted R-square:	RMSE m/sec
512.4	0.1726	0.1646	0.7451

Fig. 79: High Load, Max Vel. -Span - Slenderness 3rd deg. polyn. interp. and goodness of fit.

$$f(x, y) = p_0 + p_{10}x + p_{01}y + p_{20}x^2 + p_{11}xy + p_{02}y^2 + p_{30}x^3 + p_{21}x^2 y + p_{12}xy^2 + p_{03}y^3 + p_{40}x^4 + p_{31}x^3 y + $$
$$+ p_{22}x^2 y^2 + p_{13}xy^3 + p_{04}y^4$$

P_0	P_{10}	P_{01}	P_{20}	P_{11}	P_{02}	P_{30}	P_{21}	P_{12}	P_{03}	P_{40}	P_{31}	P_{22}	P_{13}	P_{04}
4.076	0.287	-0.088	-0.165	0.069	0.008	0.065	0.0163	-0.005	0.034	-0.006	-0.016	-0.002	0.0168	0.007

Goodness of fit:

SSE m^2/sec^2	R-square	Adjusted R-square:	RMSE m/sec
510.8	0.1752	0.1626	0.7459

Fig. 80: High Load, Max. Vel. –Span - Slenderness 4th deg. polyn. interp. and goodness of fit.

$$f(x, y) = p_0 + p_{10}x + p_{01}y + p_{20}x^2 + p_{11}xy + p_{02}y^2 + p_{30}x^3 + p_{21}x^2 y + p_{12}xy^2 + p_{03}y^3 + p_{40}x^4 + p_{31}x^3 y + $$
$$+ p_{22}x^2 y^2 + p_{13}xy^3 + p_{04}y^4 + p_{50}x^5 + p_{41}x^4 y + p_{32}x^3 y^2 + p_{23}x^2 y^3 + p_{14}xy^4 + p_{05}y^5$$

P_0	P_{10}	P_{01}	P_{20}	P_{11}	P_{02}	P_{30}	P_{21}	P_{12}	P_{03}	P_{40}	P_{31}	P_{22}	P_{13}	P_{04}	P_{50}	P_{41}	P_{32}	P_{23}	P_{14}	P_{05}
4.062	0.235	-0.255	-0.134	0.116	0.022	0.101	0.051	0.022	0.249	-0.024	-0.065	0.009	0.024	-0.012	0.001	0.017	-0.008	-0.032	-0.003	-0.054

Goodness of fit:

SSE m^2/sec^2	R-square	Adjusted R-square:	RMSE m/sec
508.1	0.1795	0.1615	0.7464

Fig. 81: High Load, Max. Vel. – Span - Slenderness 5th polyn. interp. and goodness of fit.
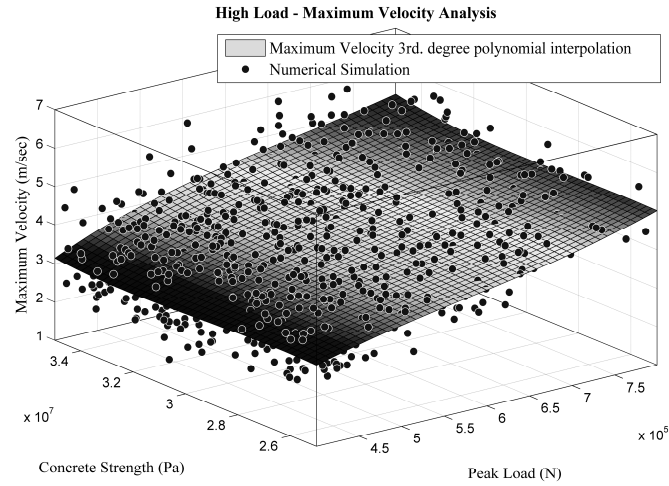
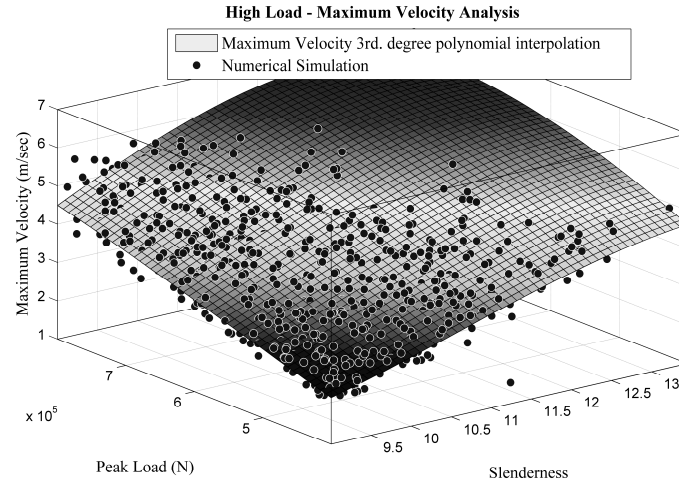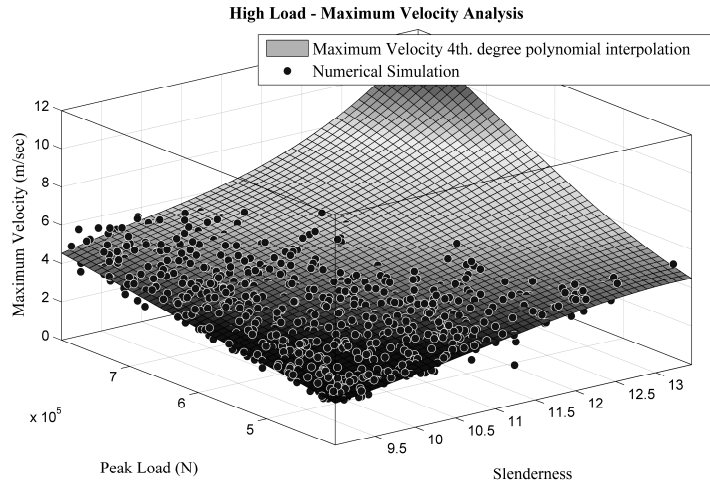$$f(x, y) = p_0 + p_{10}x + p_{01}y + p_{20}x^2 + p_{11}xy + p_{02}y^2 + p_{30}x^3 + p_{21}x^2y + p_{12}xy^2 + p_{03}y^3$$

P_0	P_{10}	P_{01}	P_{20}	P_{11}	P_{02}	P_{30}	P_{21}	P_{12}	P_{03}
3.977	0.476	0.053	-0.069	0.037	0.034	0.031	-0.025	0.009	0.023

Goodness of fit:

SSE m²/sec²	R-square	Adjusted R-square:	RMSE m/sec
357.7	0.4225	0.4168	0.6225

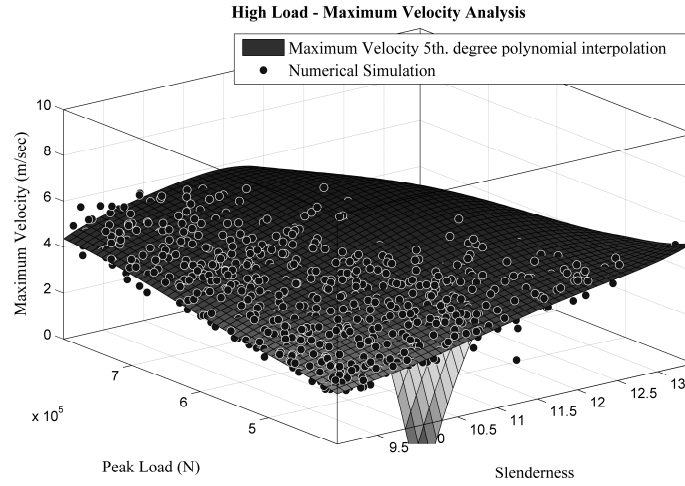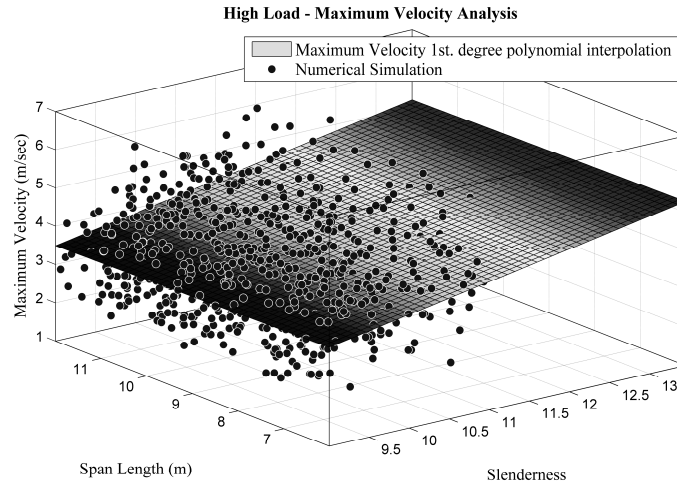Fig. 82: High Load, Max Vel. –Conc. Strength – Peak Load 3rd deg. polyn.interp. and goodness of fit.
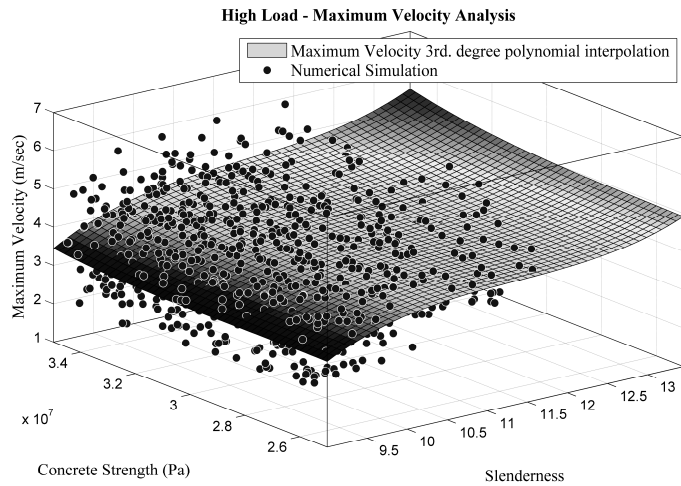
$$f(x, y) = p_0 + p_{10}x + p_{01}y + p_{20}x^2 + p_{11}xy + p_{02}y^2 + p_{30}x^3 + p_{21}x^2y + p_{12}xy^2 + p_{03}y^3$$

P_0	P_{10}	P_{01}	P_{20}	P_{11}	P_{02}	P_{30}	P_{21}	P_{12}	P_{03}
4.028	0.335	0.052	-0.142	0.022	0.042	0.027	0.004	0.000	0.011

Goodness of fit:

SSE m²/sec²	R-square	Adjusted R-square:	RMSE m/sec
511.3	0.1744	0.1664	0.7442

Fig. 83: High Load, Max Vel. –Conc. Strength – Slenderness 3rd deg. polyn. interp.and goodness of fit.

x – y	Fit type	SSE m^2	R-SQUARE	AR-SQUARE	RMSE m	Coefficients
Slend.-P.Load	poly55	0.58467087	0.796950663	0.794757906	0.017767865	21
Slend.-P.Load	poly44	0.591579941	0.794551224	0.793003171	0.017843657	15
Slend.-P.Load	poly33	0.59624080	0.792932562	0.791932236	0.017889756	10
Slend.-P.Load	poly22	0.601406477	0.791138583	0.790579233	0.017947828	6
Slend.-P.Load	poly11	0.75360261	0.738282651	0.738002739	0.020074761	3
Slend.-Span	poly55	1.249337712	0.566119663	0.561434130	0.02597284	21
Slend.-Span	poly44	1.255508783	0.563976523	0.560691093	0.025994832	15
Slend.-Span	poly33	1.264076134	0.561001182	0.558880415	0.026048348	10
Slend.-Span	poly22	1.265849822	0.560385201	0.559207872	0.026038678	6
Slend.-Span	poly11	1.327557523	0.53895484	0.538461744	0.026644395	3
P.Load-R.Ratio	poly11	2.128770294	0.260703041	0.259912349	0.033739885	3
C.Streng.-P.Load	poly11	2.351506343	0.183349423	0.182476000	0.035461106	3

Table 20 : Goodness of fit for low-load maximum deflection results .

Fig. 84 - Fig. 95 show goodness of fit in the case of low load, as concerns maximum displacement. A synthesis of this analysis is shown in Table 20, where the lowest SSE is obtained by a 5th degree polynomial function of slenderness and peak load (see Fig. 88). This function also presents the best AR-square index. These results underline the importance of peak load and slenderness in the estimation of beam response under blast load. The influence of other structural variables like concrete strength (see Fig. 94) and reinforcement ratio (see Fig. 95) does not seem to be significant.
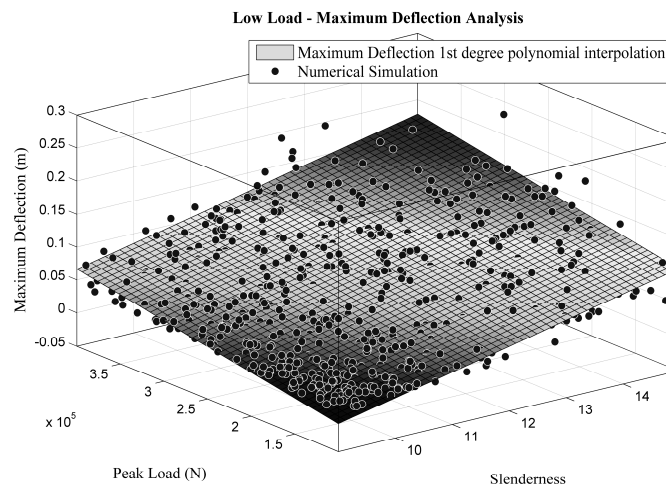
$$f(x, y) = p_0 + p_{10}x + p_{01}y$$

P$_0$	P$_{10}$	P$_{01}$
0.0699	0.029	0.021

Goodness of fit:

SSE m^2	R-square	Adjusted R-square:	RMSE m
0.7536	0.7383	0.738	0.02007

Fig. 84: Low Load, Max. Defl. – Peak Load-Slenderness 1st polyn. interp. and goodness of fit.
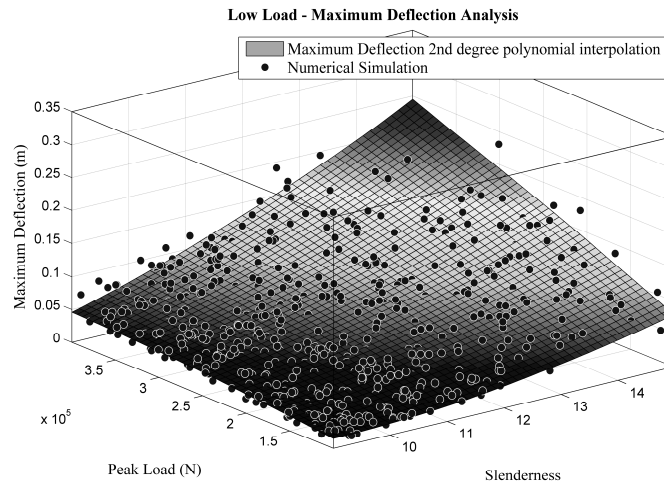
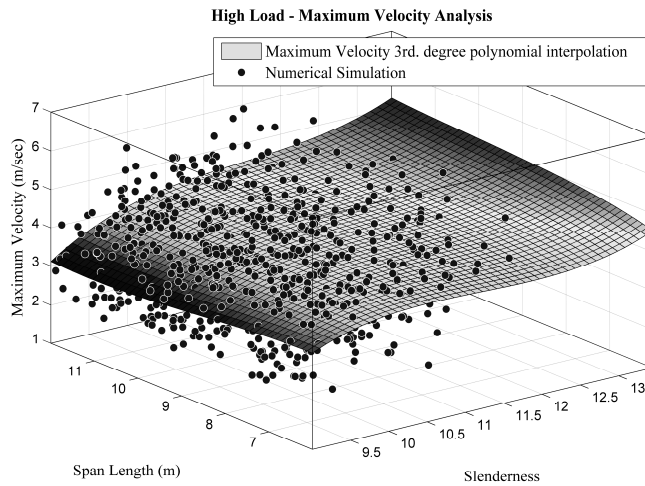$$f(x, y) = p_0 + p_{10}x + p_{01}y + p_{20}x^2 + p_{11}xy + p_{02}y^2$$

P_0	P_{10}	P_{01}	P_{20}	P_{11}	P_{02}
0.068	0.0301	0.0233	0.004	0.010	-0.001

Goodness of fit:

SSE m^2	R-square	Adjusted R-square:	RMSE m
0.6014	0.7911	0.7906	0.01795

Fig. 85: Low Load, Maximum Defl. – Peak Load-Slenderness 2nd deg. polyn. interpolation and goodness of fit.
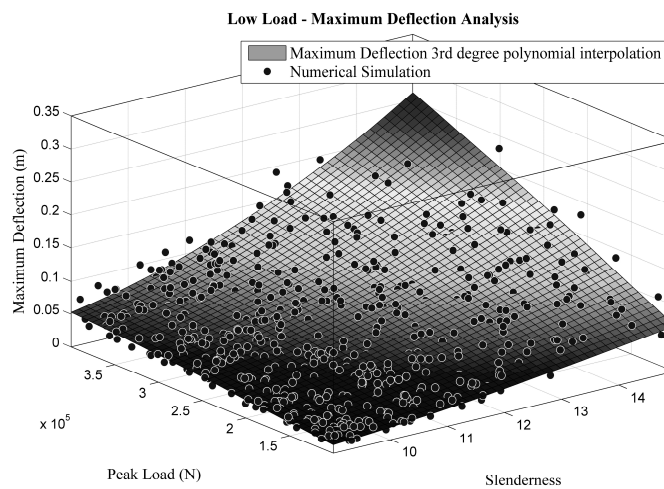
$$f(x, y) = p_0 + p_{10}x + p_{01}y + p_{20}x^2 + p_{11}xy + p_{02}y^2 + p_{30}x^3 + p_{21}x^2y + p_{12}xy^2 + p_{03}y^3$$

P_0	P_{10}	P_{01}	P_{20}	P_{11}	P_{02}	P_{30}	P_{21}	P_{12}	P_{03}
0.068	0.031	0.022	0.005	0.010	-0.001	0.000	0.002	0.000	0.000

Goodness of fit:

SSE m^2	R-square	Adjusted R-square:	RMSE m
0.5962	0.7929	0.7919	0.01789

Fig. 86: Low Load, Max. Def.- Peak Load - Span-Slenderness 3rd deg. polyn. interp. and goodness of fit.

$$f(x,y) = p_0 + p_{10}x + p_{01}y + p_{20}x^2 + p_{11}xy + p_{02}y^2 + p_{30}x^3 + p_{21}x^2y + p_{12}xy^2 + p_{03}y^3 + p_{40}x^4 + p_{31}x^3y +$$
$$+ p_{22}x^2y^2 + p_{13}xy^3 + p_{04}y^4$$

P_0	P_{10}	P_{01}	P_{20}	P_{11}	P_{02}	P_{30}	P_{21}	P_{12}	P_{03}	P_{40}	P_{31}	P_{22}	P_{13}	P_{04}
0.068	0.028	0.022	0.006	0.008	-0.003	0.002	0.001	0.000	0.000	-0.001	0.001	0.001	0.000	0.001

Goodness of fit:

SSE m^2	R-square	Adjusted R-square:	RMSE m
0.5916	0.7946	0.793	0.01784

Fig. 87: Low Load, Max. Defl. – Peak Load-Slend. 4th deg. polyn. interpolation and goodness of fit.

$$f(x,y) = p_0 + p_{10}x + p_{01}y + p_{20}x^2 + p_{11}xy + p_{02}y^2 + p_{30}x^3 + p_{21}x^2y + p_{12}xy^2 + p_{03}y^3 + p_{40}x^4 + p_{31}x^3y +$$
$$+ p_{22}x^2y^2 + p_{13}xy^3 + p_{04}y^4 + p_{50}x^5 + p_{41}x^4y + p_{32}x^3y^2 + p_{23}x^2y^3 + p_{14}xy^4 + p_{05}y^5$$

P_0	P_{10}	P_{01}	P_{20}	P_{11}	P_{02}	P_{30}	P_{21}	P_{12}	P_{03}	P_{40}	P_{31}	P_{22}	P_{13}	P_{04}	P_{50}	P_{41}	P_{32}	P_{23}	P_{14}	P_{05}
0.069	0.029	0.020	0.002	0.005	-0.004	0.004	0.002	-0.006	0.001	0.001	0.002	0.001	0.001	0.001	-0.001	-0.000	0.002	0.000	0.001	-0.000

Goodness of fit:

SSE m^2	R-square	Adjusted R-square:	RMSE m
0.5847	0.797	0.7948	0.01777

Fig. 88: Low Load, Maximum Defl. - Load-Slenderness 5th polyn. interpolation and goodness of fit.
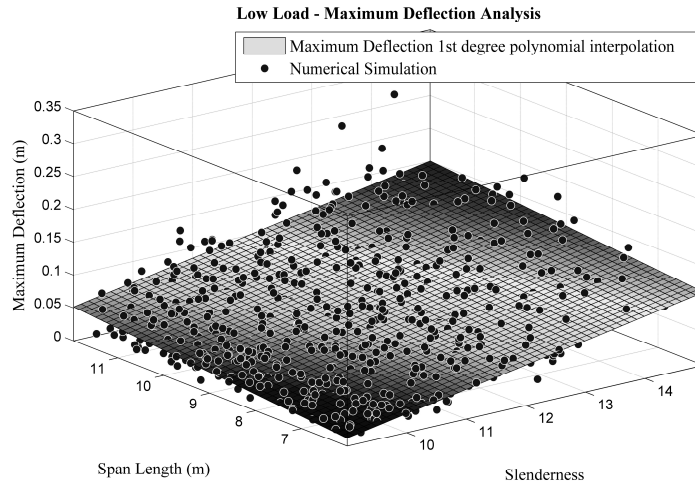
$$f(x, y) = p_0 + p_{10}x + p_{01}y$$

P_0	P_{10}	P_{01}
0.070	0.026	0.011

Goodness of fit:

SSE m^2	R-square	Adjusted R-square:	RMSE m
1.328	0.539	0.5385	0.02664

Fig. 89: Low Load, Maximum Defl. - Span-Slenderness 1st polyn. interpolation and goodness of fit.
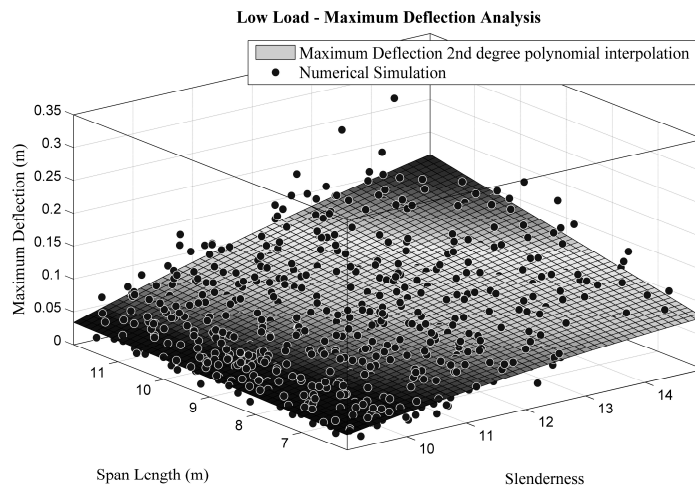
$$f(x, y) = p_0 + p_{10}x + p_{01}y + p_{20}x^2 + p_{11}xy + p_{02}y^2$$

P_0	P_{10}	P_{01}	P_{20}	P_{11}	P_{02}
0.072	0.027	0.011	-0.002	0.006	-0.000

Goodness of fit:

SSE m^2	R-square	Adjusted R-square:	RMSE m
1.266	0.5604	0.5592	0.02604

Fig. 90: Low Load, Maximum Defl. - Span-Slenderness 2nd deg. polyn. interpolation and goodness of fit.
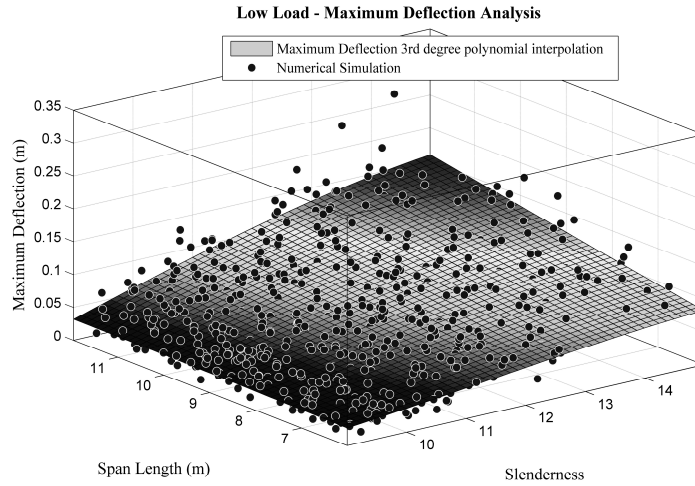
$$f(x, y) = p_0 + p_{10}x + p_{01}y + p_{20}x^2 + p_{11}xy + p_{02}y^2 + p_{30}x^3 + p_{21}x^2y + p_{12}xy^2 + p_{03}y^3$$

P_0	P_{10}	P_{01}	P_{20}	P_{11}	P_{02}	P_{30}	P_{21}	P_{12}	P_{03}
0.0715	0.0278	0.012	-0.0014	0.0060	-0.0001	0.0001	0.0008	0.000	0.000

Goodness of fit:

SSE m^2	R-square	Adjusted R-square:	RMSE m
1.264	0.561	0.5589	0.02605

Fig. 91: Low Load, Maximum Defl. - Span-Slenderness 3rd deg. polyn. interpolation and goodness of fit.

$$f(x, y) = p_0 + p_{10}x + p_{01}y + p_{20}x^2 + p_{11}xy + p_{02}y^2 + p_{30}x^3 + p_{21}x^2y + p_{12}xy^2 + p_{03}y^3 + p_{40}x^4 + p_{31}x^3y +$$
$$+ p_{22}x^2y^2 + p_{13}xy^3 + p_{04}y^4$$

P_0	P_{10}	P_{01}	P_{20}	P_{11}	P_{02}	P_{30}	P_{21}	P_{12}	P_{03}	P_{40}	P_{31}	P_{22}	P_{13}	P_{04}
0.072	0.028	0.011	-0.002	0.012	-0.002	-0.001	0.001	0.000	0.000	0.000	-0.001	0.000	-0.001	0.001

Goodness of fit:

SSE m^2	R-square	Adjusted R-square:	RMSE m
1.256	0.564	0.5607	0.02599

Fig. 92: Low Load, Maximum Defl. - Span-Slenderness 4th deg. polyn. interpolation and goodness of fit.
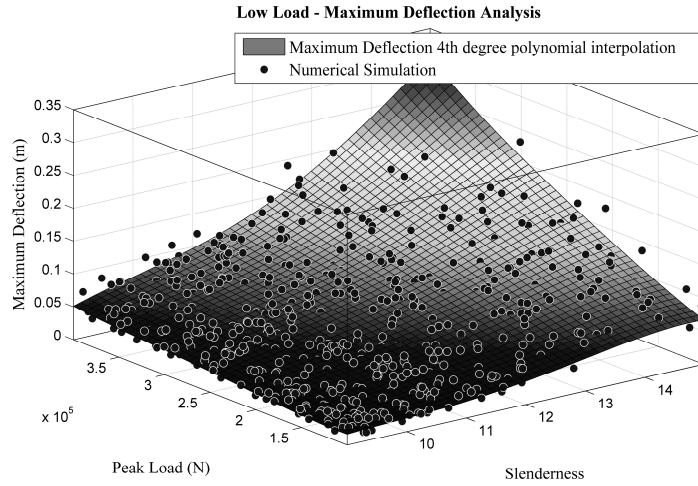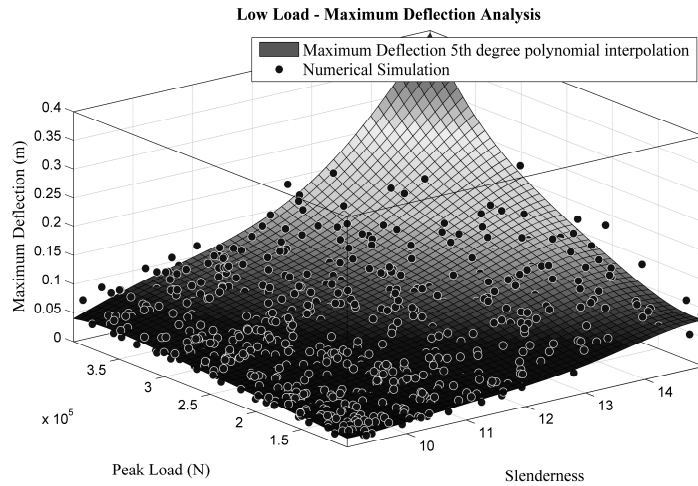
$$f(x, y) = p_0 + p_{10}x + p_{01}y + p_{20}x^2 + p_{11}xy + p_{02}y^2 + p_{30}x^3 + p_{21}x^2y + p_{12}xy^2 + p_{03}y^3 + p_{40}x^4 + p_{31}x^3y +$$

$$+ p_{22}x^2y^2 + p_{13}xy^3 + p_{04}y^4 + p_{50}x^5 + p_{41}x^4y + p_{32}x^3y^2 + p_{23}x^2y^3 + p_{14}xy^4 + p_{05}y^5$$

P_0	P_{10}	P_{01}	P_{20}	P_{11}	P_{02}	P_{30}	P_{21}	P_{12}	P_{03}	P_{40}	P_{31}	P_{22}	P_{13}	P_{04}	P_{50}	P_{41}	P_{32}	P_{23}	P_{14}	P_{05}
0.073	0.008	0.026	-0.002	0.009	-0.008	0.001	0.001	0.005	0.002	0.001	0.000	0.000	0.000	0.004	-0.001	-0.000	0.000	0.000	-0.001	-0.001

Goodness of fit:

SSE m^2	R-square	Adjusted R-square:	RMSE m
1.249	0.5661	0.5614	0.02597

Fig. 93: Low Load, Max. Defl. - Span-Slenderness 5th deg. polyn. interpolation and goodness of fit.
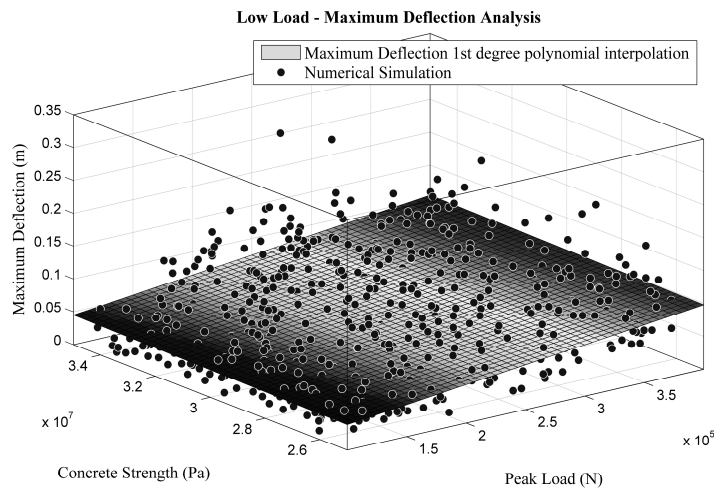
$$f(x, y) = p_0 + p_{10}x + p_{01}y$$

P_0	P_{10}	P_{01}
0.002	0.000	0.000

Goodness of fit:

SSE m^2	R-square	Adjusted R-square:	RMSE m
2.352	0.1833	0.1825	0.03546

Fig. 94: Low Load, Max. Defl. – C. Str.gth- Peak Load 1st deg. polyn. interp. and goodness of fit.

Low Load - Maximum Deflection Analysis
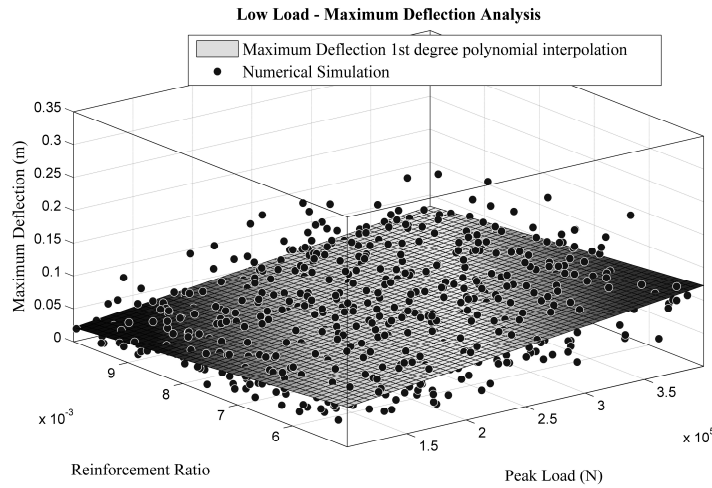
$$f(x, y) = p_0 + p_{10}x + p_{01}y$$

P_0	P_{10}	P_{01}
0.079	0.000	-7.866

Goodness of fit:

SSE m^2	R-square	Adjusted R-square:	RMSE m
2.129	0.2607	0.2599	0.03374

Fig. 95: Low Load, Max. Defl. – R. Ratio- Peak Load 1st deg. polyn. interpol. and goodness of fit.

x – y	Fit type	SSE m^2/sec^2	R-SQUARE	AR-SQUARE	RMSE m/sec	Coefficients
Slend.-P.Load	poly55	74.15608153	0.951244314	0.950717795	0.200102675	21
Slend.-P.Load	poly44	74.91211988	0.950747238	0.95037612	0.200795136	15
Slend.-P.Load	poly33	75.21087461	0.950550815	0.95031193	0.200924961	10
Slend.-P.Load	poly22	75.41919317	0.950413851	0.950281055	0.200987377	6
Slend.-P.Load	poly11	132.1395093	0.913121725	0.913028807	0.265824828	3
Slend.-Span	poly55	1026.960884	0.324800050	0.317508474	0.744657315	21
Slend.-Span	poly44	1031.492396	0.321820699	0.316710629	0.745092446	15
Slend.-Span	poly33	1038.129148	0.317457208	0.314159900	0.746481871	10
Slend.-Span	poly22	1038.440420	0.317252555	0.315424094	0.745793567	6
R.Ratio-Slend.	poly11	1054.338630	0.306799897	0.306058507	0.750877786	3
Slend.-Span	poly11	1073.179019	0.294412834	0.293658195	0.757556944	3
C.Stren.-Slend.	poly11	1076.444277	0.292266012	0.291509077	0.758708542	3

Table 21 : Goodness of fit for low-load maximum velocity results .

Fig. 96- Fig. 107 represents goodness of fit in the case of low load, as concerns maximum velocity. A synthesis of this analysis is shown in Table 21, where the lowest SSE is obtained by a 5th degree polynomial function of slenderness and peak load (see Fig. 100). The same function obtains the best AR-square index. From these results, it is clear that the most important parameters for fitting maximum velocity/low load results are peak load and slenderness. Other variables obtained dramatically worse results. Actually, a simple linear function of peak load and slenderness (see Fig. 96) fits the numerical results better than more sophisticated functions of other variables (i.e. the 5th degree polynomial corresponding to slenderness and span length, see Fig. 105).
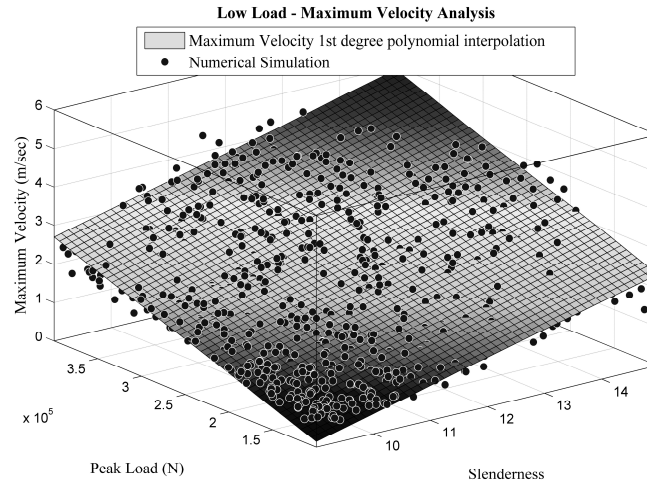
$$f(x, y) = p_0 + p_{10}x + p_{01}y$$

P_0	P_{10}	P_{01}
2.201	0.589	0.718

Goodness of fit:

SSE m^2/sec^2	R-square	Adjusted R-square:	RMSE m/sec
132.1	0.9131	0.913	0.2658

Fig. 96: Low Load, Max. Vel.. – Peak Load - Slenderness 1st deg. polyn. interpol. and goodness of fit.
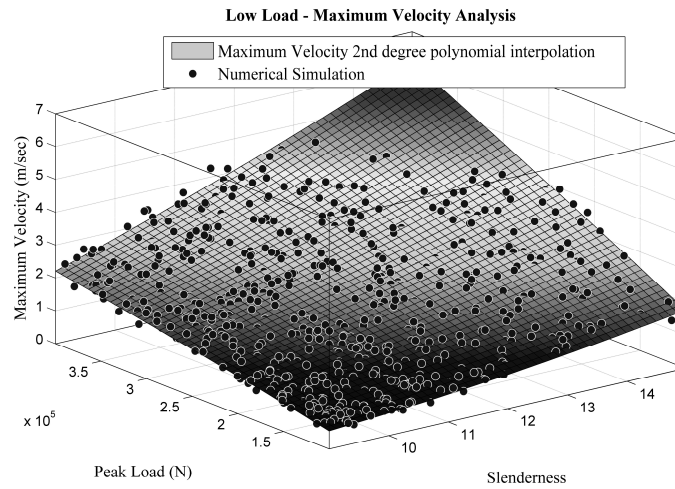
$$f(x, y) = p_0 + p_{10}x + p_{01}y + p_{20}x^2 + p_{11}xy + p_{02}y^2$$

P_0	P_{10}	P_{01}	P_{20}	P_{11}	P_{02}
2.211	0.623	0.758	0.035	0.199	-0.016

Goodness of fit:

SSE m^2/sec^2	R-square	Adjusted R-square:	RMSE m/sec
75.42	0.9504	0.9503	0.201

Fig. 97: Low Load, Maximum Vel. – Peak Load-Slenderness 2nd deg. polyn. interpolation and goodness of fit.
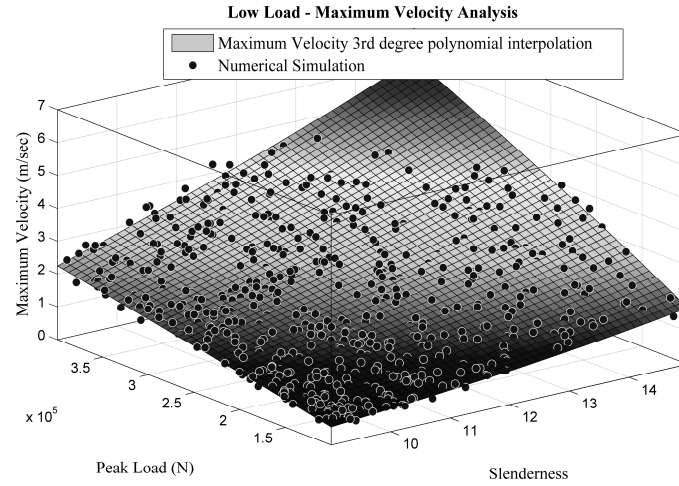
$$f(x, y) = p_0 + p_{10}x + p_{01}y + p_{20}x^2 + p_{11}xy + p_{02}y^2 + p_{30}x^3 + p_{21}x^2y + p_{12}xy^2 + p_{03}y^3$$

P_0	P_{10}	P_{01}	P_{20}	P_{11}	P_{02}	P_{30}	P_{21}	P_{12}	P_{03}
2.214	0.624	0.749	0.029	0.197	-0.018	0.004	0.002	-0.009	0.003

Goodness of fit:

SSE m^2/sec^2	R-square	Adjusted R-square:	RMSE m/sec
75.21	0.9506	0.9503	0.2009

Fig. 98: Low Load, Maximum Vel. - Peak Load -Slenderness 3rd deg. polyn. interpolation and goodness of fit.
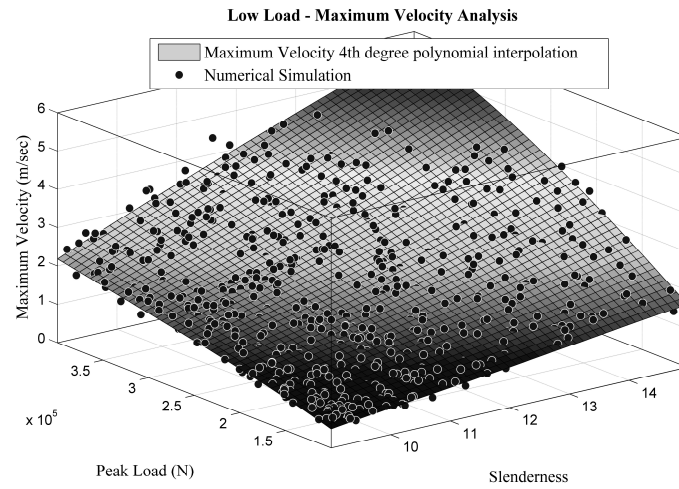
$$f(x, y) = p_0 + p_{10}x + p_{01}y + p_{20}x^2 + p_{11}xy + p_{02}y^2 + p_{30}x^3 + p_{21}x^2y + p_{12}xy^2 + p_{03}y^3 + p_{40}x^4 + p_{31}x^3y +$$
$$+ p_{22}x^2y^2 + p_{13}xy^3 + p_{04}y^4$$

P_0	P_{10}	P_{01}	P_{20}	P_{11}	P_{02}	P_{30}	P_{21}	P_{12}	P_{03}	P_{40}	P_{31}	P_{22}	P_{13}	P_{04}
2.198	0.619	0.759	0.052	0.204	-0.001	0.006	-0.006	-0.008	-0.002	-0.003	0.000	-0.017	0.008	-0.001

Goodness of fit:

SSE m^2/sec^2	R-square	Adjusted R-square:	RMSE m/sec
74.91	0.9507	0.9504	0.2008

Fig. 99: Low Load, Max. Vel. - Peak Load -Slenderness 4th deg. polyn. interp. and goodness of fit.

$$f(x, y) = p_0 + p_{10}x + p_{01}y + p_{20}x^2 + p_{11}xy + p_{02}y^2 + p_{30}x^3 + p_{21}x^2y + p_{12}xy^2 + p_{03}y^3 + p_{40}x^4 + p_{31}x^3y +$$

$$+ p_{22}x^2y^2 + p_{13}xy^3 + p_{04}y^4 + p_{50}x^5 + p_{41}x^4y + p_{32}x^3y^2 + p_{23}x^2y^3 + p_{14}xy^4 + p_{05}y^5$$

P_0	P_{10}	P_{01}	P_{20}	P_{11}	P_{02}	P_{30}	P_{21}	P_{12}	P_{03}	P_{40}	P_{31}	P_{22}	P_{13}	P_{04}	P_{50}	P_{41}	P_{32}	P_{23}	P_{14}	P_{05}
2.208	0.587	0.729	-0.003	0.215	0.009	0.052	0.036	0.012	0.016	0.025	-0.001	-0.021	-0.009	-0.006	-0.016	-0.001	-0.010	-0.025	-0.006	0.000

Goodness of fit:

SSE m^2/sec^2	R-square	Adjusted R-square:	RMSE m/sec
74.16	0.9512	0.9507	0.2001

Fig. 100: Low Load, Max. Vel. - Peak Load -Slenderness 5th deg. polyn. interp. and goodness of fit.

$$f(x, y) = p_0 + p_{10}x + p_{01}y$$

P_0	P_{10}	P_{01}
2.201	0.489	-0.045

Goodness of fit:

SSE m^2/sec^2	R-square	Adjusted R-square:	RMSE m/sec
1073	0.2944	0.2937	0.7576

Fig. 101: Low Load, Max. Vel.. – Span - Slenderness 1st deg. polyn. interpol. and goodness of fit.
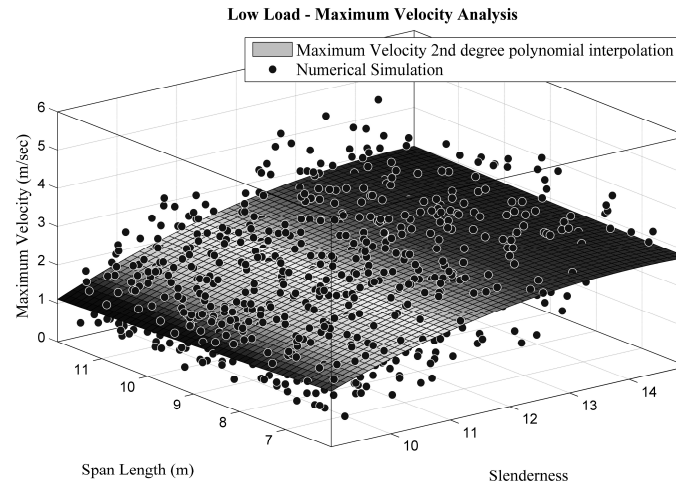
$$f(x, y) = p_0 + p_{10}x + p_{01}y + p_{20}x^2 + p_{11}xy + p_{02}y^2$$

P_0	P_{10}	P_{01}	P_{20}	P_{11}	P_{02}
2.324	0.553	-0.043	-0.131	0.037	0.005

Goodness of fit:

SSE m^2/sec^2	R-square	Adjusted R-square:	RMSE m/sec
1038	0.3173	0.3154	0.7458

Fig. 102: Low Load, Max. Vel. – Span-Slenderness 2nd deg. polyn. interpolation and goodness of fit.
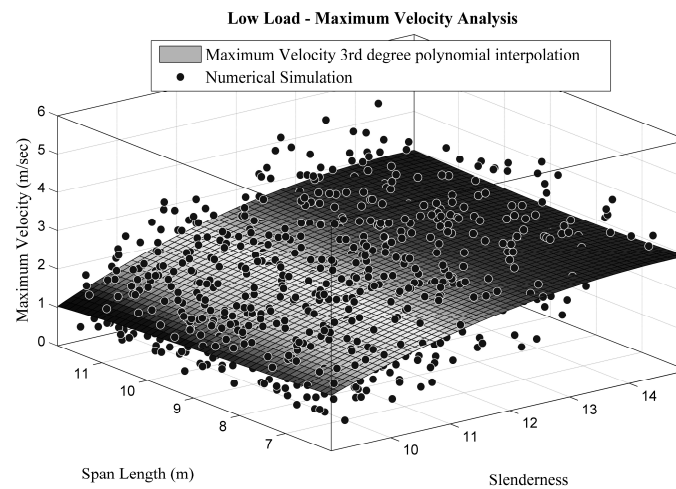
$$f(x, y) = p_0 + p_{10}x + p_{01}y + p_{20}x^2 + p_{11}xy + p_{02}y^2 + p_{30}x^3 + p_{21}x^2y + p_{12}xy^2 + p_{03}y^3$$

P_0	P_{10}	P_{01}	P_{20}	P_{11}	P_{02}	P_{30}	P_{21}	P_{12}	P_{03}
2.325	0.542	-0.028	-0.131	0.041	0.005	-0.000	-0.008	0.013	-0.005

Goodness of fit:

SSE m^2/sec^2	R-square	Adjusted R-square:	RMSE m/sec
1038	0.3175	0.3142	0.7465

Fig. 103: Low Load, Max. Vel. - Span –Slend. 3rd deg. polyn. interpolation and goodness of fit.

$$f(x,y) = p_0 + p_{10}x + p_{01}y + p_{20}x^2 + p_{11}xy + p_{02}y^2 + p_{30}x^3 + p_{21}x^2y + p_{12}xy^2 + p_{03}y^3 + p_{40}x^4 + p_{31}x^3y +$$
$$+ p_{22}x^2y^2 + p_{13}xy^3 + p_{04}y^4$$

P_0	P_{10}	P_{01}	P_{20}	P_{11}	P_{02}	P_{30}	P_{21}	P_{12}	P_{03}	P_{40}	P_{31}	P_{22}	P_{13}	P_{04}
2.369	0.591	-0.058	-0.191	0.172	-0.099	-0.042	0.022	0.009	0.009	0.029	-0.034	-0.001	-0.042	0.0426

Goodness of fit:

SSE m^2/sec^2	R-square	Adjusted R-square:	RMSE m/sec
1031	0.3218	0.3167	0.7451

Fig. 104: Low Load, Max. Vel. – Span - Slenderness 4th deg. polyn. interp. and goodness of fit.
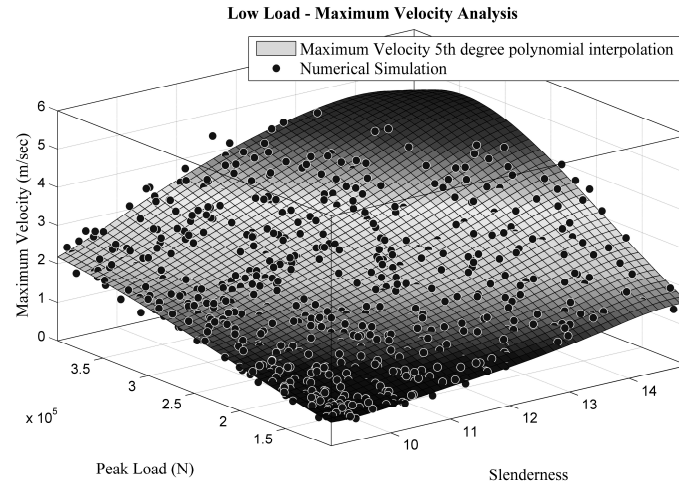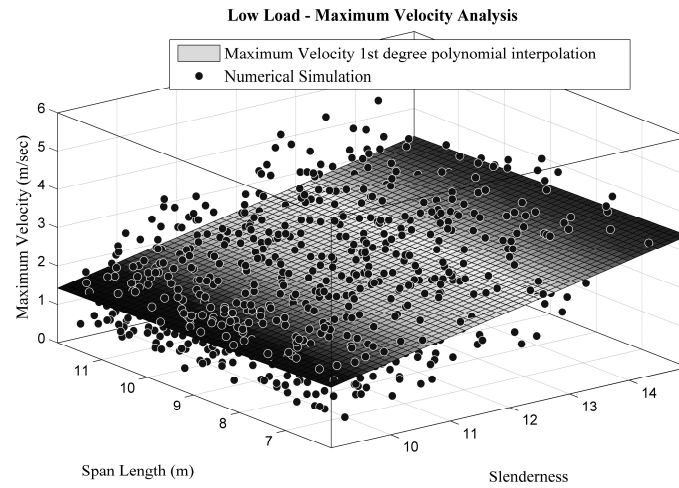

$$f(x,y) = p_0 + p_{10}x + p_{01}y + p_{20}x^2 + p_{11}xy + p_{02}y^2 + p_{30}x^3 + p_{21}x^2y + p_{12}xy^2 + p_{03}y^3 + p_{40}x^4 + p_{31}x^3y +$$
$$+ p_{22}x^2y^2 + p_{13}xy^3 + p_{04}y^4 + p_{50}x^5 + p_{41}x^4y + p_{32}x^3y^2 + p_{23}x^2y^3 + p_{14}xy^4 + p_{05}y^5$$

P_0	P_{10}	P_{01}	P_{20}	P_{11}	P_{02}	P_{30}	P_{21}	P_{12}	P_{03}	P_{40}	P_{31}	P_{22}	P_{13}	P_{04}	P_{50}	P_{41}	P_{32}	P_{23}	P_{14}	P_{05}
2.381	0.553	-0.183	-0.269	0.075	-0.084	0.01	0.163	0.033	0.115	0.072	0.028	-0.009	-0.029	0.036	-0.022	-0.043	0.007	-0.024	-0.012	-0.024

Goodness of fit:

SSE m^2/sec^2	R-square	Adjusted R-square:	RMSE m/sec
1027	0.3248	0.3175	0.7447

Fig. 105: Low Load, Max. Vel. – Span - Slenderness 5th deg. polyn. interp. and goodness of fit.
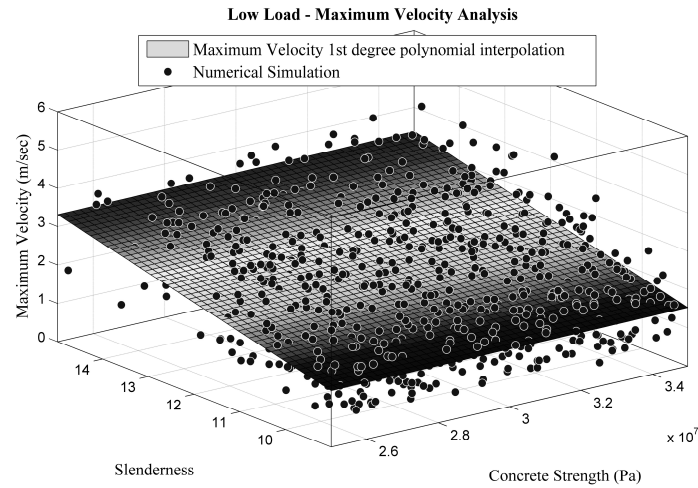
$$f(x, y) = p_0 + p_{10}x + p_{01}y$$

P_0	P_{10}	P_{01}
-1.455	0.000	0.3084

Goodness of fit:

SSE m^2/sec^2	R-square	Adjusted R-square:	RMSE m/sec
1076	0.2923	0.2915	0.7587

Fig. 106: Low Load, Max. Vel.. –Slenderness – Concrete Strength 1st deg. polyn. interpol. and goodness of fit.
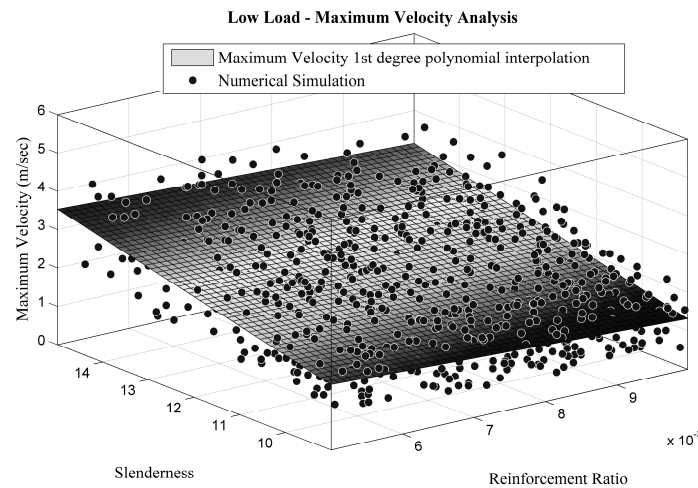
$$f(x, y) = p_0 + p_{10}x + p_{01}y$$

P_0	P_{10}	P_{01}
-0.659	-78.08	0.3059

Goodness of fit:

SSE m^2/sec^2	R-square	Adjusted R-square:	RMSE m/sec
1054	0.3068	0.3061	0.7509

Fig. 107: Low Load, Max. Vel.. –Slenderness – Reinforcement Ratio 1st deg. polyn. interpol. and goodness of fit.

3.2.3 Predictive tables

If the fitting functions, presented in the previous paragraph 3.2.2, were obtained with a sufficiently-high number of simulations they would correspond to the most probable response of the given beam under a given blast load. In order to have an idea of the useful development of this analysis Table 22 and Table 23 have been prepared. Referring to High Load (peak load 0.4-0.8 $\cdot 10^6$ N in Table 22) and Low load conditions (peak load 0.1-0.4 $\cdot 10^6$ N in Table 23) the most probable maximum displacements of a beam under the hypothesis[14] assumed in paragraph 3.1.1 are expressed. It is important to point out that, due to the limited number of numerical experiments (4000 runs of the SDOF model), only the linear polynomial function (poly1-1, see Table 18 and Table 20) of slenderness and peak load has been considered to prepare these tables. Actually, the limited number of the required parameters for a linear function and the significance of slenderness and peak load variables lead to this choice. In fact, more complex polynomial relationships with more coefficients would have required a larger number of numerical experiments to become significant.

Slenderness\Peak Load	$4 \cdot 10^5$ N	$5 \cdot 10^5$ N	$6 \cdot 10^5$ N	$7 \cdot 10^5$ N	$8 \cdot 10^5$ N
9	0.044	0.061	0.079	0.097	0.114
10	0.079	0.096	0.114	0.131	0.149
11	0.114	0.131	0.149	0.166	0.184
12	0.149	0.166	0.184	0.201	0.219
13	0.184	0.201	0.219	0.236	0.254
14	0.218	0.236	0.254	0.271	0.289
15	0.253	0.271	0.288	0.306	0.324

Table 22 : High Load – Maximum Displacement estimation (in meter) based on the poly 1-1 model Slenderness/Peak Load.

Hence, referring to Table 22 it is interesting to underline that the black thick line identifies the conditions in which the probability of collapse (attainment of the ultimate concrete strain) approaches and exceeds 50% in case of high load. This threshold of safety is never reached in case of low load.

In conclusion, a systematic application of the methodology presented in this chapter 3 could produce several useful tables like these two (Table 22 and Table 23). In this way a designer may quickly know what are the maximum displacement, the maximum velocity and the reliability measures (in terms of collapse probability) of a given type of beam under a given condition of the load.

Slenderness\Peak Load	$1 \cdot 10^5$ N	$1.5 \cdot 10^5$ N	$2 \cdot 10^5$ N	$3 \cdot 10^5$ N	$4 \cdot 10^5$ N
9	N.V.	0.005	0.017	0.042	0.066
10	0.011	0.023	0.036	0.060	0.085
11	0.030	0.042	0.054	0.079	0.104
12	0.048	0.061	0.073	0.098	0.123
13	0.067	0.080	0.092	0.117	0.141
14	0.086	0.098	0.111	0.135	0.160
15	0.105	0.117	0.129	0.154	0.179

Table 23 : Low Load – Maximum Displacement estimation (in meter) based on the poly 1-1 model Slenderness/Peak Load.

---

[14] Simple supported, uniformly distributed load with triangular time history etc.

SECTION 4:

CONCLUSIONS

The present thesis deals with the flexural failure of Reinforced Concrete beams under blast loads. The main aim was to develop theoretical dynamic and energy models capable of evaluating the dynamic response of R.C. under explosive load. For this reason various dynamic models were developed in Section 1 and a simple energy approach was presented in Section 2. In all the models the strain-rate sensitivity of both steel and concrete was taken into account, as well as other nonlinearities in structural behaviour. Models with different levels of complexity were presented, from the simplest Single Degree Of Freedom (SDOF) system to Continuous Beam and Finite Element models. The characteristics, advantages and disadvantages of each approach were stated and discussed. The theoretical results were compared with some experimental findings available in literature in order to demonstrate their excellent quality. The failure criterion was the same for all the models developed in the thesis and it corresponded to attainment of the maximum concrete strain.

In Chapter 1.2 the beam has been idealised as an equivalent SDOF system, as it is common in practical applications. This approach, in which strain-rate effects are accounted for, is more convenient than the others dynamic models from a computational point of view, but it presents two main drawbacks: the first is that it requires the use of approximate formulas to define some quantities (such as, for instance, the coefficients converting total beam mass into SDOF mass and the length of the plastic hinge); the second is that it cannot provide some useful information, like profiles of displacement, rotation and curvature along the beam at any instant in time. To sum up, the SDOF model is a very powerful tool for simple and quick calculations but it is less accurate than continuous beam models. In case of time consuming analysis it can be the best choice.

An alternative approach has been presented through Chapter 1.3, in which an Euler-Bernoulli continuous beam model has been described. The corresponding non-linear partial differential equation of motion is an innovative achievement obtained in this work. It is based on a smooth non-linear relationship between bending moment and curvature which represents a distributed plasticity along the beam. Thanks to this approach it is not necessary to distinguish one equation of motion for the elastic realm and one for the plastic realm. The only one equation is rather straightforward and easy to integrate (for example through the Finite Difference Method); nonetheless, it gives an

accurate estimation of the time-history of maximum beam displacement and, in particular, of its value at failure, as shown by comparing experimental data. The precision of the model also derives from having included in its formulation the effects of strain rate on materials mechanical properties.

In Chapter 1.4 a simple F.E. model has been presented, it was obtained by means of the commercial code *Midas Gen 2012 (v2.1).* In particular, the fibre model of this software has been used, consisting of dividing the cross-section of the beam into concrete fibres and steel rebars. In order to take into consideration the effects of strain rate, not accounted by the software, the dynamic properties of the material provided by the continuous beam model in the last step of the calculation (corresponding to the ultimate strain rates reached in the analysis of that model) were introduced into the FE model as constants. Displacement time-history provided by this approach was always less accurate than the other ones probably because of the lack of a consistent strain rate modelling.

In Section 2 the same problem faced in Section 1 is solved by means of a simple energy model. Starting from the balance of energy equation and assuming a mathematical function describing the deformed shape of the beam, it is possible to determine time-histories of displacement and curvature. Though quite simple from a computational point of view, this approach has produced excellent results regarding beam midspan deflections. It is less accurate as regards the distribution of displacement and curvature along the whole beam. It is important to underline that in this case as well, strain rate has been considered and the collapse criterion is the same as the one assumed in Section 1.

In the last part of the thesis (Section 3), a sensitivity analysis to determine the key parameters in beam response under blast load has been developed exploiting what has been achieved in the previous sections. Results of numerical simulations obtained by means of the SDOF model (presented in Section 1) in terms of deflection and velocity have been fitted by proper polynomial least-square interpolation. Random variations of beams and load characteristics produce several dynamic problems solved by means of the SDOF model presented in Chapter 1.2. Its short computational time was of fundamental importance in this analysis. Among the various interpolations considering several parameters (peak load, positive phase duration, slenderness, span length, concrete strength, reinforcement ratio etc) slenderness (corresponding to stiffness) and peak load prove to be the most important parameters, but span length (corresponding to mass) is also a key parameter. Other variables such as concrete strength and reinforcement ratio do not seem to have a high correlation with the results.

The latter approach can be very suitable for simple analysis in the case of blast-resistant structural design. Indeed, fitting functions obtained with a sufficiently-high number of simulations correspond to the most probable response of the real beam under a given condition of blast load. For this reason, systematic application of these procedures can yield suitable tables (like Table 22 and Table 23) where it is possible to find the most probable maximum deflection or maximum velocity of a beam with a given slenderness under a given blast load characterized by a given peak value.

Future developments of this thesis can be briefly outlined. Concerning the continuous beam model proposed in Section 1 the use of the Timoshenko's beam theory can take into account the rotational inertia and shear deformation (neglected in the Euler-Bernoulli model). In addition the hypothesis of small displacements and rotations assumed in Chapter 1.3 can be overcome by considering large

deformations.

Furthermore, regarding both the dynamic models presented in Section 1 and the energy model described in Section 2 a different failure criterion could be defined. Since the maximum displacement predicted by the proposed approach underestimates the actual value found experimentally, calculation of maximum deflection could be carried out after the first concrete fibre reaches maximum strain (representing the collapse criterion considered in the thesis); then, in order to account for the portion of crushed concrete, the depth of the cross-section could be decreased until equilibrium ceases to exist.

The energy model in Section 2 can be improved by adding more terms to the Ritz series representing the deformed shape of the beam, but it would cost an increase of computational time.

Future work will also check the validity of the dynamic and energy models when the beams are subjected to other dynamic loads (like concentrated forces produced by the impact of falling objects) and when the boundary condition are different from what considered in this thesis (both ends simple supported).

Finally the tables produced at the end of Section 3 can also be calculated for different loads, boundary conditions, failure criterions and for other different significant parameters. Moreover, instead of a random variation of the variables accounted in this section, it would be interesting to consider other typical distribution functions such as the Gauss-normal or a Fuzzy representation.

SECTION 5

REFERENCES

[1]   Carta G, Stochino F. "Theoretical models to predict the flexural failure of reinforced concrete beams under blast loads". Engineering Structures, Volume 49, April 2013, Pages 306–315 (2013), dx.doi.org/10.1016/j.engstruct.2012.11.008.

[2]   Acito M. Stochino F. Tattoni S "Structural response and reliability analysis of rc beam subjected to explosive loading". International Conference: PROTECT 2011 "Protection & Strengthening of Structures under Extreme Loading" – Lugano 08/30 –09/01 2011 - Applied Mechanics and Materials Vol. 82 (2011) pp 434-439 doi:10.4028/www.scientific.net/AMM.82.434.

[3]   Tattoni S–Stochino F.(2012): "Azioni esplosive sulle strutture in c.a." 19° Congresso CTE, Bologna 11/8-10 2012-Pag. 407-417, ISBN: 978-88-903647-9-2.

[4]   Acito M. Stochino F. Tattoni S., "Analisi della sicurezza di travi in c.a. soggette ad azioni da esplosione". Giornate AICAP 2011 – Le prospettive di sviluppo delle opere in calcestruzzo strutturale nel terzo millennio, Padova 05/19-21 2011 – Pag. 3-11.

[5]   Stochino F. Tattoni S., "Incremento prestazionale per edifici in c.a. resistenti ad esplosione e relativa valutazione economica". Giornate AICAP 2011 – Le prospettive di sviluppo delle opere in calcestruzzo strutturale nel terzo millennio, Padova 05/19-21 2011 – Pag. 375-380.

[6]   G. C. Mays, P. D. Smith, (1995), "Blast Effect on Buildings"- second edition, Thomas Telford Publications, London ISBN: 978-0-7277-3521-8.

[7]   B. Genova, M. Genova, M.Silvestrini, (2010), "Sicurezza degli edifici nei riguardi dei fenomeni esplosivi",UTET Scienze Tecniche, ISBN: 978-88-598-0415-4.

[8]   G. De Matteis, E. Cadoni, D.Asprone, (2010), "Analysis of Behaviour of Construction Under Impact and Explosions: Approaches for Structural Analysis, from Material Modeling to Structural Response", Final Report of Urban Habitat Constructions under Catastrophic Events , edited by Mazzolani, Taylor & Francis Group, London ISBN: 978-0-415-60686-8, p. 161-178.

[9]   A. M. Remennikov, "A Review of Methods for Predicting Bomb Blast Effects on Buildings", Journal of Battlefield Technology, 2003, 6(3), 5-10.

[10]   TM 5-1300 (1990), Structures to Resist the Effects of Accidental Explosion, Departments of the Army, the Navy and the Air Force, TM 5-1300, NAVFAC P-379, AFR 88-22.

[11]   C.N. Kingery and G.Bulmash, "Airblast Parameters from TNT Spherical Air Burst and Hemispherical Surface Burst", (1984), Report ARBL-TR-02555, U.S. Army BRL, Aberdeen Proving Ground, MD.

[12]   US DEPARTMENT OF DEFENSE (DOD), "Unified Facilities Criteria UFCDOD: Structures to Resist the Effect of Accidental Explosions", (2008), UFC 3-340-02, Washington, D.C.

[13]   C.C. Hudson,"Sound Pulse Approximations to Blast Loading (with comment on Transient Drag", Sandia Corporation Technical Memorandum (1955), SC-TM-191-55-51.

[14]   A. Tyas, J.A. Warren, T. Bennet, S.D. Fay, "Prediction of Clearing Effects in Far-Field Blast Loading of Finite Targets", Shock Waves (2011), 21, pp 111-119 doi: 10.1007/s00193-011-0308-0.

[15]   A. Tyas, T. Bennet, J.A. Warren, S.D. Fay, S. E. Rigby, "Clearing of Blast Waves on Finite Sized Targets- an Overlook Approach", Proceedings of Performance, Protection and Strengthening of Structures under extreme Loading, in Applied Mechanics and Materials Vol. 82 (2011), pp 669-674, doi:10.4028/www.scientific.net/AMM.82.669.

[16]   Magnusson J, Hallgren M. High performance concrete beams subjected to shock waves from air blast. Report n. FOA-R--00-01586-311--SE, Defence Research Establishment (FOA), Tumba, Sweden; 2000.

[17]   Magnusson J, Hallgren M. High performance concrete beams subjected to shock waves from air blast, Part 2. Report n. FOI-R--1116--SE, Swedish Defence Research Agency (FOI), Tumba, Sweden; 2003.

[18]   Magnusson J, Hallgren M. Reinforced high strength concrete beams subjected to air blast loading. In: Jones N, Brebbia CA, editors. Structures under shock and impact VIII. Southampton : WIT Press; 2004, p. 53-62.

[19]   Magnusson J, Hallgren M, Ansell A. Air-blast-loaded, high-strength concrete beams. Part I: Experimental investigation. Mag Concr Res 2010; 62: 127-136.

[20]   Magnusson J, Hallgren M, Ansell A. Air-blast-loaded, high-strength concrete beams. Part II: Numerical non-linear analysis. Mag Concr Res 2010; 62: 235-242.

[21]   Zhu F. & Lu G. A Review of Blast and Impact of Metallic and Sandwich Structures, Electronic J Struct Eng, 7 Special Issue: Loading on Structures (2007) , 92-101.

[22]   Lee E.H. and Symonds P.S. Large Plastic Deformation of Beam Under Transverse Impact. J. Appl. Mech. Vol.19, No.3, 1952. 308-314.

[23]   Conroy M.F. and Providence R.I. Plastic – Rigid Analysis of Long Beams under Transverse Impact. Journal of Applied Mechanics- ASME – vol. 19 – 1952. 465-470.

[24]   Symonds P.S. and Providence R.I. Dynamic Load Characteristic in Plastic Bendings of Beams. Journal of Applied Mechanics- ASME – vol.20 1953. 475-481.

[25]   Martin J.B. and Symonds P.S. Mode Approximations for impulsively-loaded rigid plastic-structures" – Journal of Engineering Mechanics – ASCE 1966 EM.43-46.

[26]   Prager W. An introduction to plasticity. Addison Wesley Press, Reading, Mass. 1959.

[27]   Vashi, K.M., 1966. Effect of shear deformation in a beam impulsively loaded on a central portion, Master's thesis, Division of Engineering, Brown University, USA.

[28]   Symonds P.S. Plastic shear deformations in dynamic load problems. In: Heyman J, Leckie FA, editors. Engineering Plasticity. Cambridge: Cambridge University Press; 1968 p.674-64.

[29]   Symonds, P.S.; Jones, N. Impulsive loading of fully clamped beams with finite plastic deflections and strain-rate sensitivity. International Journal of Mechanical Sciences vol. 14 issue 1 January, 1972. p. 49-69.

[30]   Nonaka T. Some interaction effects in a problem of plastic beam dynamics. Parts 1–3. ASME J Appl Mech 1967;34:623–43.

[31]   Nonaka T. Shear and bending response of a rigid-plastic beam to blast-type loading. Ing-Arch 1977;46:35–52.

[32]   Menkes S.B., Opat H.J. Broken beams Experimental Mechanics, 13 (1973), pp. 480–486.

[33]   Jones N. A theoretical study of the Dynamic Plastic Behaviour of Beams and Plates with finite deflections. International Journal of Solids and Structures.- vol. 7, 1971, 1007-1029.

[34]   Jones N. Plastic Failure of Ductile Beams loaded dynamically. Journal of Eng. Ind. Trans.- ASME 1976 98(B) 131-136.

[35]   Jones N. On The Dynamic Inelastic Failure Of Beams" in Structural Failure by Wierzbicki and Jones – Wiley N.Y. 1989 pp 133-159.

[36]   Jones N, Song B. Shear and bending response of a rigid-plastic beam to partly distributed blast-type loading. J Struct Mech 1986;14(3):275–320.

[37]   Jones N, de Oliveira J.G. The influence of rotatory inertia and transverse shear on the dynamic plastic behaviour of beams. J Appl Mech 1979;46:303–10.

[38]   de Oliveira J.G., Jones N. A numerical procedure for the dynamic plastic response of beams with rotatory inertia and transverse shear effects. J Struct Mech 1979;7:193–230.

[39]   Li Q.M. Jones N. Blast loading of fully clamped beams with transverse shear effects. Mech. Struct. & Mach.,23(1), 59-86 (1995).

[40]   Jones N. Bounds on the dynamic plastic behaviour of structures including transverse shear effects. Int J ImpactEng 1985;3(4):273–91.

[41]   Lellep J., Torn K. Shear and bending response of a rigid-plastic beam subjected to impulsive loading International Journal of Impact Engineering, Volume 31, Issue 9, October 2005, 1081-1105.

[42]   Qiu X., Deshpande V.S. , Fleck N.A. Impulsive loading of clamped monolithic and sandwich beams over a central patch. Journal of the Mechanics and Physics of solids 53 (2005) 1015–1046.

[43]   Qin Qing Hua, Wang T.J. A theoretical analysis of the dynamic response of metallic sandwich beam under impulsive loading. European Journal of Mechanics A/Solids 28 (2009) 1014–1025.

[44]   Frankland J. M., Effects on Impact of Simple Elastic Structures, Taylor Model Basin Report No. 481, April, 1942.

[45]   Morison C. M. Dynamic response of walls and slabs by single-degree-of-freedom analysis—a critical review and revision. International Journal of Impact Engineering, Volume 32, Issue 8, August 2006, Pages 1214–1247.

[46]   Fundamentals of protective design (Non-nuclear) TM 5-855-1. Washington, DC: Department of the Army; March 1965. (Reprint of former document 1110-345-405, 1946).

[47]   Seiler J.A., Cotter B.A., Symonds P.S., Providence R.I., Impulsive Loading of Elastic-Plastic Beams. J. Appl. Mech. (1956) 23, 515-521.

[48]   Brooks N.B., Newmark N.M., The response of simple structures to dynamic loads, Technical report to ONR contract N6ori-071(06), Task Order VI Project NR-064-183 University of Illinois Urbana, Illinois, 1953.

[49]   Newmark NM. An engineering approach to blast resistant design, American Society of Civil Engineers Transactions, Paper No. 2786, vol. 121, 1956. p. 45.

[50]   Design of protective structures to resist the effects of nuclear weapons, AFSWC TR-59-70, December 1959. 2nd ed. TDR-62-138. Washington, DC: US Air Force; 1962.

[51]   Design of structures to resist Nuclear weapon effects. ASCE manuals & reports on engineering practice—No. 42. New York: American Society of Civil Engineers; 1961.

[52]   Design of structures to resist the effects of atomic weapons—principles of dynamic analysis and design, EM 1110- 345-415. Washington, DC: US Army Corps of Engineers; March 1957.

[53]   Design of structures to resist the effects of atomic weapons—principles of structural elements subjected to dynamic loads, EM 1110-345-416, Washington, DC: US Army Corps of Engineers; March 1957.

[54]   Biggs JM. Introduction to structural dynamics. New York: McGraw-Hill Book Company; 1964.

[55]   Fischer K., Häring I. SDOF response model parameters from dynamic blast loading experiments Engineering Structures, Volume 31, Issue 8, August 2009, Pages 1677–1686.

[56]   Nassr AA, Razaqpur AG, Tait MJ, Campidelli M, Foo S. Single and multi degree of freedom analysis of steel beams under blast loading. Nucl Eng Des 2012; 242: 63-77.

[57]   Yang G, Lok T-S. Analysis of RC structures subjected to air-blast loading accounting for strain rate effect of steel reinforcement. Int J Impact Eng 2007; 34: 1924-1935.

[58]   Magnusson J. Structural concrete elements subjected to air blast loading [Licentiate thesis]. TRITA-BKN Bulletin 92. Stockholm (Sweden): Royal Institute of Technology; 2007.

[59]   Baker W.E., Cox P.A., Westine P.S., Kulesz J.J., Strehflow R.A. (1983) Explosion Hazards and Evaluation. Elsevier. New York.

[60]   Clough, R. W. Penzien, J. (1995). Dynamics of Structures, Computers & Structures Inc. Berkley CA USA, 730 pp.

[61]   Stronge, W.J., and Yu, T.X. (1993) Dynamic models for structural plasticity, Springer-Verlag, London ISBN: 0-387-19815-6.

[62]   Goldsmith W. Impact: The Theory and Physical Behaviour of Colliding Solids. Edward Arnold Publishers, London (1960).

[63]   Symonds, P.S. (1980) Elastic, finite deflection and strain rate effects in a mode approximation technique for plastic deformation of pulse loaded structures, Journal of Mechanical Engineering Science; 22(4): 189-197.

[64]   Symonds, P.S. (1980) Finite elastic and plastic deformations of pulse loaded structures by an extended mode technique, International Journal of Mechanical Sciences; 22(10): 597-605.

[65]   Yankelevsky, D.Z. (1985) Elastic-plastic blast response of rectangular plates, International Journal of Impact Engineering; 3(2): 107-119.

[66]   Schleyer, G.K, and Hsu, S.S. (2000) A modelling scheme for predicting the response of elastic-plastic structures to pulse pressure loading, International Journal of Impact Engineering; 24: 759-777.

[67]   Symonds, P. S., and Jones, N. (1972). Impulsive loading of fully clamped beams with finite plastic deflections and strain rate sensitivity. Int. J. Mech. Sci., 14, 49–69.

[68]   Carney J. F., and Yeh, C. W. (1991). ''Viscoplastic response of clamped beams under impact loading.'' J. Struct. Engrg., ASCE, 117(12), 3680–3697.

[69]   Boutros M. (2000). Elastic-Plastic Model of Pinned Beams Subjected to Impulsive Loading. J. Eng. Mech., 126(9), 920–927.

[70]   Fujikake K, Li B, Soeun S. Impact response of reinforced concrete beams and its analytical evaluation. J Struct Eng ASCE 2009; 135: 938-950.

[71]   Gere, J. M. and Timoshenko, S. P., 1997, Mechanics of Materials, PWS Publishing Company.

[72]   Frýba L. 1996 Dynamics of Railway Bridges. Thomas Telford Ltd. London ISBN: 0-7277-2044-9.

[73]   Frýba L. 1972 Vibration of Solids and Structures under Moving Load. Czechoslovak Academy of Science.

[74]   Hudson JL, Darwin D. Evaluation and repair of blast damaged reinforced concrete buildings. SL Report 05-1, University of Kansas Center for Research, Inc., Lawrence, Kansas, USA; 2005.

[75]   Remennikov AM, Kaewunruen S. Impact resistance of reinforced concrete columns: experimental studies and design considerations. Proceedings of the 19th Australasian Conference on the Mechanics of Structures and Materials; 2006 Nov 29 - Dec 1;

Christchurch, New Zealand. Tailor & Francis; 2007, p. 817-824.

[76]   Tachibana S, Masuya H, Nakamura S. Performance based design of reinforced concrete beams under impact. Nat Hazards Earth Syst Sci 2010; 10: 1069-1078.

[77]   Alves M, Jones N. Impact failure of beams using damage mechanics: Part II – Application. Int J Impact Eng 2002; 27: 863-890.

[78]   Lawver D, Daddazio R, Vaughan D, Stanley M, Levine H. Response of AISC steel column sections to blast loading. Proceedings of the ASME 2003 Pressure Vessels and Piping Conference; 2003 Jul 20-24; Cleveland, Ohio, USA. New York: ASME; 2003, p. 139-148.

[79]   Federal Institute of Technology. Model Code 2010, First Complete Draft, Volume 1. Lausanne (Switzerland): fib Bulletin 55; 2010.

[80]   Riedel W, Fischer K, Kranzer C, Erskine J, Cleave R, Hadden D et al. Modeling and validation of wall-window retrofit system under blast loading. Eng Struct 2012; 37: 235-245.

[81]   Mattock, A. H.,1967. "Discussion of 'rotational capacity of reinforced concrete beams." J. Struct. Div., 93ST2, 519–522.

[82]   Comité Euro-International du Béton. Concrete structures under impact and impulsive loading. Lausanne (Switzerland): CEB Bulletin 187; 1988.

[83]   Asprone D, Frascadore R, Di Ludovico M, Prota A, Manfredi G. Influence of strain rate on the seismic response of RC structures. Eng Struct 2012; 35: 29-36.

[84]   Graff KF. Wave motion in elastic solids. New York: Dover Publications, Inc.; 1991.

[85]   Greenspon J.E. Plastic Behaviour of Control Surfaces and Plates Subjected to Air blast Loading Part 1. Simplified Theoretical Relations. Contract No. DA36-034-ORD-3081RD with BRL, Nov. 1960.

[86]   Greenspon J.E. Plastic Behaviour of Control Surfaces and Plates Subjected to Air blast Loading Part 2. Detailed Analysis and Numerical Results for Beam Type Structures. Contract No. DA36-034-ORD-3081RD with BRL, Nov. 1962.

[87]   Greenspon J.E. Prediction of Iso-Damage Curves. Contract No. DAAD05-67-C-0331-with BRL, Nov. 1967.

[88]   Greenspon J.E. Elastic-Plastic Response of Structures to Blast and Impulse Loads. . Contract No. DA- 18-001 -AMC-101 9(X) with BRL. March 1967.

[89]   Greenspon J.E. Theoretical Calculations of Iso-Damage Characterizations. Contract No. DAADO5-69-C-01 16 with BRL. Feb. 1960.

[90]   Westine P.S., Baker W.E. Energy solutions for predicting deformation in blast-loaded structures. Report EM-CR—76027-N.6, Contract No. DAAA15-75-0083 DAAD05-74-C-0751 Edgewood Arsenal Contractor Report ,Department of the Army, Aberdeen Proving Ground, Maryland 21010, USA; 1975.

[91]   Westine P.S., Cox P.A. Additional energy solutions for predicting deformation in blast-loaded structures. Report EM-CR—76031-N.4, Contract No. DAAA15-75-C-0083 Edgewood Arsenal Contractor Report ,Department of the Army, Aberdeen Proving Ground, Maryland 21010, USA; 1975.

[92]   Cox P.A., Westine P.S., Kulesz J.J., Esparza E.D. Analysis and evaluation of suppressive shields. Report n. ARCSL-CR—77028-N.10, Edgewood Arsenal Contractor Report ,Department of the Army, Aberdeen Proving Ground, Maryland 21010, USA; 1978.

[93]   Florence A.L. and Firth R.D. Rigid Plastic Beams Under Uniformly Distributed Impulses. Journal of Applied Mechanics 32 Series E, 1 March 1965 pp. 7-10.

[94]   Bouthier O.M., Bernhard R.J. Simple models of the energetic of transversely vibrating plates Journal of Sound and Vibration, 182 (1995), pp. 149–164.

[95]   Lyon R. H. 1975 Statistical Energy Analysis, Cambridge, Massachusetts: MIT Press.

[96]   Lyon R.H., Dejong R.G., Theory and Application of Statistical Energy Analysis, Seconded. Butterworth-Heinemann,London,1995.

[97]   Ju-Bum Han, Suk-Yoon Hong, Jee-Hun Song Energy flow model for thin plate considering fluid loading with mean flow, Journal of Sound and Vibration, Volume 331, Issue 24, 19 November 2012, Pages 5326-5346.

[98]   Belov V.D., Rybak S.A., Tartakovskii B.D. Propagation of vibrational energy in absorbing structures, Journal of Soviet Physics Acoustics, 23 (2) (1977), pp. 115–119.

[99]   Wohlever J.C., Bernhard R.J.. Mechanical energy flow models of rods and beams. Journal of Sound and Vibration, 153 (1973), pp. 1–19.

[100] Bouthier O.M., Bernhard R.J. Simple models of the energetics of transversely vibrating plates. Journal of Sound and Vibration, 182 (1995), pp. 149–166.

[101] Bouthier O.M., Bernhard R.J. Simple models of the energy flow in vibrating membranes. Journal of Sound and Vibration, 182(1) (1995), pp. 129–147.

[102] Ju-Bum Han, Suk-Yoon Hong, Jee-Hun Song. Energy flow model for thin plate considering fluid loading with mean flow. Journal of Sound and Vibration, 331 (2012) 5326–5346.

[103] Luzzato E. Approximations and solutions of the vibration energy density in equation beams. 1991 Proceedings of Inter Noise 91. 675-678.

[104] Lase Y and Jezequele L. Analysis of a dynamic system based on a new energetic formulation. 1990 International Congress on Intensity Techniques, Senlis, 277-279.

[105]   Le Bot A. and Jezequele L. Energy formulation for one-dimensional problems. 1993 Proceedings of the Institute of Acustic 15(3). 561-568.

[106]   U. Starossek: "Progressive Collapse of Multi-Span Bridges:A Case Study", Report, LABSE Symposium "Structures for the Future – the Search of Quality", Rio de Janeiro, Brazil, 25-27 August 1999.

[107]   Low H.Y., Hao H., Reliability analysis of reinforced concrete slabs under explosive loading. Structural Safety 23 (2001) 157–178.

[108]   H.-C. Rong and B. Li, Probabilistic response evaluation for RC flexural members subjected to blast loadings. Structural Safety 29 (2007) 146–163.

[109]   Borenstein E., Benaroya H., Sensitivity analysis of blast loading parameters and their trends as uncertainty increases. Journal of Sound and Vibration, Volume 321, Issues 3–5, 10 April 2009, Pages 762–785 http://dx.doi.org/10.1016/j.jsv.2008.10.017.